

The Pennsylvania State University

The Graduate School

College of Earth and Mineral Sciences

**FABRICATION AND ANALYSIS OF 2D TMD BASED DEVICES FOR INTEGRATION
INTO MORE-THAN-MOORE ELECTRONIC SYSTEMS**

A Dissertation in

Materials Science and Engineering

by

Donna D. Deng

© 2019 Donna D. Deng

Submitted in Partial Fulfillment
of the Requirements
for the Degree of

Doctor of Philosophy

May 2019

The dissertation of Donna D. Deng was reviewed and approved* by the following:

Joshua A. Robinson
Associate Professor of Materials Science and Engineering
Dissertation Advisor
Chair of Committee

Mauricio Terrones
Distinguished Professor of Physics, Chemistry, and Materials Science and
Engineering

Christine Keating
Professor of Chemistry

Aida Ebrahimi
Assistant Professor of Electrical Engineering

Suzanne Mohney
Professor of Materials Science and Engineering and Electrical Engineering
Chair, Intercollegiate Graduate Degree Program in Materials Science and
Engineering

*Signatures are on file in the Graduate School

ABSTRACT

As the silicon MOSFET approaches scalability limits, diversification of components in microprocessors becomes necessary to increase the value of digital circuitry and to facilitate networks of functional components known as the Internet of Things. Targeted functionalities focus on the direct interaction of digital components with its environment for applications in medicine, energy, and more. This is an attractive front for many novel materials with unique properties that are superior to silicon in specific applications. Among them are layered 2-dimensional materials, with unique optoelectronic and physical properties that make them attractive for various applications from sensors to flexible electronics.

Due to the large surface-to-volume ratio of 2D transition metal dichalcogenides (TMDs), the integration, device fabrication, and post-processing techniques can affect the material properties and thus characteristics of the subsequent devices. In order to produce 2D TMD-based devices at industrial levels, these effects must be well understood. This dissertation aims to provide insight into the relationships between material properties, processing techniques, and characteristics of transistor and sensing devices through material integration, device fabrication, and electrical characterization of 2D TMD-based devices. Specifically, this dissertation work furthers the understanding of how choices in growth or integration and post-processing techniques can affect characteristics of 2D TMD-based devices, focusing on MoS₂ based devices; understanding how device characteristics are intertwined with material properties and device fabrication allows for direct tuning of these factors in optimizing 2D TMD-based device design and fabrication for transistor and sensing devices.

Chapter 1 provides context and motivation for the thesis, and Chapters 2 and 3 provide information necessary for discussions in the remainder of the dissertation. Chapter 2 focuses on background information regarding materials, devices, and processes used in the dissertation studies,

including discussion on current challenges for 2D materials. Chapter 3 details the exact materials and methods steps used.

Chapters 4 through 6 describe thesis research topics. Chapter 4 focuses on the dielectrophoretic self-assembly of 2D monolayer WS₂ and MoS₂ monolayers and the effect of the integration process on the material. In both cases, the monolayers lay flat and densely along the edge of a parallel electrode system with negligible physical damage. Based on semi-analytical calculations, the most commonly observed orientation of assembly, a 0° orientation defined as where a triangle side spans the electrode gap, is suggested to be driven by the minimization of the potential energy of an assembling particle. Raman and photoluminescence spectroscopy reveal that no observable damage is incurred on the particle after assembly. Adjustments on the assembly electrode to include lateral positioning guides and photoresist wells provided more precise control of rectangularly patterned TMD films, but with a diminished assembly rate, possibly due to the large spatial periodicity of the target assembly locations.

Chapter 5 moves away from transfer processes to a direct synthesis of epitaxial graphene – MoS₂ heterostructures for electrical contact in order to combat the high contact resistance of conventional metal contacts due to Fermi level pinning. The heterostructure exhibits an order of magnitude improvement in the contact resistance from 235.4 kΩ/μm for a metal contacted device to 11.6 kΩ/μm for a heterostructure contact device at no applied gate bias. FETs fabricated using these contacts performed drastically better than conventional metal contacted devices, with a more than three-fold improvement in the subthreshold swing from 312 mV/dec to 89.2 mV/dec and two orders of magnitude increase in the device on/off ratio. Band alignment calculations based on low energy electron reflectivity reveal that the barrier to electron transport across a metal-MoS₂ contact and a graphene-MoS₂ contact is 1.01 and 0.51eV respectively, suggesting that the improvement in electrical transport stems from the lower barrier to electron transport for a graphene-MoS₂ junction. A first order comparison of FETs utilizing the directly synthesized graphene-MoS₂ heterojunctions

to exfoliated heterojunctions show that the latter subthreshold swing is lower at 213 mV/dec, suggesting the pristine quality of the direct growth method is advantageous for electrical transport.

Finally, Chapter 6 focuses on the effects of material, processing, and experimental design on the sensing characteristics of MoS₂ chemiresistors using triethylamine analyte. It is observed that defects may play a large role in increasing the sensing amplitude or sensitivity of the MoS₂ chemiresistors. Exposing a MoS₂ sensor to ultra-violet ozone (UV O₃) and inducing Mo-O bonds increased the saturation signal amplitude by up to 30x, with an observed maximum of 920% at 15 minutes of exposure to 1 ppm UV O₃. Doping the MoS₂ channel with 5.6 at% Nb changed the major carrier type in the material to holes instead of electrons in pristine films, with a decrease in the signal amplitude from ~45% to ~15%, but with an ultimately 50 times increase in the signal to noise ratio. For experimental design, the Ti/Au contacted devices performed better than the EG devices with 4 orders of magnitude increase in the saturation signal amplitude and 1 order of magnitude increase in the signal to noise ratio. Finally, it is observed that low-energy white light illumination is sufficient in inducing a signal increase in the MoS₂ channel, suggesting an improvement in the mobility of the carriers with induced light.

TABLE OF CONTENTS

LIST OF FIGURES	ix
LIST OF TABLES.....	xvi
ACKNOWLEDGEMENTS	xvii
Chapter 1 Introduction.....	1
1-1. Moore's law	1
1-2. Two-dimensional materials	3
Chapter 2 2-Dimensional Materials: Introduction to Materials and Devices.....	6
2-1. 2-dimensional transition metal dichalcogenides	6
2-1-1. Introduction to semiconductors	6
2-1-2. Introduction to 2-dimensional materials.....	7
2-2. Synthesis and integration of 2-dimensional transition metal dichalcogenides	10
2-2-1. 2-dimensional material transfer methods	11
2-2-2. Bottom-up growth of transition metal dichalcogenides	15
2-2-3. Bottom-up growth of graphene.....	19
2-3. Introduction to electronic devices.....	20
2-3-1. Resistors	20
2-3-2. Metal-semiconductor junctions.....	21
2-3-3. Transistors	26
2-3-2. Chemical vapor sensors.....	29
2-4. Basics of device fabrication.....	35
2-4-1. Lithography	36
2-4-2. Plasma etching	38
2-4-3. Physical vapor deposition	39
2-4-4. Gate dielectric	41
2-5. Summary	44
Chapter 3 Experimental Procedures	45
3-1. Lithography on 2-dimensional materials	45
3-1-1. Optical lithography	46
3-1-2. Electron beam lithography	46
3-1-3. Photoresist removal.....	47
3-2. Substrate preparation.....	48
3-2-1. Alignment marks.....	48

3-3. Material growth.....	49
3-3-1. Pre-growth cleaning	49
3-3-2. Powder vaporization growth.....	50
3-3-3. Epitaxial graphene-powder vaporization MoS ₂ Growth	50
3-3-4. Metal-organic chemical vapor deposition MoS ₂ growth.....	51
3-4. Device fabrication	52
3-4-1. Transition metal dichalcogenide dispersion	52
3-4-2. Device isolation	53
3-4-3. Device contact	53
3-4-4. Solid electrolyte gate.....	54
3-5. Device analysis setup	55
3-5-1. Field effect transistor measurements.....	55
3-5-2. Sensing measurements	55
3-6. Characterization techniques.....	57
3-6-1. Microscopy techniques.....	57
3-6-2. Spectroscopy techniques	58
3-7. Summary	59
Chapter 4 Dielectrophoretic Assembly as a Scalable Alternative to Exfoliation for 2-Dimensional Transition Metal Dichalcogenide Integration	60
4-1. Introduction	60
4-2. Theoretical discussions on the assembly of 2-dimensional materials	61
4-2-1. Dielectrophoretic forces on assembling WS ₂	61
4-2-2. Additional forces during assembly	63
4-3. Materials and experimental methods.....	65
4-3-1. Transition metal dichalcogenide dispersion	65
4-3-2. Assembly electrode	66
4-3-3. Characterization	67
4-4. Results and Discussion.....	68
4-4-1. Assembly of WS ₂ – physical characterization	68
4-4-2. Assembly of WS ₂ : optical characterization	72
4-4-3. Assembly of MoS ₂	73
4-4-4. Lateral positioning control of transition metal dichalcogenide flakes	74
4-5. Summary & Future work	76
Chapter 5 MoS₂- Epitaxial Graphene Heterostructures as Electronic Contacts.....	78
5-1. Introduction	78

5-1-1. Graphene contact to MoS ₂	78
5-2. Materials and experimental methods.....	80
5-2-1. Growth and fabrication of devices with synthetic contacts	80
5-2-2. Device fabrication of exfoliated epitaxial graphene-MoS ₂ devices	82
5-2-3. Characterization tools.....	83
5-3. Results and discussion.....	83
5-3-1. Epitaxial graphene – MoS ₂ heterostructures.....	83
5-3-2. Device characteristics of epitaxial graphene-contacted MoS ₂ field effect transistors.	86
5-3-3. Band alignment comparison of epitaxial graphene-MoS ₂ and Ti/Au-MoS ₂	89
5-3-4. Comparison of synthesized and exfoliated epitaxial graphene-MoS ₂ heterostructures	90
5-4. Summary & future work.....	91
Chapter 6 Exploration of the Roles of Material and Device design on Sensing Characteristics of MoS ₂ -Based Chemiresistors	93
6-1. Introduction	93
6-2. Materials and experimental methods.....	96
6-2-1. Material growth and device fabrication.....	96
6-2-2. Ozone exposure	97
6-2-3. Sensing methods	97
6-3. Results and discussions	98
6-3-1. Basic device sensing characteristics of MoS ₂ chemiresistors	98
6-3-2. Effect of growth process on sensing characteristics.....	100
6-3-3. Effect of controlled defects on sensing characteristics: ozone exposure	102
6-3-4. Effect of controlled defects on sensing characteristics: Nb-doping	104
6-3-5. Effect of contact material on sensing characteristics	107
6-3-6. Effect of low-energy illumination on sensing characteristics	110
6-4. Summary & future work.....	111
Chapter 7 Dissertation Summary	115
References	118

LIST OF FIGURES

Figure 1-1. A plot showcasing the number of transistors on a single microprocessor from 1970 to 2016. The transistor count is plotted in log scale, showcasing the exponential increase in the transistor count over the years (adapted from reference ¹⁰).....	2
Figure 1-2. An illustration of the combined push for higher value systems through “More-Moore” (further scaling of microprocessor components) and “More-than-Moore” (diversification of the functionalities of microprocessor components) (adapted from reference ⁴).....	3
Figure 1-3. A schematic of various 2D materials and a table of 2D TMDs listed with their characteristics, including crystal structure and other various properties: ferromagnetism (F), anti-ferromagnetism (AF), superconductivity (S), and charge density wave (CDW) (adapted from reference ²⁹).	5
Figure 2-1. a) An illustration of the spreading of energy states for an atom as a function of interatomic spacing. b) Three types of band structures for conductors, insulators, and semiconductors. (Both a) and b) adapted from reference ⁴¹).....	7
Figure 2-2. a) An illustration of the honeycomb crystal structure showcasing flexibility of a graphene sheet. b) A map of the electronic band structure of graphene, showing the Dirac cones where the conduction and valence bands come to a point (adapted from reference ⁵¹).	8
Figure 2-3. a) An illustration of the 2H and 1T structures, illustrating the alignment of the chalcogen (blue) atoms relative to the metal (gray) atoms (adapted from reference ⁵⁶). b) A survey of bandgaps of various 2D materials. The wide range of alignment allows for the fabrication of various types of heterostructures (adapted from reference ⁵⁷).	9
Figure 2-4. An illustration of the scotch tape method for exfoliating mono- to few-layer graphene (adapted from reference ⁶⁸).	11
Figure 2-5. a) schematic of a parallel electrode assembly system with VO ₂ nanorods suspended in a solution. b) an optical image of VO ₂ nanorods assembled on the electrode gap in a perpendicular configuration (D. Deng, unpublished).	13
Figure 2-6. a) Schematics of a particle in uniform and non-uniform electric field. In a uniform field, the particle may see a rotational torque, but there is no net force on the particle. In a non-uniform field, forces on the particle do not cancel out and thus there is a finite force on the particle. b) A plot of the real part of the CM factor as a function of AC bias frequency for assembly of MoS ₂ . The plot also illustrates the effect of the material conductivity on the CM factor (D. Deng, unpublished).	14
Figure 2-7. a) A schematic of a hot-wall CVD reactor. b) A simplified schematic of the chemical vapor deposition process, showing the transport of a precursor into and through the	

boundary layer, adsorption on to the substrate surface, and the transport across the substrate surface until it reacts into the targeted product.	16
Figure 2-8. A comparison of an example set of PV and MOCVD processes, illustrating the growth set up (a & b), SEM images of the growth (c & d), and XPS spectra for Mo 3d and S 2p, with corresponding Mo:S ratio (e & f) ¹⁰² . In general, MOCVD growths are more uniform and stoichiometric, while PV growths are much faster. (c), d), and f): D. Deng unpublished)	18
Figure 2-9. a) a schematic of the Nb-doped MOCVD MoS ₂ growth set up, showing NbCl ₅ powder introduced upstream. b) A plot showing the location of the fermi level within the MoS ₂ band gap as a function of at% of Nb on various substrates (K. Zhang, in preparation).	19
Figure 2-10. An illustration of the growth of epitaxial graphene on SiC, and a cross-sectional TEM showing the graphene layers and the buffer layer. Exact details on the growth and TEM parameters are discussed in Section 3-3-2 and 3-6-1 respectively.	20
Figure 2-11. a) A basic schematic of a resistor. b) An illustration of a thin sheet-like resistor with a square region governed by R_s	21
Figure 2-12. a) Band diagrams before and after contact of a metal and n-type semiconductor in an ohmic contact with b) a corresponding current-voltage characteristic. c) Band diagrams before and after contact of a metal and a n-type semiconductor in a Schottky contact with d) a corresponding current voltage characteristic. (a) and c) adapted from reference ¹¹³).....	23
Figure 2-13. Schematic of the three transport mechanisms of charged carriers across a Schottky barrier based on the doping concentration and thus the Schottky barrier width (adapted from reference ⁴³).	24
Figure 2-14. a) A channel with two electrical contacts and its equivalent circuit. b) A graphical representation of the relationship between channel length and the total device resistance.	25
Figure 2-15. a) A schematic of a VO ₂ phase-transition FET. b) A secondary electron microscope image of a VO ₂ nanowire contacted on both ends, and a c) representative resistivity transition driven in the material by heating (D. Deng, unpublished).	26
Figure 2-16. a) Band alignment schematic of a MOScap with a p-type semiconductor. b) Band diagram of the MOScap under $V_G < 0$. Majority carriers (holes in this case) accumulate near the semiconductor surface. c) Band diagrams of the MOScap under a gate bias $V_G > 0$. Inversion of the carrier type at the semiconductor interface begins to occur at small magnitudes of V_G . As V_G is increased, the inversion increases and minority carriers accumulate at the semiconductor surface. d) A cross-sectional schematic of a MOSFET, illustrating the MOScap and the inversion layer induced in the semiconductor channel. e) Example I_D - V_D curves over a range of V_G in log and linear scale. (adapted from reference ³) f) Example I_D -	

V_G curves in linear and log scale. (adapted from reference ¹⁶) g) A simple schematic illustrating the subthreshold swing in I_D - V_G curves.	28
Figure 2-17. a) A scale of the relative acidity and basicity with examples of some functional groups (adapted from reference ¹²¹). b) A schematic showing the direction of charge transfer between MoS ₂ and NH ₃ or NO ₂ , which are Lewis base and acid respectively (adapted from reference ¹²²).	30
Figure 2-18. a) A simplified example plot of sensing signal over time in an ideal device (blue) and realistic device (red) for two analyte pulses at varying concentrations. The yellow highlighted regions correspond to when the sensor is exposed to analyte. b) A simple schematic of a sensor before exposure and at steady-state during exposure, showing the equilibrium of flux onto and off of the substrate at steady-state. c) The adsorption density q as a function of the concentration for Langmuir and Freundlich models, in comparison to a linear model (adapted from reference ¹²⁹).	32
Figure 2-19. A schematic of the basic fabrication steps required to fabricate a simple two-terminal device. Material is transferred or grown on a film, then lithographically patterned for isolation etching. After cleaning, the patterning is repeated for the deposition of contact metals. Depending on the complexity of the device, other processes or repetitions may be used. However, the devices in this dissertation work is limited to 2 or 3 patterning processes after growth in order to minimize resist residue.	36
Figure 2-20. a) AFM image of the surface of a MoS ₂ device after several photoresist lithography processes and a simple cleaning step. (D. Deng, unpublished) b) A comparison of the PL of WS ₂ before any cleaning, after an anneal in H ₂ /N ₂ , and after an AFM “nano-squeegee” cleaning process, where the polymer residue is physically scraped away. The disappearance of the trion peak suggests the AFM method is effective, and the PMMA residue on the surface directly affects the electrical properties of the WS ₂ (adapted from reference ¹⁴⁶).	37
Figure 2-21. a) A schematic of an inductively coupled plasma etch chamber, based on the system most frequently used in this dissertation. The sample is placed on a bias electrode towards which the charged particles in the plasma are accelerated. b) A comparison of contact resistance of Ti/Au on epitaxial graphene for various duration of plasma treatment. 90s O ₂ plasma before the metal deposition reduces the contact resistance by three orders of magnitude (adapted from reference ¹⁵²). ..	39
Figure 2-22. a) A schematic of a physical vapor evaporation system. In this thesis, an electron beam is utilized to vaporize the material (adapted from reference ¹⁵⁸). b) A cross-sectional illustration of a single layer and double layer photoresist stack for metal patterning. Using a single stack can lead to sidewall deposition that can collapse after resist removal or lead to lift-off failure. c) Device transfer characteristics measured for devices using various metals as contacts to MoS ₂ . There is a correlative trend between the proximity of the metal work function to the MoS ₂ conduction band and the device performance (adapted from reference ⁶²). d) A map	

of the metal work function and the energy level at which various metals are pinned to for both bulk and monolayer devices is plotted. The metal work function appears to have minimal effect on the location at which the metal pins to the semiconductor (adapted from reference ¹⁶¹).....	41
Figure 2-23. An illustration of the self-limiting cycles of ALD growth for Al ₂ O ₃ , showing the self-limiting cycles of TMA and H ₂ O reactions on the sample surface (adapted from reference ¹⁶⁹).....	42
Figure 2-24. a) Atomic force microscope (AFM) images of MOCVD WSe ₂ with 2 nm of seed layer and 20nm of ALD. Using Al ₂ O ₃ seeds lead to lower roughness of the subsequent ALD film. b) Drain current and gate leakage current as a function of gate bias for a 33μm wide MoS ₂ channel with 2nm Al ₂ O ₃ seed and 20nm ALD Al ₂ O ₃ . The inset shows the data on a log scale (D. Deng, unpublished).....	43
Figure 3-1. A schematic of the basic fabrication steps required to place contacts on a heterostructure material after growth. First, the material is grown on a substrate using one of the methods discussed in Section 3-3. After growth, a photoresist patterning is performed for isolation etching, discussed in Section 3-4-2. The photoresist is removed using the standard cleaning procedure listed in Section 3-1-3. After cleaning, another photoresist patterning is performed, this time for the deposition of contact metals, discussed in Section 3-3-3. Depending on the complexity of the device, other processes or repetitions of earlier fabrication steps may be necessary.	45
Figure 3-2. a) Illustration of the sensing system setup. b) an equivalent circuit system of the sensor during measurement by the LIA (F.K. Perkins).....	57
Figure 4-1. a) A cross-sectional schematic of an assembly device with parallel electrodes and a corresponding field gradient map of taken from above. b) A cross-sectional map of the DEP force on a 3 μm wide WS ₂ particle as a function of position. Both sets of maps are calculated using COMSOL Multiphysics.	63
Figure 4-2. A schematic of the series of steps used to transfer PV-grown TMD sheets on SiO ₂ /Si into an acetone dispersion that can be dropped on an assembly electrode. 3 μL of the dispersion is used for each assembly system.	66
Figure 4-3. a) A simplified illustration of the interdigitated assembly electrodes used for the assembly of WS ₂ . In the actual device, there are 12 pairs of interdigitated fingers, 150 μm wide and separated by 3μm. b) A schematic of the DEP assembly setup for WS ₂ over an electrode gap.....	67
Figure 4-4. a) A low magnification SEM image of the electrodes displaying the preferential positioning of the TMD sheets in the electrode gap regions. b) A closer look at the electrode region. c) Zoomed in images of representative assembled particles. Negligible wrinkling or physical damage is observed. d) An illustration showing the defined particle orientations. e) A survey of 100+ assembled particles and their	

assembled orientation. There is a clear preference for particles to assemble in the 0° orientation.....	69
Figure 4-5. a) An equivalent circuit schematic of a particle in suspension above the electrode. The inset shows an SEM image of an assembled particle, illustrating the region of the particle that overlaps with the electrode. c) A semi-analytical plot of the in-plane torque as a function of particle orientation for triangles 1.9 ~ 2.1 times the size of the electrode gap.	71
Figure 4-6. a) A schematic of an assembled particle with example positions of the “on electrode” and “over gap” positions. b) A comparison of the PL spectra of WS ₂ taken before and after assembly with fitted curves for the Trion X ⁻ and Exciton X ⁰ peaks. c) a comparison of the Raman spectra of WS ₂ taken before and after assembly.....	73
Figure 4-7. a) an SEM image of a monolayer crystal of MoS ₂ is assembled across a 3μm wide electrode gap. The wrinkle in the center of the monolayer is believed to stem from strained growth on the SiO ₂ /Si substrate. b) Raman spectra obtained from MoS ₂ before and after assembly. No significant change is observed post-assembly.	74
Figure 4-8. a) An overview of the assembly structure with extended fingers and a patterned resist well. b) Top view map of the electric field gradient on a similar electrode structure. the field gradient appears highest around the finger tips. c) A cross-sectional schematic and resulting MoS ₂ film assembly on the extended finger electrode, showing the positioning and orientation control of this assembly design.	75
Figure 4-9. A cross sectional map of the field gradient in logarithmic color scale. While the geometry of the field gradient differs before and after assembly, the relative high-gradient positioning and magnitude are similar. This suggests that the DEP force at the electrode gap still persists and assembly of subsequent 2D TMD layers may be possible for the fabrication of van der Waals heterostructures.	77
Figure 5-1. a) A cross-section illustration of a 2D FET, with graphene contacts to the MoS ₂ channel. b) A direct comparison between contact resistance between metal contacted and graphene contacted MoS ₂ FETs over a range of gate voltage (adapted from reference ²⁰¹). c) A dark-field TEM image of a directly grown MoS ₂ -CVD graphene lateral heterojunction, showing the abrupt material interface (adapted from reference ²⁰⁸).....	80
Figure 5-2. a) A schematic of the fabrication process of EG-MoS ₂ heterostructures. b) False colored SEM images of the heterostructure and metal-contacted devices. c) A schematic of a heterostructure device with an electrolytic global gate.	81
Figure 5-3. a) A schematic of the plumed growth on the substrate and corresponding false colored SEM images of the EG-MoS ₂ heterostructure. The uncoalesced regions showcase the MoS ₂ growth outwards from the edge of the EG. b) an AFM image and c) a PL map of a series of EG rectangles with MoS ₂ growing around them. ...	84

Figure 5-4. Cross-sectional TEM images of a) graphene, b) MoS ₂ c) and the heterostructure interface. These reveal the high quality of the growths and a pristine overlap region. e) A series of elemental mapping obtained using EDS that further prove that the interface is sharp with no intermixing.	86
Figure 5-5. a) The total device resistance of heterostructure and metal contacted devices before and after the deposition of the electrolytic gate. b) An example of the TLM method, where the resistance of a series of devices are recorded and fit as a linear function of channel length. c) A comparison of the contact resistance of the heterostructure devices and the metal contacted devices. d) The transfer curves of a heterostructure device and a Ti/Au contacted device.	88
Figure 5-6. a) A LEED image showing the polycrystallinity of MoS ₂ and crystallinity of EG in an overlap region. b) a set of band alignment diagrams estimated from LEER values. The electron barrier to transport for the Ti/Au contacted device is twice the height of the EG contacted devices.	90
Figure 5-7. a) A false color SEM of the exfoliated EG-MoS ₂ FET. The source-drain electrical signal is driven through the metal contacts at the bottom of the image, which extend out to large pads. b) A comparison of the transfer curves for the directly synthesized and exfoliated EG-MoS ₂ FETs. The directly synthesized heterostructures exhibit a significantly faster turn-on.	91
Figure 6-1. a) A schematic of the Internet of Battlefield Things, illustrating the goal of a communication network of soldiers, sensors, vehicles, and other military apparatus (adapted from reference ²³¹). b) The molecular structure of TEA. c) The chemical structure of several V-series nerve agents, highlighting the amine functional group in light blue that is isolated after decomposition (adapted from reference ²³²).....	94
Figure 6-2. a) Optical image of an MOCVD MoS ₂ device, showing the interdigitated structure. b) XPS of the Mo 3d and S 2p peaks originally shown in Chapter 2. The Mo:S ratio is ~1:1.98. c) The sensing characteristics of MoS ₂ devices over increasing concentrations of TEA. The response time listed corresponds to these specific curves and not a surveyed or averaged representation of a number of devices. d) A pulsed sensing characteristic of the same device in (c) at 10 ppm pulsed for 15 s and 45 s recovery. The peak-to-valley signal for each pulse is also plotted.....	99
Figure 6-3. a) Sensor signal over time through ten 30 second pulses of pure N ₂ at 5 lpm flow. b) Sensor signal over time through a single 5 minute pulse of 3 ppm o-NTol in N ₂ . In both a) and b), no detectible sensor signal is observed.	100
Figure 6-4. a) A representative comparison between a PV and MOCVD grown MoS ₂ film under 100 ppm TEA/N ₂ exposure. the PV grown film exhibits a 3.5x increase in the saturation signal. b) SEM images of PV and MOCVD grown films. The PV domains are larger and thicker, while the MOCVD growths are smaller but appear more crystalline.	101

Figure 6-5. a) XPS data for the S 2p peak of a MOCVD MoS₂ sample before and after 10 minutes in ~4 ppm UV O₃ exposure. After the exposure, peaks corresponding to S-Mo-O bonds are observed. b) A calculation of S to Mo concentration for increasing ozone exposure times. The ratio stabilizes at approximately 0.94 above 10 min of exposure. c) An illustration of MoS₂ after exposure to UV O₃ where the top sulfur layer has been removed and replaced with O and vacancies to produce a MoOS Janus structure. d) The saturation signal of MOCVD and PV MoS₂ sensors as a function of ~1 ppm UV O₃ exposure time. Both devices exhibit a similar increase in sensing, a peak in the saturation is observed for MOCVD devices at 15 minutes. The inset shows the S/N ratio of the MOCVD sensing curves, which mirror the trend seen in the saturation signal..... 103

Figure 6-6. a) SEM images of MOCVD MoS₂ sensor channels for pristine and 5.6 at% MoS₂ films contacted by Ti/Au metal electrodes. b) The XPS data near the valence band edge of MoS₂. The fermi level shifts closer to the valence band edge at higher doping concentrations (K.Zhang, in preparation). c) Current voltage characteristics for pristine and 5.6 at% Nb MoS₂ devices. The latter is approximately three orders of magnitude more conductive. d) Sensing characteristics of pristine and 5.6 at% Nb MoS₂ sensors in 100 ppm TEA/N₂. While the pristine MoS₂ exhibits an increase in signal with analyte exposure, 5.6 at% Nb doped MoS₂ exhibits a decrease in the conductance. e) Sensing characteristics of pristine and 5.6 at% Nb MoS₂ sensors in 15ppb TEA/N₂. While no signal is observed for pristine devices, a signal 50 x above noise level is observed for the doped devices..... 105

Figure 6-7. a) A series of schematics of devices with MoS₂ channel and Ti/Au contacts, MoS₂ channel with EG contacts, and EG channel with Ti/Au contacts. b) The sensing characteristics of the three types of devices under exposure of 100ppm TEA/N₂, plotted in log scale for easier comparison. The graphene channel does not exhibit any sensing, while the Ti/Au-contacted devices exhibit higher overall signal and S/N in comparison to EG-contacted devices. 108

Figure 6-8. a) A cross sectional schematic of MOCVD MoS₂ devices and the corresponding saturation signal as a function of channel length for devices exposed to 10 ppm (light gray), 100ppm (black), and 1000ppm (red). The inset shows the same data on a log plot. b) A cross sectional schematic of a polymer covered MOCVD MoS₂ device and the corresponding saturation signal as a function of channel length for 1000ppm exposure. 109

Figure 6-9. a) Saturation signal of 13 μm MOCVD MoS₂ sensors as a function of TEA concentration with and without microscope lamp illumination. b) The spectrum of the halogen lamp used in Sherlock. Wavelengths strong enough to desorb O₂ is marked (adapted from reference ²⁴⁹). 111

LIST OF TABLES

Table 3-1. A table of the photoresist stack, exposure, and developing information used for the various fabrication processes. Parameters not listed in this table, such as soft bake temperature of developer type, is constant for all processes ^{176,177}	47
Table 4-1. A table showing the equation and parameters used for the calculations for gravitational and buoyant forces in competition with DEP forces during assembly ^{185,190,191}	64
Table 4-2. Details of the peak fitting of the exciton and trion peaks in the WS ₂ PL spectra shown in Figure 4-6 above.	73
Table 6-1. Comparison of triethylamine sensors in literature (top half) to the sensors in this work (bottom half). While some literature report higher signals, sensors in this work perform at room temperature, and exhibit promise for signal and detection limit improvements. Detection limits listed in () specifies the minimum tested concentration.....	113

ACKNOWLEDGEMENTS

My time as a graduate student in the Materials Science and Engineering at the Pennsylvania State University have been filled with technical, professional, and personal challenges. However, my experience has been rewarding, and I have felt myself grow in many ways due to the tremendous support of friends, family, mentors, and colleagues. First, I would like to acknowledge Prof. Joshua A. Robinson for his support and teachings. His patience and guidance have kept me grounded through the ups and downs of my research, and his constant encouragement to push the boundaries of my thoughts have been an invaluable lesson in both technical and professional ways. I'd also like to express gratitude for the welcoming way he approaches his group, which has built the strong, cooperative culture of the Robinson group.

I am also grateful for Dr. Theresa Mayer for having guided and supported the beginning of my graduate studies, and giving me an opportunity to come to Penn State to pursue my doctorate degree. I'd also like to thank Prof. Mauricio Terrones, Prof. Christine Keating, and Prof. Aida Ebrahimi for their mentorship through my studies and thesis research.

While a thesis is defined as the culmination of personal research, I would not have been able to achieve the work discussed here without the help of collaborators and mentors. I'd like to acknowledge the guidance of Jie Li and Scott Levin through the first years of my studies and Julien Frougier for helping cultivate my scientific independence. I'd like to thank Shruti Subramanian for being a supportive, energizing, and encouraging partner for the majority of my latter years of study. I'd also like to thank my collaborators and colleagues for their support and aid: the members of the T.S. Mayer group, including Lan Lin, Xuexue Guo, Liu Liu, and Oren Gall; Colleagues and staff of the nanofabrication center, including Michael Labella, Guy Lavallee, Bill Drawl, Andy Fitzgerald, Bangzhi Liu, Kathy Gehoski, Shane Miller, Beth Jones, Michael Barth, Rahul Pandey, Matthew Hollander, and Daniel Schulman; my colleagues in the J.A. Robinson group, including Yu-chuan Lin, Ganesh Bhimanapati, Chia-hui Lee, Brian Bersch, Kehao Zhang, Rui Zhao, Natalie

Briggs, Nick Simonson, Azim Kozhakhmetov, Max Wetherington and Bhakti Jariwala; staff of the Materials Research Institute, including Haiying Wang, Ke Wang, and Tim Tighe; Penn State-based collaborators including Zhong Lin, Prof. Ray E. Schaak, Xuefei Liu, Prof. Suman Datta, Matthew Jerry, and Nikhil Shukla; External collaborators including Ke Xu and Prof. Susan Fullerton-Shirey of University of Pittsburgh, Jun Li, Dacen Waters, and Prof. Randall Feenstra of Carnegie Mellon University, Mina Asghari Heidarlou and Prof. Alan Seabaugh of Notre Dame University, Frank Keith Perkins and Paul Campbell of the Naval Research Labs, and Nicholas Glavin, Steve Kim, Christopher Muratore, Michael Brothers, Rahul Rao, and Drake Austin of the Air Force Research Labs.

In addition to professional colleagues, I'd like to thank my close friends and family for their support and understanding through my journey. I'd like to express sincere gratitude to my parents, Mei Chen and Jeffrey Deng, for providing the push towards my scientific studies, as well as my brother Yitz Deng for his moral support. I'd like to thank my friends, especially Meng Wang, Elizabeth Zeng, Welley Loc, Austin Ross, and Jason Chan for their friendship and unwavering support in my well-being. Finally, I'd like to thank Ian Ma for his companionship and understanding of my personal and professional goals, as well as challenging me to continue to be a better person and pursue my mental and physical well-being.

Chapter 1

Introduction

1-1. Moore's law

Current technology is established on silicon (Si)-based logic devices, leading a semiconductor industry worth 412.2 billion U.S. dollars in 2017¹. The success of Si, despite not being the most ideal material for electronics, is largely due to the quality of the oxide formed when exposed to high temperature oxidative environments^{2,3}. Improvements to computational power of microprocessors thus far have relied on scaling down the size and increasing the numbers of metal-oxide-semiconductor field effect transistors (MOSFETs), the basic components of a microprocessor. In short, modern microprocessors are more powerful than those of the past largely because there are more switches within it. Historically, the density of MOSFETs has doubled every 2 years; this trend, illustrated in Figure 1-1, is known as “Moore’s Law”⁴, though it is an empirical observation of technological advancements rather than a physical law.

Moore’s Law has become increasingly difficult to maintain with further scaling; at smaller device sizes (the state-of the-art transistors are now at the 7 nm node⁵), many non-idealities stemming from quantum mechanics that are negligible at larger sizes, including effects of high leakage currents and drain-induced barrier lowering^{6,7}, become detrimental to the device performance. Thus far, such issues have been circumvented through various means, including the replacement of SiO₂ with high-k dielectrics at the 45 nm node and a shift in device design to the FinFET, where the channel is surrounded on three sides with dielectric, at the 32 nm node^{8,9}. However, as FET size continues to shrink, the scaling challenges become nearly insurmountable, and large overhauls to logic devices may be necessary in order to increase the computational value of Si-based MOSFETs.

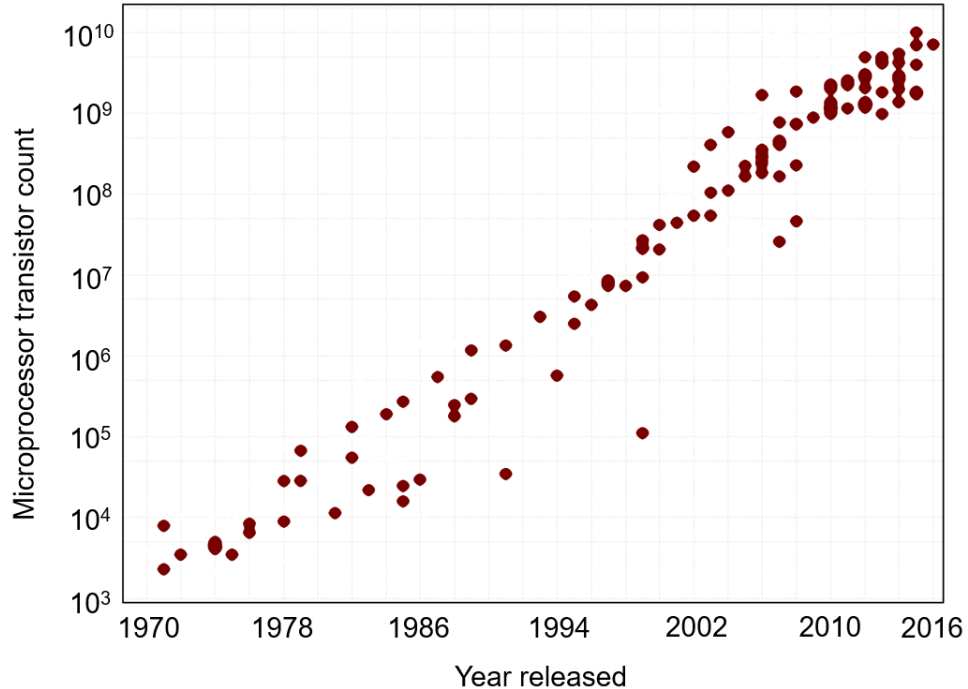


Figure 1-1. A plot showcasing the number of transistors on a single microprocessor from 1970 to 2016. The transistor count is plotted in log scale, showcasing the exponential increase in the transistor count over the years (adapted from reference ¹⁰).

While further improvement of the computational value of semiconductor chips (a push known as “More-Moore”) is important for technological advancements, there is another complimentary direction of improvement; this area is known as “More-than-Moore” (MtM), and it describes the push to increase the functionality of a microprocessor beyond computational power ^{4,11}. As illustrated in Figure 1-2, much of MtM is dedicated to furthering the communication between the microprocessor and the world around it, through devices such as signal modules or sensors, in a way that allows the microprocessor to respond to changes in its environment in real-time. MtM allows the total value of the microprocessor to increase independently to its processing power.

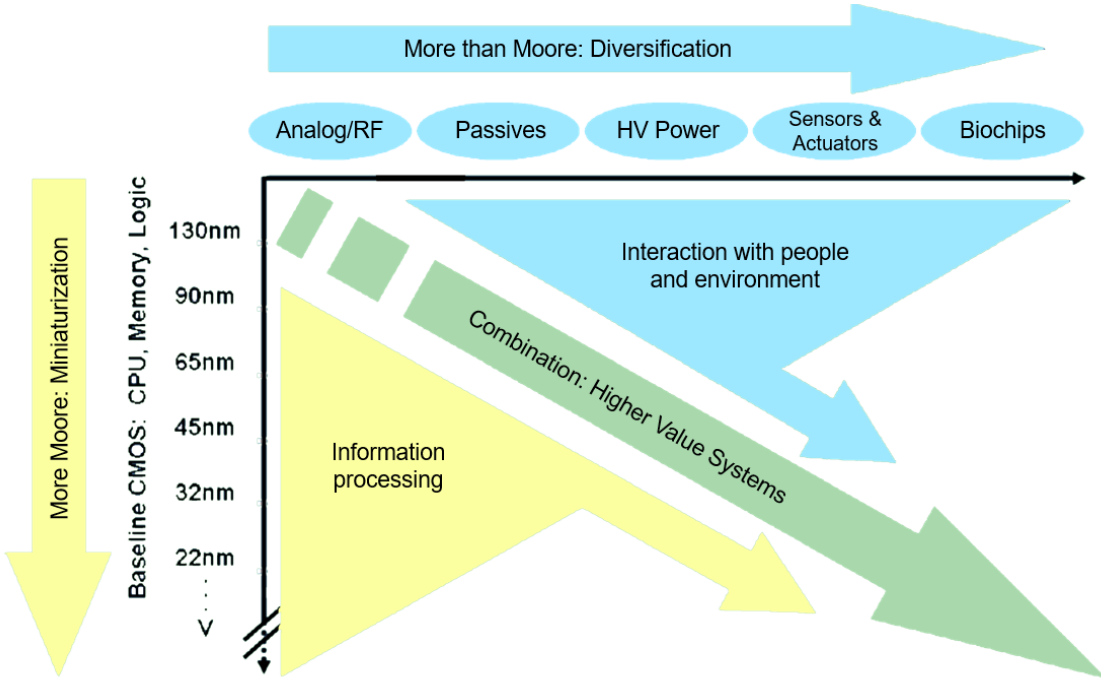


Figure 1-2. An illustration of the combined push for higher value systems through “More-Moore” (further scaling of microprocessor components) and “More-than-Moore” (diversification of the functionalities of microprocessor components) (adapted from reference ⁴).

1-2. Two-dimensional materials

As mentioned briefly earlier, silicon is intrinsically a non-ideal material for many functionalities despite its pervasiveness in a wide range of electronics. Si is an indirect band gap semiconductor, meaning the lowest energy state of the conduction band and the highest energy state of the valence band do not overlap in momentum space ³. This leads to inefficient energy transfer for many applications; In order for an electron to be energized into the conduction band, it requires either higher energy input than its bandgap size or the assistance of a phonon ¹².

One of the families of materials that have attracted attention for moving beyond Si in the MtM push is 2-dimensional (2D) materials. These materials are made of layers only a few atoms thick with no direct interlayer bonding ¹³. Due to the large surface-to-volume ratio and unique physical and optoelectronic properties, they offer novel functionalities and could prove to be better

candidates for MtM devices in comparison to Si^{14–16}. While 2D materials were known to the scientific community in theory^{17,18}, they were suspected to be unstable until 2004 when Novoselov and Geim successfully isolated a single layer of carbon atoms from graphite, now known as graphene¹⁹. Since this discovery, many unique properties of graphene have been reported, including high tensile strength²⁰, flexibility^{21,22}, high mobility^{23,24}, and chemical stability²⁵. While these observations brought about a surge of interest in this material for a wide range of applications, its intrinsic lack of a bandgap was a disadvantage in utilizing graphene as the electronic functional material in device applications^{26,27}. Instead, researchers looked toward related materials, the 2D transition metal dichalcogenides (TMDs). This family of materials, some of which are listed in Figure 1-3, exhibit a wide range of properties, and among them are a series of semiconducting materials. Like graphene, these materials can be exfoliated from bulk crystals, are flexible, and have unique properties stemming from their layered structure^{13,28,29}. In addition, their properties are dependent on the number of layers in the film and tunable to the requirements of the application. Furthermore, these materials can be layered on top of each other to produce van der Waals heterostructures with unique interlayer coupling or transport properties^{30,31}.

Since then, demonstrations of potential applications using the novel properties of 2D semiconducting TMDs have been reported, including conventionally structured transistors, optoelectronics, and sensors, as well as new device structures using the thin form of the 2D TMDs^{32–37}. However, in contrast to the field of Si devices, which have been studied since the mid 1900's, single- to few-layer TMD-based devices were not demonstrated until shortly after the successful isolation of graphene^{38,39}, and the field of 2D TMD-based devices is still relatively new and much remains to be understood. For instance, due to the unique structure of 2D materials, namely their large surface-to-volume ratio, it is found that the processing and device fabrication techniques can heavily affect the transport characteristics of the resulting device^{37,40}. The goal of this dissertation is to detail my research on the integration and fabrication of 2D TMDs into electronic devices, focusing on the effect of material property and processing techniques on the device transport

characteristics in order to further the understanding of the role 2D materials can play in the MtM landscape.

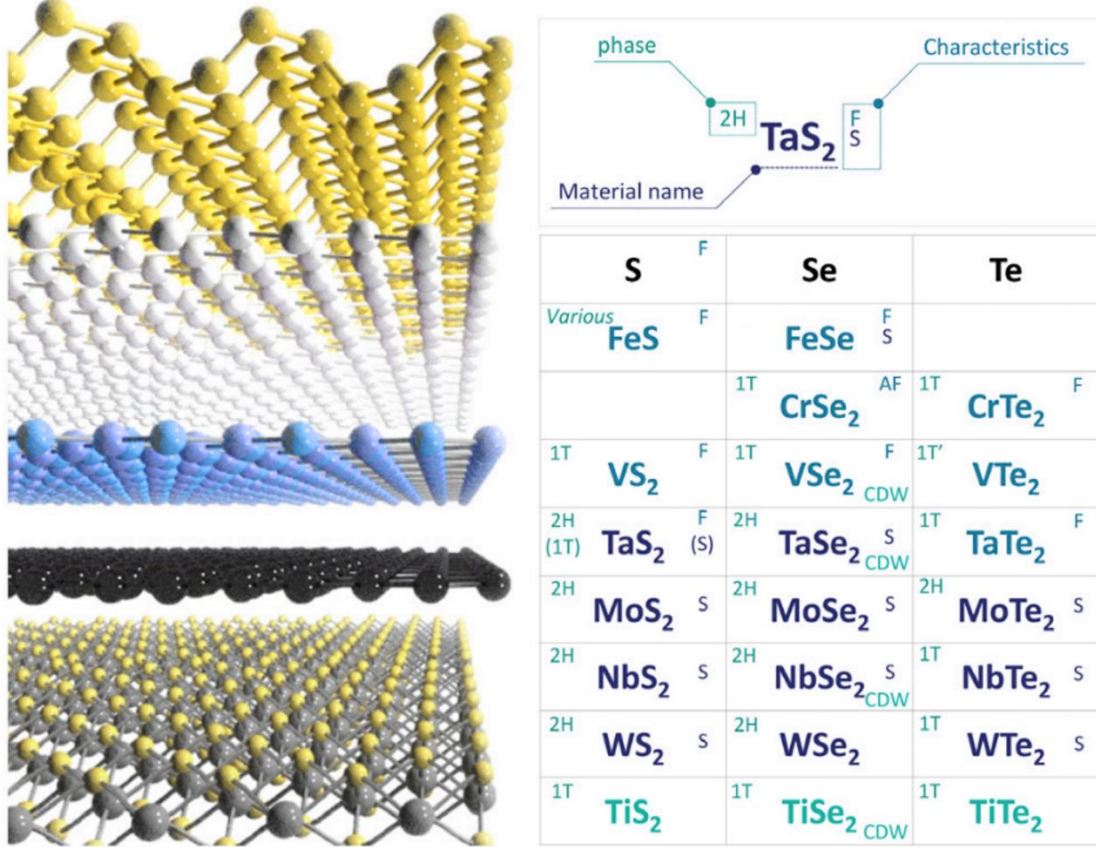


Figure 1-3. A schematic of various 2D materials and a table of 2D TMDs listed with their characteristics, including crystal structure and other various properties: ferromagnetism (F), anti-ferromagnetism (AF), superconductivity (S), and charge density wave (CDW) (adapted from reference ²⁹).

Chapter 2

2-Dimensional Materials: Introduction to Materials and Devices

2-1. 2-dimensional transition metal dichalcogenides

2-1-1. Introduction to semiconductors

While electrons bound to a lone atom in free space have discrete energy levels approximated by the Bohr model, an electron in a periodic crystal lattice is subject to interactions with neighboring electrons and atoms³. These interactions lead to a splitting of the original energy states, creating bands of discrete but tightly stacked energy states, shown in Figure 2-1a⁴¹. The electronic properties of a material are determined by the band structure and where the fermi level, the highest occupied energy state at absolute zero, lies within it. Figure 2-1b shows the 3 basic configurations that can occur, corresponding to conductors, insulators, and semiconductors.

In reality, the crystal structure of a material is not perfectly repetitive; defects, including misalignment of the crystal structures, vacancies, or even foreign elements, may exist in the material. These disturb the crystal structure and thus the energy levels, creating energy states within the band, leading to shifts in the fermi level within the band and changes in its electrical properties⁴². Some of these defects can be precisely controlled. For example, controlling the concentration of foreign dopants that inject negatively or positively charged carriers, electrons or holes, in semiconductors can directly affect the electronic transport properties of the material, part of which manifests in its conductivity σ :

$$\sigma = q(n\mu_e + p\mu_h) = 1/\rho \quad \text{Eq. 2-1}$$

where q is the electrical charge ($1.6 * 10^{-19}$ coulombs), n and p are the carrier concentrations of electrons and holes respectively, and μ_e and μ_h are the mobilities of electrons and holes respectively within the material⁴³. The resistivity ρ is defined as the inverse of the conductivity.

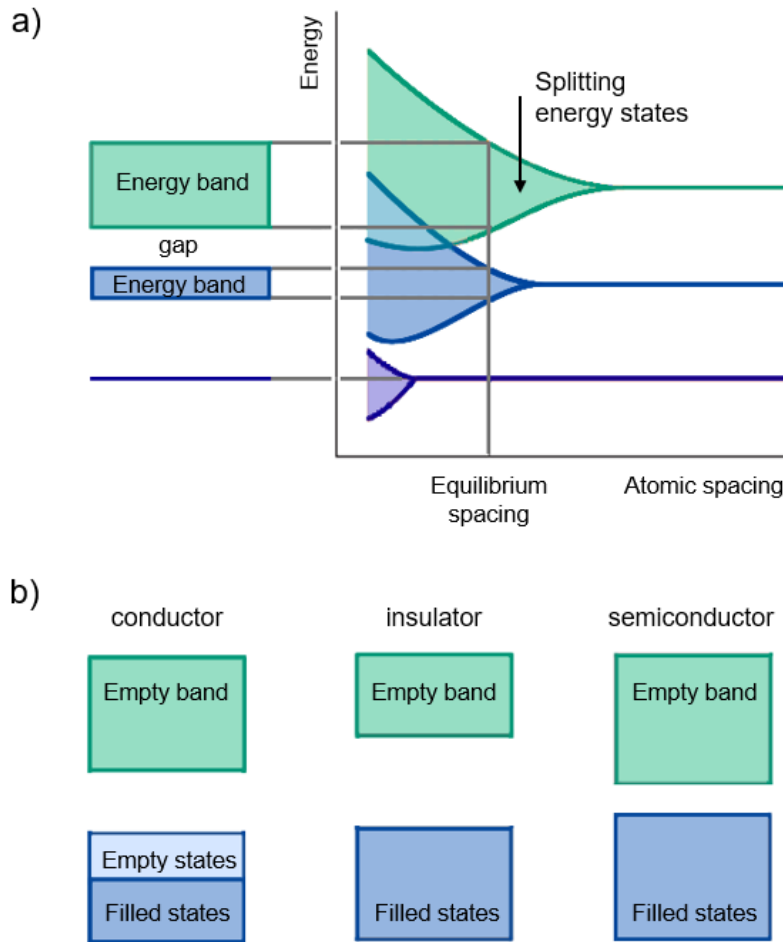


Figure 2-1. a) An illustration of the spreading of energy states for an atom as a function of interatomic spacing. b) Three types of band structures for conductors, insulators, and semiconductors. (Both a) and b) adapted from reference⁴¹)

2-1-2. Introduction to 2-dimensional materials

In their bulk crystalline form, 2D materials are stacks of atomically thin layers that are self-confined without electronic bonds extending out of the plane of each layer. Instead, these layers are held together by van der Waals forces¹³. The first material in this family to be isolated is graphene, made up a single atomic thick layer of sp² hybridized carbon atoms that extend out laterally in a hexagonal honeycomb structure, illustrated in Figure 2-2a⁴⁴. Due to the strength and elasticity of these carbon bonds, graphene is physically robust, boasting an experimental lateral

tensile strength of 130 GPa²⁰. In addition, this ultra-thin and elastic structure of graphene makes it highly flexible, an attractive property for flexible or wearable electronics^{45,46}. Beyond its intriguing physical properties, its high thermal conductivity^{47,48}, transparency⁴⁹, and chemical inertness^{25,50} make graphene a material of interest for many applications.

While the physical properties of graphene have garnered attention, much of graphene's popularity comes from its unique electrical properties. The honeycomb structure leaves an extra electron, a π -bond, out of the graphene layer plane. This electron is free to move about the layer surface, resulting in the high conductivity of graphene, with experimentally reported mobility values of up to $200,000 \text{ cm}^2 \text{ V}^{-1} \text{ s}^{-1}$ at low temperatures^{23,24}. However, the graphene electronic band structure reveals that the material is semi-metallic; its valence and conduction bands come to a point at the fermi level, forming a Dirac cone (illustrated in Figure 2-2b)^{51,52}. This lack of band gap and corresponding device leakage currents due to Klein tunneling, where electrons travel through large potential barriers more efficiently than in conventional non-relativistic tunneling, limit the application of graphene as a functional material for many electronic devices^{53,54}.

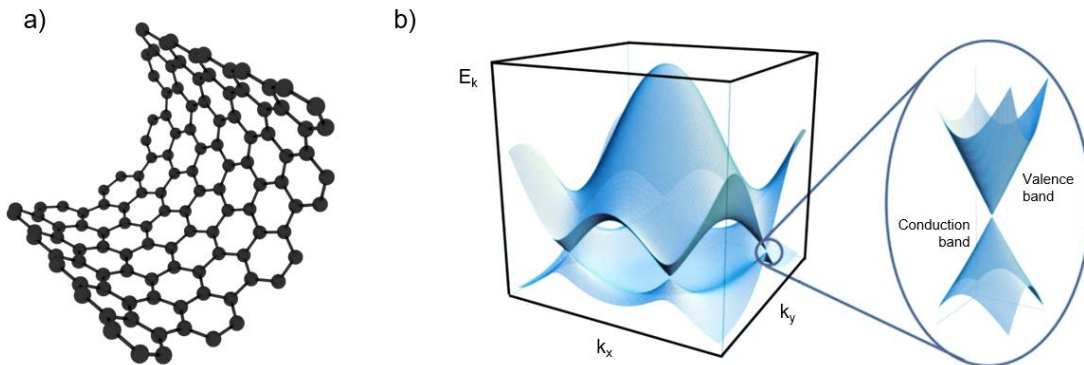


Figure 2-2. a) An illustration of the honeycomb crystal structure showcasing flexibility of a graphene sheet. b) A map of the electronic band structure of graphene, showing the Dirac cones where the conduction and valence bands come to a point (adapted from reference⁵¹).

With the realization that the intrinsic properties of graphene were non-advantageous as the functional material in many electronic devices, researchers turned to a family of related materials, the transition metal dichalcogenides (TMDs). These materials structurally differ from the single

atom thick layers of graphene; instead, they are made of a layer of transition metal (M) sandwiched by two layers of chalcogenide (X) atoms, forming a MX_2 chemical formula^{17,28}. The two main types of structures observed in this family are 2H, where the three atomic layers stack in an ABA configuration such that the chalcogen atoms are aligned in the vertical plane, and 1T, where the two chalcogen layers are shifted such that the stacking is in an ABC configuration (illustrated in Figure 2-3a)⁵⁵. In both structures, the chalcogen atoms are bonded only to the central metallic layer, such that no bonds extend beyond these three layers. Like graphene, each of these layers are held together by van der Waals forces²⁹.

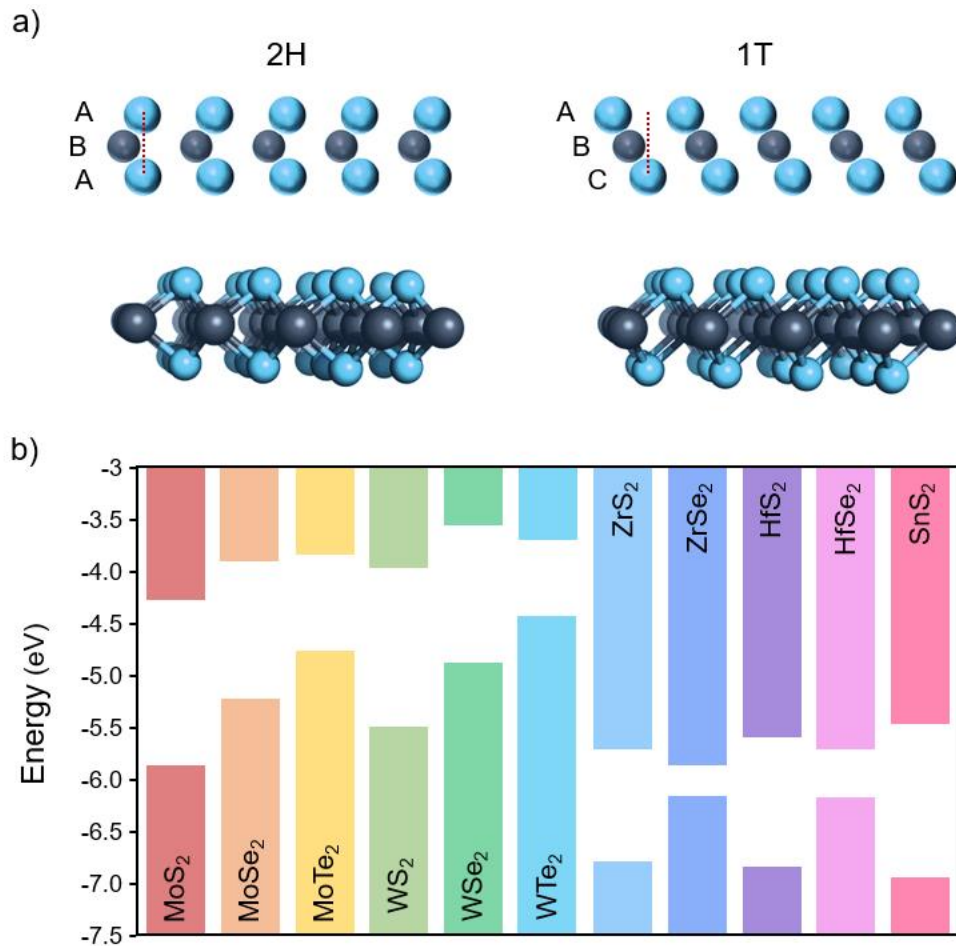


Figure 2-3. a) An illustration of the 2H and 1T structures, illustrating the alignment of the chalcogen (blue) atoms relative to the metal (gray) atoms (adapted from reference⁵⁶). b) A survey of bandgaps of various 2D materials. The wide range of alignment allows for the fabrication of various types of heterostructures (adapted from reference⁵⁷).

Unlike graphene, the materials in the 2H TMD family, including intrinsic MoS₂ and WSe₂, are semiconducting with bandgaps ranging from 0.5eV for ZrSe₂ to 1.94 eV for monolayer WS₂, illustrated in Figure 2-3b⁵⁸⁻⁶⁰. In addition, the band structure and therefore the electronic properties of these materials are thickness dependent. For example, MoS₂ in its bulk form is a semiconductor with 1.23eV band gap, which increases and becomes a direct band gap of 1.8eV at a single layer; this allows for the tunability of the material properties based on the needs of the specific application⁶¹. Among the 2D TMDs, MoS₂ in particular have attracted much attention in the field, with reported mobility values up to 517 cm² V⁻¹s⁻¹ and transistor on/off ratios of up to 10⁸, making it a promising material for electronic applications^{62,63}.

2-2. Synthesis and integration of 2-dimensional transition metal dichalcogenides

While most 2D materials are available naturally, they are found in bulk crystalline forms made of domains of stacked layers. Graphene was first isolated experimentally from graphite in 2004 using the “Scotch tape method”¹⁹. In this method, a piece of graphite is sandwiched between two adhesive sides of common tape, and pulled apart such that the graphite piece splits in the plane of the layers. This can be repeated until the graphite is thinned to only a few layers of graphene, at which point the flake is transferred onto a substrate (Shown in Figure 2-4). Because the adhesion between the graphene surface to the substrate is stronger than the van der Waals forces between the graphene layers themselves, this leaves ultra-thin layers of graphene on the target substrate. This method has been extended to nearly all 2D materials and is the preferred way to isolate these layers for exploration of their unique phenomena.

While this process can produce large single crystalline sheets of 2D material, it is non-ideal for scaling to industrial levels of output as it requires optically mapping the substrate for transferred flakes and designing the devices around targeted flakes^{39,64,65}. The process usually yields low number of devices per transfer and can be highly time consuming. Rather than using such top-down

techniques, bottom-up growth methods to depositing large area growth of 2D materials have been the main focus for material synthesis for device applications in recent years^{29,66,67}. This section will discuss several transfer techniques for 2D materials and then provide an overview of bottom-up growth methods.

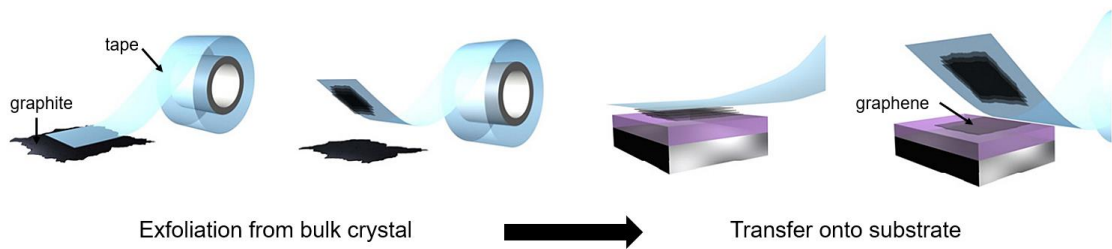


Figure 2-4. An illustration of the scotch tape method for exfoliating mono- to few-layer graphene (adapted from reference⁶⁸).

2-2-1. 2-dimensional material transfer methods

Due to the simplicity of dry exfoliation methods (such as the scotch tape method), much of mono- to few-layer 2D material-based devices reported in literature have been produced using such top-down methods. While bottom-up growth methods have continued to improve, with wafer-scale growths now achievable, these often require transfer off of its growth substrate onto a more ideal substrate on which electronic devices could be fabricated^{69,70}. For example, materials are often transferred from conductive or entirely insulating substrates onto SiO₂/Si substrates in order to allow back gating of devices built around the material^{19,40,64,65}. In addition, transferring material can be attractive for applications where the material growth process is not compatible with the substrate. For example, it can be useful for structurally complicated devices that require underlying circuitry or components that may not survive 2D material growth conditions^{71,72}. It is particularly

useful for heterostructures where the growth of subsequent layers may affect or damage the underlying layers on the substrate^{33,54,73}.

Large area transfer of 2D materials

There are two common methods to transfer films of 2D materials: The wet transfer process and the dry transfer process. In both cases, the starting material is isolated on a handling layer via exfoliation from bulk or by separating the material from its growth substrate by etching away a sacrificial growth substrate (an example process, used in this dissertation, is described in Section 3-3-1). In a wet transfer process, the handling layer is placed in water with the material on the bottom surface; the handling layer floats on the surface of the water. The entire layer is then fished out from underneath by the target substrate, then cleaned of the polymer handling layer such that only the material remains on the target substrate^{74,75}. This process is quick and simple, but offers no control of the final positioning of the material. While this is not an issue for device arrays if the grown film is fully coalesced, the same cannot be said for films with isolated domains of material. In a dry transfer process, the handling layer with the material side down is positioned directly on the dry target substrate. The transfer relies on the adhesion of the TMD to the substrate over the handling layer or additional layers of material^{68,76}. Using this method in conjunction with precision manipulators allows for more accurate positioning, but it is time-consuming and non-scalable as only one domain can be controllably positioned at a time^{77,78}. The term “dry transfer” is more often used to refer to the deterministic transfer method utilizing manipulators.

Dielectrophoretic assembly

In addressing the non-scalability of the wet and dry transfer methods, additional transfer methods with roots in transfer of non-2D materials may be applied to 2D materials. One such method is the directed self-assembly of particles with dielectrophoretic (DEP) forces⁷⁹⁻⁸¹. This technique relies on the forces on a dipole induced in a colloid suspended in a liquid medium in a non-uniform electric field to drive the particles to regions of interest.

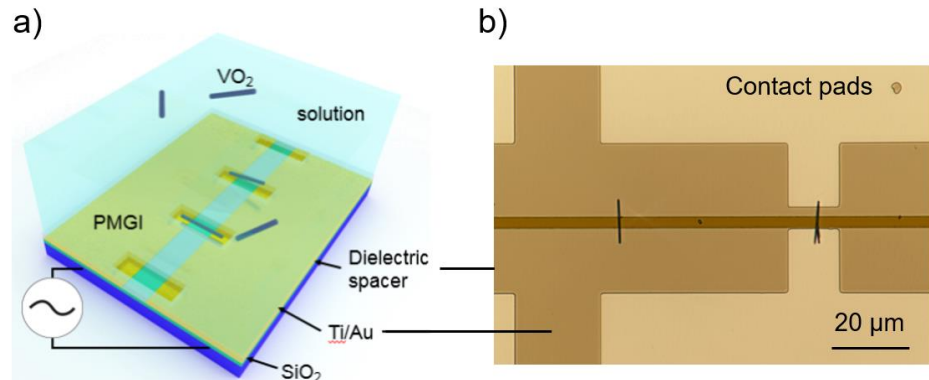


Figure 2-5. a) schematic of a parallel electrode assembly system with VO₂ nanorods suspended in a solution. b) an optical image of VO₂ nanorods assembled on the electrode gap in a perpendicular configuration (D. Deng, unpublished).

Dielectrophoretic assembly is often utilized for the positioning of 1D nanorods and tubes, as they can exhibit large dipole moments ideal for DEP assembly ^{79,80}. An example of such assembly is shown in Fig 2-5, where solution synthesized VO₂ nanowires by Xuefei Li of the Raymond E. Schaak group are positioned across a simple parallel electrode structure. While spherical particles and nanoplates have also been assembled using DEP, assembly of 2D materials have been limited to plates of large number of layers or small sub-micron flakes of mostly chemically synthesized material ⁸²⁻⁸⁴. Furthermore, the focus has been on graphene and reduced graphene oxide (rGO), with little work done on the assembly of monolayer TMD flakes ^{85,86}. However, since the basic physics of DEP assembly relies simply on induced dipoles and electric fields, it is expected that 2D materials can assemble in similar ways to its 1D or nanoplate counterparts, making DEP assembly a potential scalable alternative to other transfer techniques.

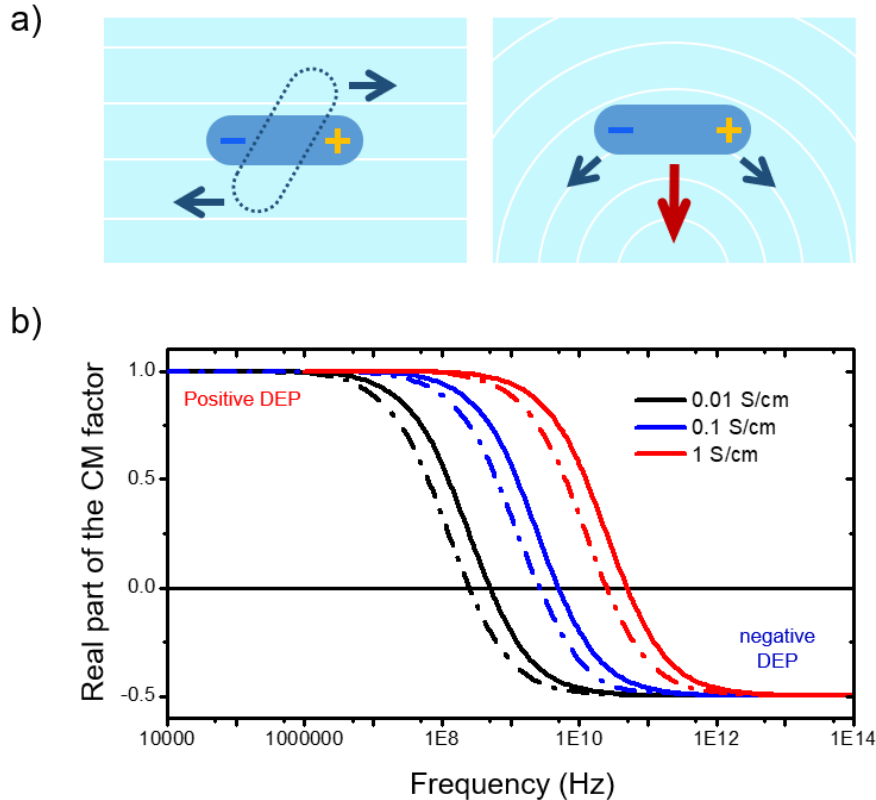


Figure 2-6. a) Schematics of a particle in uniform and non-uniform electric field. In a uniform field, the particle may see a rotational torque, but there is no net force on the particle. In a non-uniform field, forces on the particle do not cancel out and thus there is a finite force on the particle. b) A plot of the real part of the CM factor as a function of AC bias frequency for assembly of MoS₂. The plot also illustrates the effect of the material conductivity on the CM factor (D. Deng, unpublished).

When a particle of an arbitrary shape is placed in a uniform electric field, as illustrated in Figure 2-6a, the electric field induces a dipole within the material that leads to forces on each end of the dipole, creating a torque that orients the particle along the electric field⁸⁷. When the particle is aligned, the forces on each end of the dipole are equal and opposite, such that the total net force on the particle due to the electric field becomes zero⁸⁸. However, in a non-uniform electric field, the forces exhibited on the dipole no longer cancel out, leading to a non-zero net force on the particle. This causes the electric field to drive the dipole through space. This net force is called the dielectrophoretic force and can be described by equation 2-2:

$$\langle F_{DEP} \rangle = \Gamma \varepsilon_m \operatorname{Re} \left\{ \frac{\varepsilon_p^* - \varepsilon_m^*}{\varepsilon_p^* + 2\varepsilon_m^*} \right\} \nabla |\vec{E}|^2 \quad \text{Eq. 2-2}$$

Γ is a factor that describes the shape and size of the particle, ε_m is the dielectric permittivity of the medium, and $\nabla |\vec{E}|^2$ is the gradient of the electric field squared. $\frac{\varepsilon_p^* - \varepsilon_m^*}{\varepsilon_p^* + 2\varepsilon_m^*}$ is also known as the Clausius-Mosotti (CM) factor, and ε_p^* and ε_m^* are the complex permittivities of the particle and the medium respectively. The CM factor is a frequency dependent factor that determines the sign, and therefore the direction, of the DEP force. Figure 2-6b shows a plot of the real portion of the CM factor calculated for MoS₂ at varying conductivity values as a function of the frequency of the AC field. The CM is positive at lower frequencies ($<10^7$ for the conductivities used), resulting in a positive F_{DEP} and attraction of the particle to regions of high field gradient. At higher frequencies, the CM factor decreases until it reaches negative ($>10^{11}$ for the conductivities used) and the opposite is true, with particles being repelled from regions of high field gradient due to a negative F_{DEP} .

2-2-2. Bottom-up growth of transition metal dichalcogenides

Several bottom-up growth techniques have been reported for TMDs ⁸⁹. Molecular beam epitaxy (MBE) is a slow method of TMD growth, but provides precise control of the stoichiometry and species being deposited, allowing for the growth of atomically sharp van der Waals heterostructures ⁹⁰⁻⁹². Atomic layer deposition (ALD), where single layers of atoms are introduced into the growth chamber and reacted, can also be used to produce films of TMDs ^{93,94}. Other methods with less direct approaches, such as wet chemical synthesis ^{95,96} or physical deposition and subsequent annealing ^{97,98} have also been reported. However, vapor deposition techniques are most commonly used for producing large area TMD films for device fabrication. The TMD materials

used in this dissertation are produced using two methods of chemical vapor deposition (CVD): powder vaporization (PV), and metal-organic chemical vapor deposition (MOCVD).

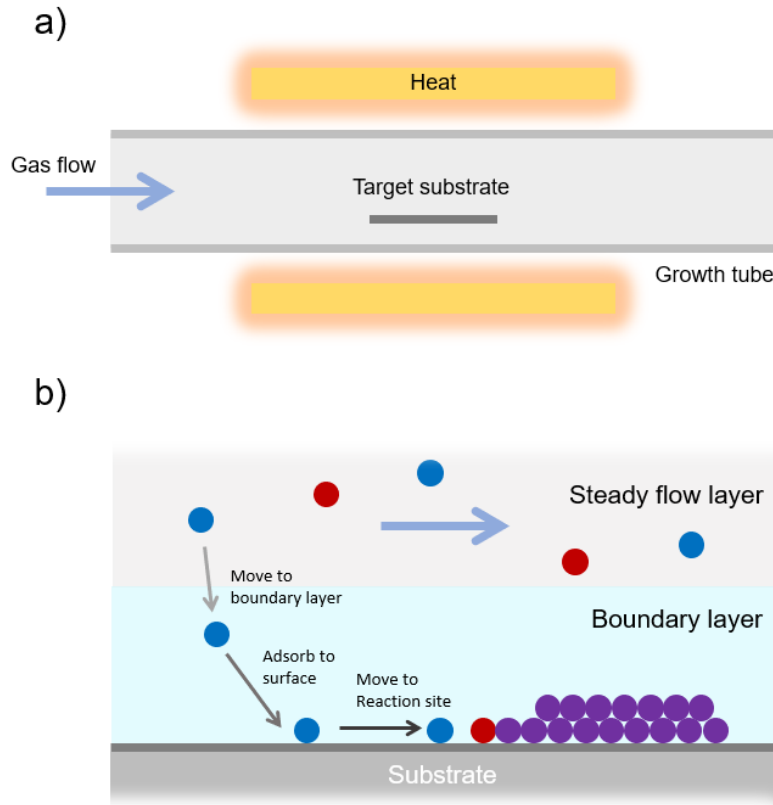


Figure 2-7. a) A schematic of a hot-wall CVD reactor. b) A simplified schematic of the chemical vapor deposition process, showing the transport of a precursor into and through the boundary layer, adsorption on to the substrate surface, and the transport across the substrate surface until it reacts into the targeted product.

Chemical vapor deposition utilizes a system where gas phase precursors are flowed over a heated target growth substrate, upon which the precursors adsorb and react to produce a film ⁹⁹. Figure 2-7 illustrates a basic schematic of a hot wall reactor, the types of furnaces used in this dissertation, and a schematic of the steps in a CVD process. First, precursors are transported to the boundary layer, which is a region directly above the substrate where the changes in flow dynamics and substrate surface reactions result in a region that differs from the rest of the tube in gas velocity, concentration, etc. The precursors are then transported towards the substrate, adsorb onto the surface, and react for the nucleation or growth of the target film ¹⁰⁰. Each of these steps are

dependent on many factors, including temperature, pressure, precursor and gas concentrations. While trends for these factors generally remain constant, i.e. lower temperature growths tend to result in lower crystallinity of the film due to the lower mobility of precursors at the surface, differences between growth systems make CVD growths unique to each furnace²⁹.

In powder vaporization techniques, the metal precursor is a solid powder. For example, the MoS₂ PV growths used in this dissertation utilizes MoO₃ as its Mo source. The morphology is heavily dependent on the relative partial pressures of the precursors which are controlled by separately manipulating the temperature of the chalcogen precursor. As the powders are heated and vaporized, they are carried downstream and react on the substrate surface, or above it before being deposited onto the substrate. Furthermore, non-uniformity in the vaporized powder partial pressures as a function of lateral location across the sample has been reported¹⁰¹. This leads to non-uniform deposition of the material on the substrate as a function of its position down the growth tube, often creating a “plume” of growth as illustrated in Figure 2-8a.

Though the morphology of MoS₂ is heavily related by the relative partial pressures of its precursors, it is difficult to precisely control, as the rate of powder vaporization is highly sensitive to factors out of the growers’ control, including powder particulate size. In cases where uniform control of the precursors is necessary, MOCVD methods are utilized instead. In this method, the precursors are not powders heated in the growth tube, but introduced in vapor form through an external line; the name of the method derives from the use of metal-organic compounds such as Mo(CO)₆ as its metal source. These compounds are transported through the system on a carrier gas. Because the precursor can be carefully controlled via a mass flow controller, this growth process allows for greater control and uniformity of growth in comparison to PV methods. In fact, MOCVD growth has been demonstrated to produce extremely uniform growths over waver scale⁷⁰. Figure 2-8 illustrates the growth set up, morphology, and resulting stoichiometry of PV and MOCVD growths for the deposition of MoS₂ on SiC and sapphire substrates respectively (see Section 3-3 for methods). Figure 2-8e & f shows X-ray photoemission spectra (XPS) of PV and MOCVD growths

provided by Shruti Subramanian and Kehao Zhang from the J. Robinson group respectively. It is observed that the PV process produces MoS₂ that is naturally more sulfur deficient, with a Mo:S ratio of approximately 1:1.8, while the MOCVD process produces more stoichiometric materials with Mo:S ratios near 1:1.98.

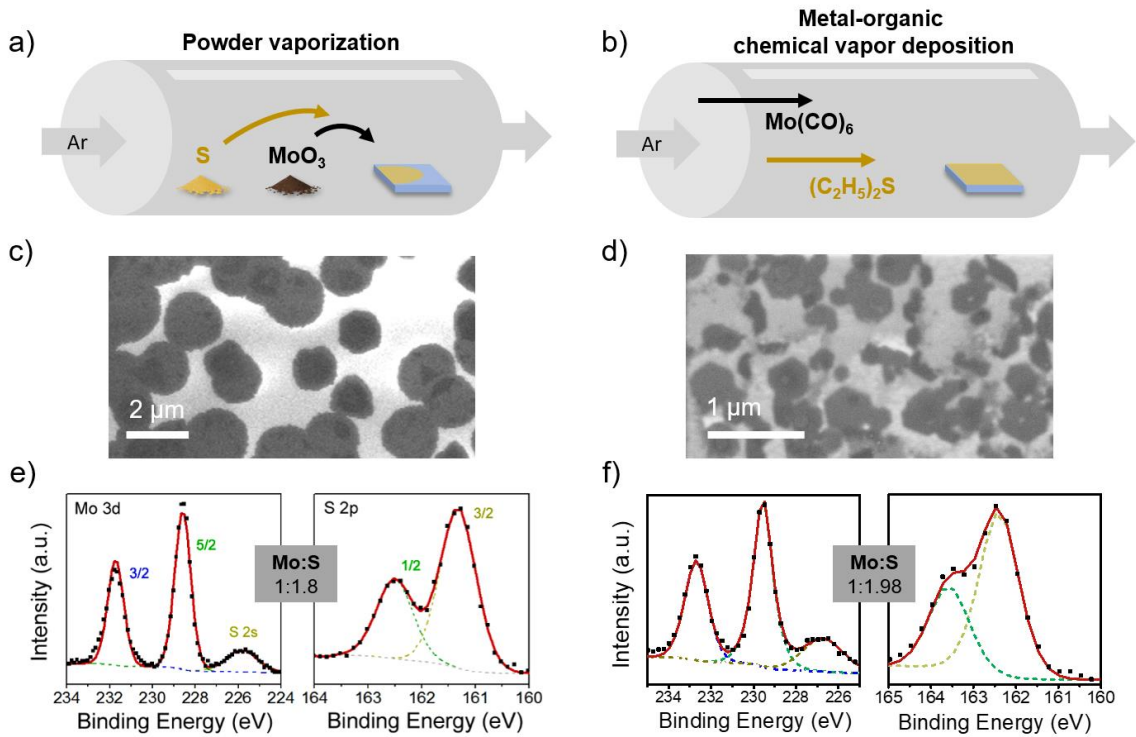


Figure 2-8. A comparison of an example set of PV and MOCVD processes, illustrating the growth set up (a & b), SEM images of the growth (c & d), and XPS spectra for Mo 3d and S 2p, with corresponding Mo:S ratio (e & f)¹⁰². In general, MOCVD growths are more uniform and stoichiometric, while PV growths are much faster. (c), (d), and (f): D. Deng unpublished)

While MoS₂ grown for this dissertation behaves n-type as-grown, additional components can be introduced into the growth furnace and thus into the material to produce further n-doped or p-doped materials. For example, introducing Nb, a p-type dopant, into the growth system through NbCl₅, as illustrated in Figure 2-9a, can controllably tune the fermi level in the MoS₂, down to beyond the valence band edge to produce degenerately doped MoS₂. The location of the fermi level relative to the valence band maximum is plotted as function of the Nb at% in the film for various

growth substrates in Figure 2-9b. The amount of Nb can be controlled through the heating temperature and thus the partial pressure of Nb. Specific details of this doping process is discussed in Section 3-3-3.

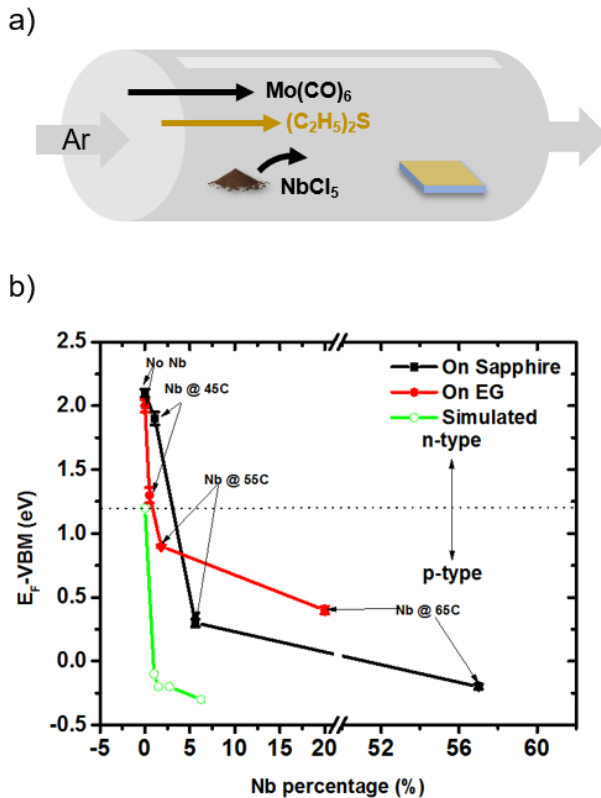


Figure 2-9. a) a schematic of the Nb-doped MOCVD MoS_2 growth set up, showing NbCl_5 powder introduced upstream. b) A plot showing the location of the fermi level within the MoS_2 band gap as a function of at% of Nb on various substrates (K. Zhang, in preparation).

2-2-3. Bottom-up growth of graphene

While CVD graphene is a well-reported method of growth used to produce large area films of graphene, the growth is generally done on a metallic substrate and results in polycrystalline films¹⁰³⁻¹⁰⁷. Another graphene growth process is the epitaxial growth directly on an insulating substrate, producing epitaxial graphene (EG)^{108,109}. SiC-based epitaxial growth is performed in a high temperature furnace, such as the system shown in Figure 2-10a of the furnace used in this

dissertation. The growth begins with a crystalline SiC surface. At high temperatures, Si sublimates off of the surface of the substrate, leaving behind carbon that self-rearranges into graphene, as illustrated in Figure 2-10b. Because this method is a subtractive process where the substrate surface is converted to a graphene film, a buffer layer exists at the interface of the substrate and the graphene film. This layer can be described as defective graphene, partially converted from SiC to the graphene but also partially covalently bonded to the SiC substrate (see Figure 2-10c). This direct interaction and the polarization of the SiC surface due to the sublimation process electrostatically induces n-type characteristic in the graphene above it. Furthermore, by intercalating underneath the buffer layer to separate the graphene from the SiC substrate, the induced electrostatic doping becomes p-type¹¹⁰. This makes EG tunable to the requirements of the application.

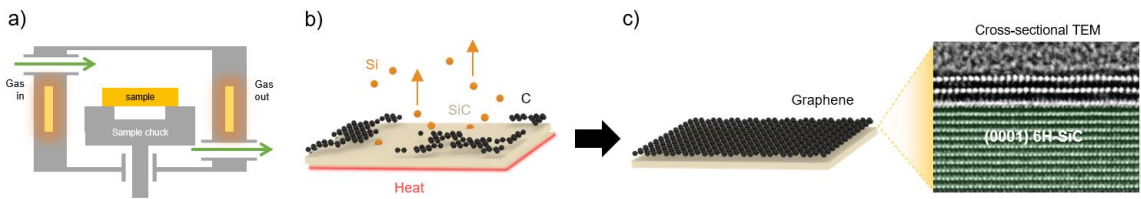


Figure 2-10. An illustration of the growth of epitaxial graphene on SiC, and a cross-sectional TEM showing the graphene layers and the buffer layer. Exact details on the growth and TEM parameters are discussed in Section 3-3-2 and 3-6-1 respectively.

2-3. Introduction to electronic devices

2-3-1. Resistors

The most basic electronic device is a resistor, where a material is placed in line along the path of electrical current such that the motion of electrical charges is impeded by the material. Given a material with resistivity ρ , the total resistance of this component is determined by its physical shape and size¹¹¹:

$$R = \rho \frac{L}{A} \quad \text{Eq. 2-3}$$

where L and A are the length and cross-sectional area respectively of the component through which electrical current passes through, known as the channel, as illustrated in Figure 2-11a. For a sheet-like component where the thickness t is uniform through the channel, a sheet resistance R_s can also be used. R_s describes the resistance through a lateral square of the uniform material measured at opposite corners, but can also be described as the resistivity normalized to the thickness⁴³:

$$R_s = \frac{\rho}{t} \quad \text{Eq. 2-4}$$

This parameter is more straightforward to use for 2D materials, where the thickness of the material is theoretically infinitesimally thin.

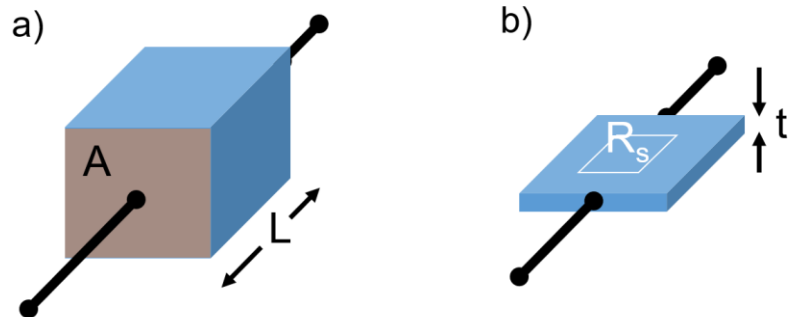


Figure 2-11. a) A basic schematic of a resistor. b) An illustration of a thin sheet-like resistor with a square region governed by R_s .

2-3-2. Metal-semiconductor junctions

While theoretical circuitry assumes no interfaces exist between the circuit components, this assumption fails in experimental devices, where there is a physical disturbance in the atomic structure between the channel material and the conductive contact. Figure 2-12a and c illustrate the band diagram of metals and semiconductors in space. When the materials are brought together, the

carriers on each side flow through the junction such that equilibrium is achieved in the fermi level across the junction. This motion of carriers in the semiconductor at the junction leads to a built-in electric field in the semiconductor due to the remaining immovable atomic charge which offset the motion of charge, shown as a bend in the semiconductor energy bands. The width of this depletion region W_d is given as

$$W_d = \sqrt{\frac{2\epsilon_s(V_{bi})}{qN_d}} \quad \text{Eq. 2-5}$$

where ϵ_s is the permittivity of the semiconductor, V_{bi} is the built-in potential across the depletion width, q is the electronic charge and N_d is the dopant density, assumed to overwhelm the intrinsic carrier concentration in the material such that $n \cong N_d$ ⁴². Depending on the relative positioning of the fermi level in the semiconductor and the metal work function Φ_m , the energy required to free an electron from the metal fermi level into vacuum, metal-semiconductor junctions can have two forms: ohmic and Schottky. In an ohmic junction, there is no barrier-to-transport to the metal as the major carriers follow the band edge of the semiconductor. A Schottky junction, on the other hand, creates a barrier over which electrons need to pass, defined as the Schottky barrier ϕ_B (or SB), equivalent to the difference between the major carrier band (conduction band for n-type and valence band for p-type semiconductors) to the fermi level of the metal:

$$\phi_B = \Phi_m - \chi \quad (\text{for n-type}) \quad \text{Eq. 2-6}$$

$$= (\chi + E_g) - \Phi_m \quad (\text{for p-type}) \quad \text{Eq. 2-7}$$

where E_g is the band gap of the semiconductor and χ is the electron affinity of the semiconductor, the energy required to free an electron from the conduction band edge into vacuum¹². While this is the theoretical value for ϕ_B , in experimental work the value is not quite as simple. χ may not be accurately known, and non-idealities such as Fermi-level pinning, a phenomenon where surface states in the semiconductor due to charges or defects lead to a fixed built-in potential ϕ_{bi} , may

dominate the actual SB height¹¹². The thermionic emission current density over the SB can be expressed as:

$$J = A^* T^2 \exp\left(-\frac{q\phi_B}{kT}\right) \left[\exp\left(\frac{qV_a}{nkT}\right) - 1 \right] \quad \text{Eq. 2-8}$$

where A^* is the Richardson constant, n is an ideality factor, and k is the Boltzmann constant³. This relationship allows the SB height to be extracted through a series of measurements of the junction current as a function of temperature.

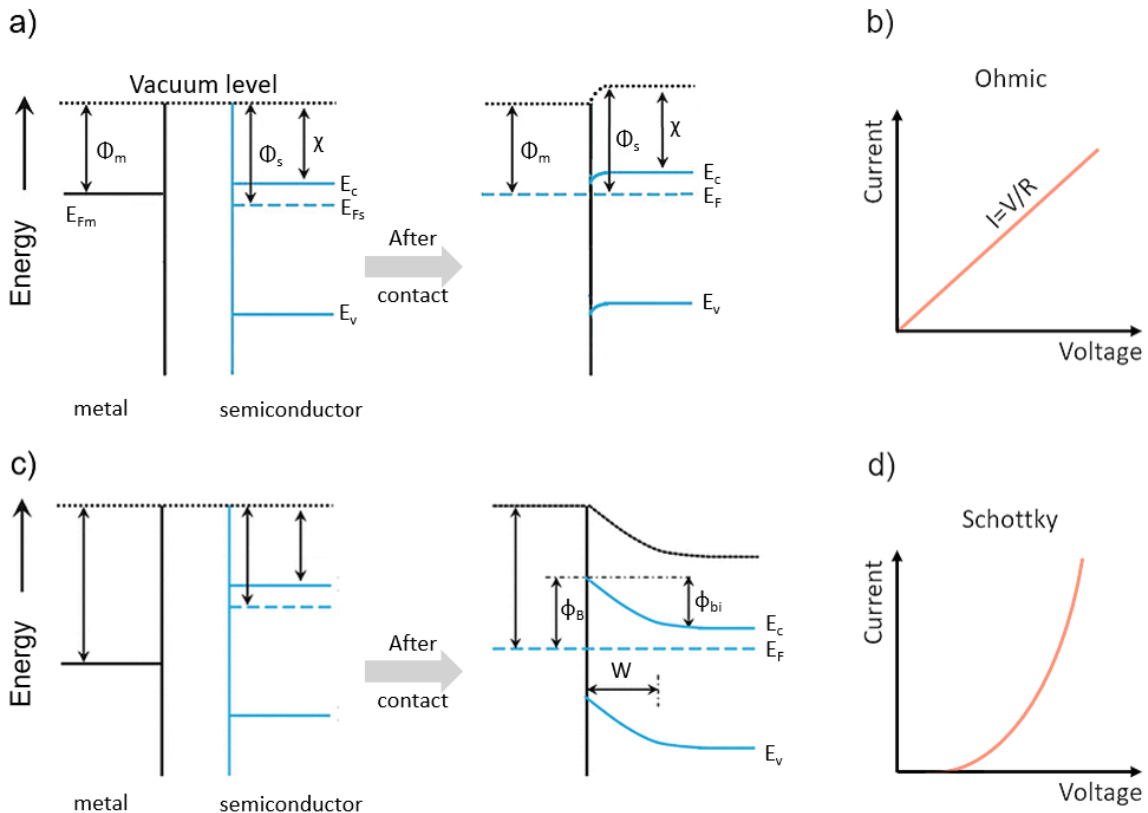


Figure 2-12. a) Band diagrams before and after contact of a metal and n-type semiconductor in an ohmic contact with b) a corresponding current-voltage characteristic. c) Band diagrams before and after contact of a metal and a n-type semiconductor in a Schottky contact with d) a corresponding current voltage characteristic. (a) and c) adapted from reference¹¹³⁾

In reality, thermionic emission may be insufficient in describing the current flow across the junction. This is due to the capability of electrons to tunnel through a thin barrier, with the probability of tunneling dictated by the Wentzel-Kramers-Brillouin (WKB) approximation:

$$T_{WKB} = \exp \left[-\frac{4\sqrt{2m_R^*}(E_g + E_\perp)^{\frac{3}{2}}}{3q\hbar F} \right] \quad \text{Eq. 2-9}$$

where m_R^* is the reduced effective mass, E_\perp is the transverse kinetic energy, \hbar is the reduced Planck constant, and F is the electric field through the junction ¹¹⁴. At very high carrier concentrations, the thinning of the barrier by Eq. 2-5 causes the SB width to be sufficiently thin, causing electrons to tunnel across the barrier through field emission, with minimal thermionic emission of electrons over the barrier (see Figure 2-13). In intermediate cases, a mixture of the two mechanisms, thermionic-field emission, is observed. In this case the SB is thin near the peak of the barrier such that the electrons must be thermionically energized but able to tunnel through the barrier below its peak height ⁴³.

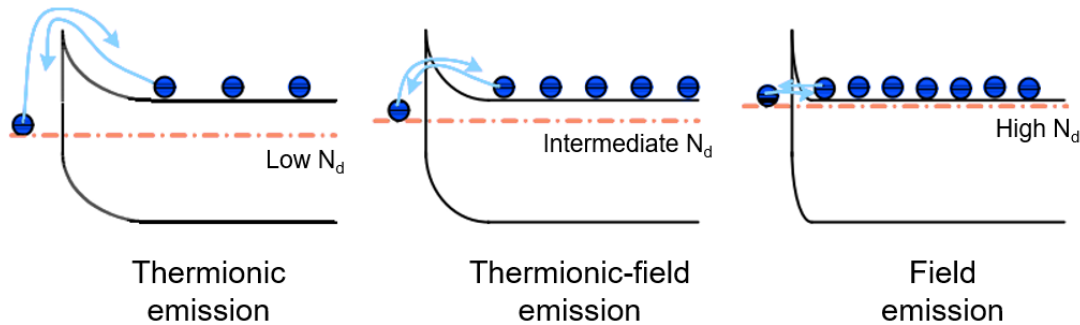


Figure 2-13. Schematic of the three transport mechanisms of charged carriers across a Schottky barrier based on the doping concentration and thus the Schottky barrier width (adapted from reference ⁴³).

While direct extraction of the SB height provides information on the junction properties, it is useful in many cases to combine the resistive effects of the SB and the resistance attributed to the contact area and material into a singular value of the contact resistance R_c . As this value takes into consideration the physical contact structure in addition to its electronic structure, it is a useful metric for quantifying device contacts as a whole. One method to quantify the contact resistance is a method known as the transfer length measurement (or the transmission line measurement,

abbreviated as TLM)¹¹². This method is best understood by modeling an electrically contacted component with an equivalent circuit system as a series of resistors illustrated in Figure 2-14a. The resistance of the functional channel material is defined as R_m , while the resistance associated with the contacts is defined as R_c . Note that R_c on both the source and drain is equivalent for a symmetrical device. When the channel length L is increased or decreased while keeping the remaining device parameters constant, R_m increases or decreases correspondingly. However, R_c remains constant, as it does not depend on the size of the channel itself. Furthermore, the change in R_m with L is linear due to Eq. 2-3. The total resistance across the series of resistors in this case can be described by the following equation:

$$R_T = R_m + 2R_c = \frac{\rho L}{A} + 2R_c \quad \text{Eq. 2-10}$$

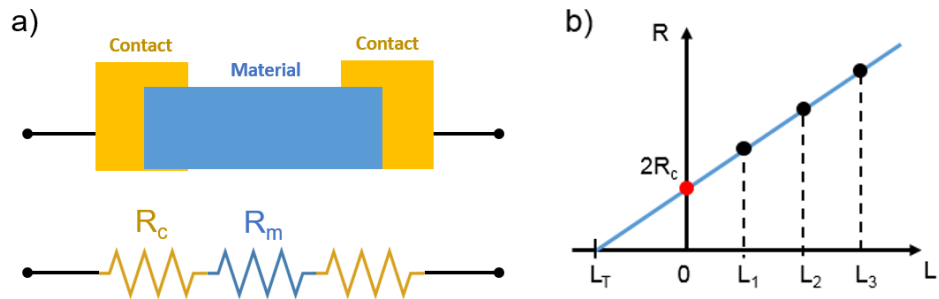


Figure 2-14. a) A channel with two electrical contacts and its equivalent circuit. b) A graphical representation of the relationship between channel length and the total device resistance.

Note that this relationship between R_T and L can be described by a linear curve with slope of $\frac{\rho}{A}$ and y-intercept of $2R_c$, as illustrated in Figure 2-14b. Physically, the y-intercept position describes a limit where L is infinitesimally small such that R_m approaches zero. Based on Eq. 2-10, $R_T \approx 2R_c$ at this point. A value for R_c can be extracted by plotting R_T as a function of L , then fitting a linear curve through the data and interpolating to the y-axis. In addition, this method can be used to obtain the sheet resistivity of the material from the slope of the fitted curve by combining Eqs 2-4 and 2-10:

$$R = \frac{R_s L}{W} + 2R_c \quad \text{Eq. 2-11}$$

where W is the width of the channel. Based on this, the slope of the fitted linear curve is equivalent to $\frac{R_s}{W}$, from which R_s can be calculated.

2-3-3. Transistors

A transistor is a variable resistor for which the utility is to dramatically increase or decrease the output current of the component to turn on or off an electrical signal. There are various types of transistors; for example, a phase-transition field effect transistor uses a metal-insulator-transition material such as VO_2 (shown in Figure 2-15) to amplify the effect of an in-line FET device by inducing an abrupt change in the injected drain current¹¹⁵. In this chapter, a basic introduction is provided for the most commercially produced transistor, the metal-oxide-semiconductor FET (MOSFET).

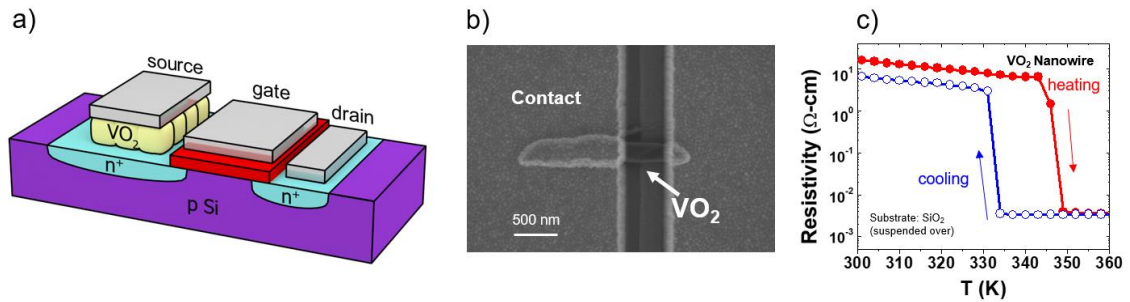


Figure 2-15. a) A schematic of a VO_2 phase-transition FET. b) A secondary electron microscope image of a VO_2 nanowire contacted on both ends, and c) representative resistivity transition driven in the material by heating (D. Deng, unpublished).

Before studying the characteristics of a MOSFET, it is useful to focus on one part of the device to study the switching mechanism. Figure 2-16a shows the band diagram of a metal-oxide-semiconductor stack, most commonly known as a metal-oxide-semiconductor capacitor (MOS capacitor) in a theoretical case where the work function is equal in the metal and the semiconductor.

When a gate bias $V_G < 0$ is applied to the metal, an electric field is induced in the oxide (also referred to as the gate dielectric) such that the majority carriers are accumulated at the semiconductor surface (in this case, the semiconductor is p-type)¹¹⁶. On the other hand, if a small $V_G > 0$ is applied to the metal, dipoles of the opposite polarity are induced in the oxide, inducing an inversion layer where the minority carriers accumulate at the material surface. For larger $V_G > 0$, strong inversion is induced in the film such that conduction at the surface of the semiconductor is dominated by the minority carrier. The nomenclature for the MOSFET is dictated by this region, such that the device in this example would be an “n-channel” device. The voltage at which strong inversion begins to occur, and thus the device begins to turn “on”, is defined as the threshold voltage V_T . The charge Q induced in the channel is related to the MOS capacitor geometry, V_G , and V_T through the following equation:

$$Q = \frac{\epsilon_{ox}}{t_{ox}} WL(V_G - V_T) \quad \text{Eq. 2-12}$$

where ϵ_{ox} and t_{ox} is the oxide permittivity and thickness respectively.

If electrical contact is made to the semiconductor in the MOS capacitor as illustrated in Figure 2-16d, the device functions as a full MOSFET with input control over the drain voltage V_D through the semiconductor channel and metal gate bias V_G . Figure 2-16e is an example plot of I_D as a function of V_D at varying gate voltages for an example n-channel MOSFET. At small V_D under constant V_G , the increase in V_D is met with a linear increase in I_D , proportional to the device conductance g ³:

$$I_D = gV_D = \left[\mu \frac{\epsilon_{ox} W}{t_{ox} L} (V_{GS} - V_T) \right] V_D \quad \text{Eq. 2-13}$$

While V_D and V_G has been assumed to independently control the device output thus far, this assumption breaks down with large applied V_D . In reality, V_D and V_G are compounded in the channel such that the voltage drop across the channel varies depending on the proximity to the drain contact to which V_D is applied. The source side of the channel sees a voltage drop between the gate and the

source equivalent to V_G . However, the drain side sees a smaller voltage drop of $V_G - V_D$. While this reduction in the effective gate bias is negligible for $V_G \gg V_D$, a decrease in the inversion of the channel near the drain contact is observed at larger V_D , manifesting in a decrease in the rate of I_D increase with V_D . When $V_D \cong V_G - V_T$, the inversion channel is “pinched-off” at the drain contact, signifying the loss of strong inversion, and the channel becomes independent of V_D :

$$I_{Dsat} = \frac{1}{2} \mu \frac{\epsilon_{ox}}{t_{ox}} \frac{W}{L} (V_G - V_T)^2 \quad \text{Eq. 2-14}$$

Because of current stability, this saturation region is where a MOSFET is operated for its “ON” state. In operating a MOSFET, the V_D is kept constant and V_G is used to modulate the channel and control the electrical output I_D .

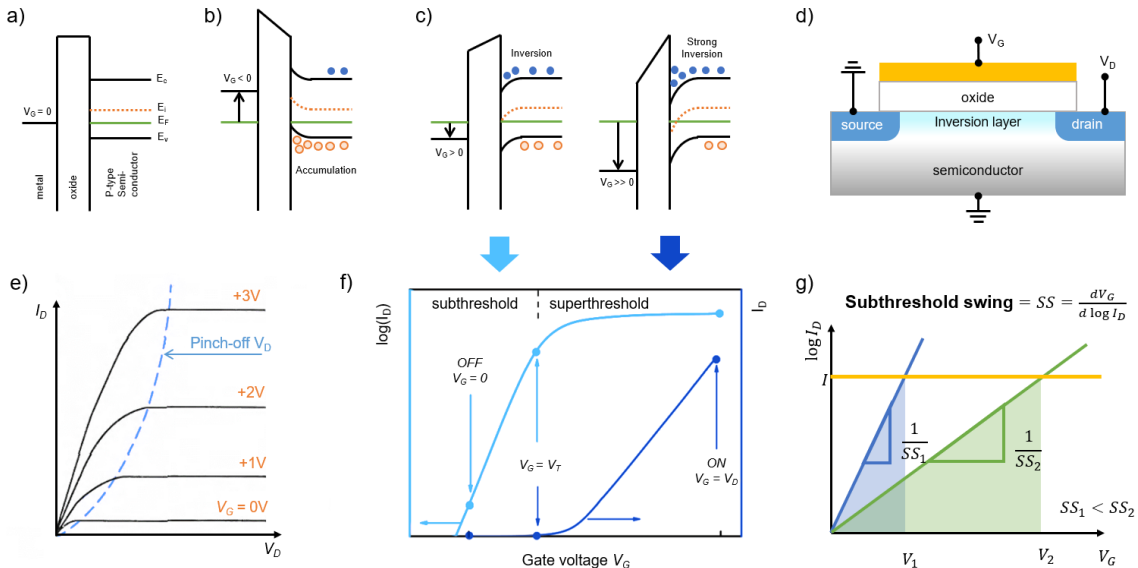


Figure 2-16. a) Band alignment schematic of a MOSCap with a p-type semiconductor. b) Band diagram of the MOSCap under $V_G < 0$. Majority carriers (holes in this case) accumulate near the semiconductor surface. c) Band diagrams of the MOSCap under a gate bias $V_G > 0$. Inversion of the carrier type at the semiconductor interface begins to occur at small magnitudes of V_G . As V_G is increased, the inversion increases and minority carriers accumulate at the semiconductor surface. d) A cross-sectional schematic of a MOSFET, illustrating the MOSCap and the inversion layer induced in the semiconductor channel. e) Example I_D - V_D curves over a range of V_G in log and linear scale. (adapted from reference ³) f) Example I_D - V_G curves in linear and log scale. (adapted from reference ¹⁶) g) A simple schematic illustrating the subthreshold swing in I_D - V_G curves.

While in an ideal transistor, $I_D = 0$ when $V_G < V_T$, this is not the case for a MOSFET, as a weak inversion layer is still present in the subthreshold region. A finite subthreshold current through the device is observed before the device is switched off with further decrease in V_G . The approximate difference in I_D in the off state and the superthreshold state is called the on/off ratio. The steepness of the subthreshold between the “ON” and “OFF” states describes how quickly the transistor can turn on or off, and is quantified as the subthreshold swing SS . SS is given as the inverse of the slope in log scale, which physically describes the additional voltage required to increase I_D by an order of magnitude. It is commonly given in units of mV/decade. This is a metric quantifying the efficiency of the MOSFET as a switch, as the power required to turn on a device, equivalent to the area under the transfer curve as illustrated in Figure 2-16g, is smaller for a steeper slope. In addition to dampening effect of the switch due to the weak inversion region, there also exists an intrinsic limit in the steepness of the subthreshold swing. Due to the Fermi-Dirac distribution of electrons filling energy states in the conduction band, an increase in gate voltage leads to a gradual increase in the current as electrons overcome contact barriers through thermionic emission¹¹⁷. At room temperature, the minimum SS is 60 mV/dec¹¹⁴.

2-3-4. Chemical vapor sensors

As discussed in the last section, a transistor controls the conductance of a circuit component to drive a change in the electrical output. Conversely, changes in the electrical output signifies a change in the environment of the device component. If the relationship between the component environment and its total resistance is understood, it is possible to produce sensors that monitor the electrical output of the device and attribute it to the device environment. There are various environmental changes that can be detected by a resistive sensor; for example, a photodetector converts a change in the number of photons to which it is exposed into a change in the magnitude of I_D ⁴⁹. The substance the sensor detects (i.e. the photons in the last example) is referred to as the

analyte¹¹⁸. There are many types of sensors relying on various sensing mechanisms depending on the analyte, the channel material, and how these interact. Resistive sensors rely on mechanisms that increase or decrease the carrier concentration in the functional material. Among these, sensors that rely on changes in its carrier concentration through charge transfer interaction with chemical vapors is referred to as a chemical gas sensor or as a chemiresistor¹¹⁹.

When discussing chemical species for charge transfer, it is useful to use the Lewis spectrum of acidity and basicity. This is a system that measures the relative propensity of a molecule to accept or donate an electron based on the electronegativity of the molecule and its atomic constituents. A Lewis acid is a substance that tends to accept non-bonding electrons, i.e. an electron-acceptor, while a Lewis base tends to be electron-donating¹²⁰. Figure 2-17a shows a spectrum of Lewis acidity of some example molecules. As a guide, molecules with lone pairs, such as ammonia (on the nitrogen atom) or triethylamine (TEA), tend to donate electrons, while molecules with atoms bonded to heavily electronegative atoms (such as F or Cl) tend to accept electrons.

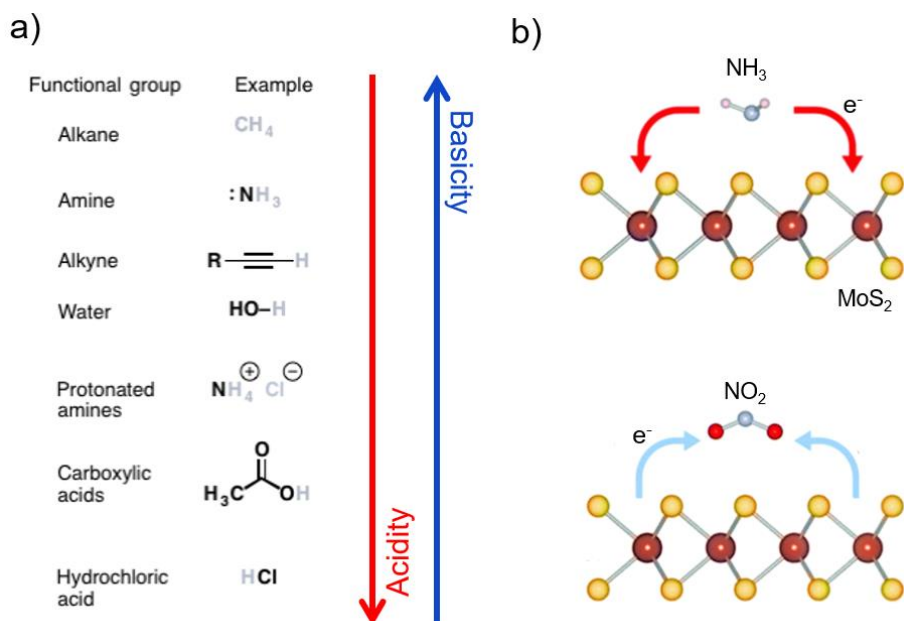


Figure 2-17. a) A scale of the relative acidity and basicity with examples of some functional groups (adapted from reference¹²¹). b) A schematic showing the direction of charge transfer between MoS_2 and NH_3 or NO_2 , which are Lewis base and acid respectively (adapted from reference¹²²).

The relative acidity or basicity determines the interaction with the sensing material. Example interactions are illustrated in Figure 2-17b. When a material interacts with a Lewis base, an electron donator, it gains electrons (loses holes through recombination), and the opposite is true for interactions with a Lewis acid. Depending on the major carrier type of the material, its resistance can increase or decrease relative to its unexposed state. This change is reflected in the electronic output, and is often reported in various ways; while some data are quantified in simple output values such as voltage or current, it is also common to use normalized values such as exposed “gas” resistance R_g over initial “air” resistance R_a , or R_g/R_a ^{123,124}. In the field of carbon nanotube or 2D material sensors, it is more common to define the sensor sensitivity S , as a % change in total resistance ΔR normalized to the initial resistance R_0 , or change in total conductance ΔG normalized to the initial conductance G_0 ^{125–128}:

$$S = \frac{\Delta R}{R_0} * 100\%$$

$$\text{Or } S = \frac{\Delta G}{G_0} * 100\% \quad \text{Eq. 2-15}$$

$$= \frac{\Delta I}{I_0} * 100\%$$

In systems with constant input voltage, the signal can be calculated as a normalized change in the output current I of the device as well. Conventionally, the signal is quantified in the direction of increasing signal; for example, since an increase in photons leads to an increase in the conductivity of a photodetector, this signal may be defined as $\Delta G/G_0$ rather than $\Delta R/R_0$. This is because a signal in the negative direction approaches a maximum normalized value of -100%, while an increasing signal has no mathematical upper bound, making it a more intuitive measure of the change in the environment of the material.

Due to the transient nature of surface chemical interactions, plotting sensor signals against time is useful in studying the interaction of the analyte and sensor material. Figure 2-18a is an

example of a resistive sensor signal as a function of time with varying exposure concentrations $[x]$ of some analyte x . Analyte released into the device environment interacts with the functional material to induce a sensor signal. When the system reaches steady-state such that the flux J of the analyte onto the sensor surface is equivalent to the flux off of the sensor surface as illustrated in Figure 2-18b, the device reaches saturation, corresponding to a plateau in the signal amplitude. A larger $[x]$ manifests in a larger saturation signal, due to increasing density of chemical molecules available for detection by the channel in equilibrium.

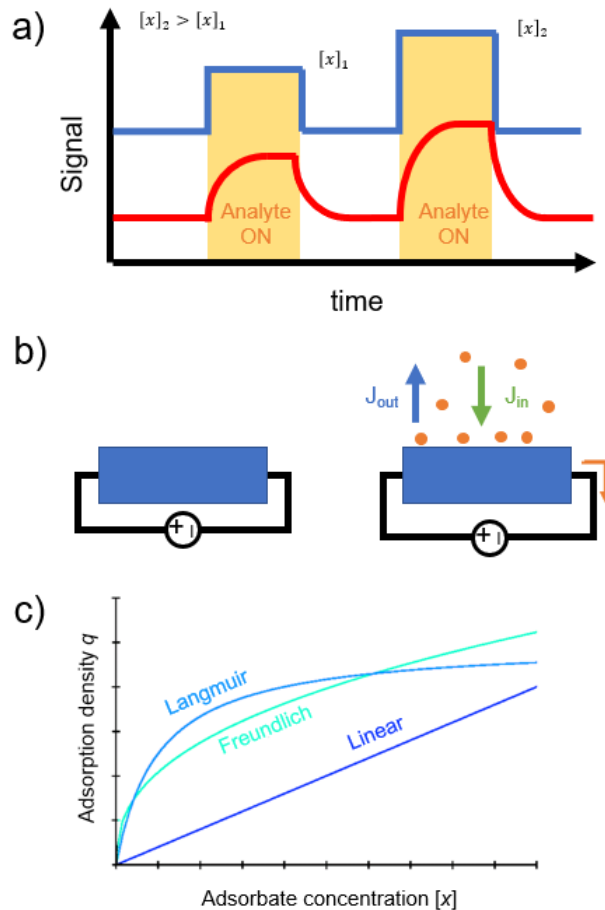


Figure 2-18. a) A simplified example plot of sensing signal over time in an ideal device (blue) and realistic device (red) for two analyte pulses at varying concentrations. The yellow highlighted regions correspond to when the sensor is exposed to analyte. b) A simple schematic of a sensor before exposure and at steady-state during exposure, showing the equilibrium of flux onto and off of the substrate at steady-state. c) The adsorption density q as a function of the concentration for Langmuir and Freundlich models, in comparison to a linear model (adapted from reference ¹²⁹).

The exact relationship between $[x]$ and S will vary depending on the nature of the adsorption interaction between the analyte and the material. There are many adsorption isotherms that model the relationship between the amount of analyte on a material surface and the concentration of that analyte in the surrounding liquid or gas mixture^{130,131}. The two most commonly used models are Langmuir and Freundlich isotherm models. The Langmuir model is based on a rational model of analytes adsorbing onto a finite number of sites (i.e. defects), such that the fractional occupancy θ of these sites is given by:

$$\theta = \frac{K_L[x]}{1 + K_L[x]} \quad \text{Eq. 2-16}$$

where K_L is the Langmuir constant. This model assumes that only a monolayer of analytes can adsorb on a finite number of sites. This leads to upper limit of θ at 100% above large concentrations. The Freundlich isotherm model is an empirical model without a logical derivation. The adsorption density q_e on the material surface is given by a power relationship:

$$q_e = K_F[x]^{\frac{1}{n}} \quad \text{Eq. 2-17}$$

where K_F and n are empirical fitting values dependent on the system. While the Freundlich model does not stem from a logical derivation, it is useful for describing the relationship between adsorbed analyte and concentration under systems where the assumptions of the Langmuir model fails. The adsorption density curves modeled by each method is illustrated in Figure 2-18c.

While the isotherm models aim to describe the relationship between $[x]$ and the sensor signal, the models describe a system in equilibrium after the sensor system has saturated. The blue curve in Figure 2-18a indicates a theoretical, non-kinetic limited case where all analyte interactions with the material occur immediately such that the signal steps to saturation. However, the red curve is more representative of experimental data, where the sensor has a finite duration of time where the signal increases until it reaches saturation. This duration of a sensor “turning on” is referred to as the response time τ_s , while the opposite “turning off” time is referred to as the recovery time τ_r .

It is also common for both time factors to be represented simply by τ in their own respective context. While minimization of the duration of the response and recover transitory states are ideal, a τ_s of less than 1 minute is generally considered fast sensing¹¹⁸.

In literature, the response and recovery time is often defined in two methods. The first method is to define τ_s as the time it takes for the signal to reach a specific value, usually 90%, of its saturation value^{132,133}. The same method can be used to obtain τ_r as the time it takes for the single to fall to 10% of the saturation value. This is a simplistic approach not limited to the sensing mechanism, making it a universally comparable time factor. The second method is associated more with a physical model of analyte interaction with the channel material, and is particularly useful for chemiresistors that rely on charge transfer from analytes adsorbed on the surface of the channel material. In this method, the system is approximated as having a finite amount of adsorption sites, and the occupancy of these sites and thus the signal of these sensors increases until equilibrium is reached, at which the signal saturates. The response signal of the sensor at time t after starting exposure can be approximated as an exponentially decaying increase^{134,135}:

$$S = y_0 + A \exp\left[-\frac{t}{\tau}\right] \quad \text{Eq. 2-18}$$

A is the saturation amplitude, y_0 is a fitting parameter, and τ is the response time factor. In systems where there is more than a single sensing mechanism (for example, if there are two types of defect sites with varying interaction rates that compound into the signal), the sensing signal may be more accurately described using multiple exponential curves. This second method of quantifying response time will be used for sensor discussions in this dissertation. Note that while τ is discussed as the speed at which the sensor turns on, it is difficult to deconvolute this data from other transient factors, such as the time required to deliver the analyte from an open valve.

While S is a normalized term describing a relative change in the output characteristic, the relative signal-to-noise ratio S/N of the sensing characteristics is also useful to note as a metric of the confidence of the signal data and thus the resolution of the device. In this case, the signal is the

saturation signal amplitude, while noise is calculated as the root-mean-squared value of output signals taken in the “off” state. The detection limit of a sensor is often defined as the concentration at which a signal to noise ratio of 3 is achieved ¹³⁶.

2-4. Basics of device fabrication

There are two main ways to approach device fabrication for 2D materials, generally corresponding to small area placement or large area growth. When working with top-down approaches to material integration, such as exfoliation or deterministic transfer, the electronic device is built around the material based on the location of the target material ^{19,40,64,65}. Conversely, when working with large area of films achievable through MOCVD or PV techniques discussed in Section 2-2, it is possible to fabricate large arrays of devices without the need to map the material ^{70,137}. While the material, substrate, and design preparation may vary between the two methods, device fabrication techniques are universal. An example of a series of processing steps for devices is illustrated in Figure 2-19. After growth, the material is isolated into device dimensions. This is done in order to isolate each device in the array and contain carrier flow in specified regions. For 2D materials, which have reduced adhesion to 3D materials ^{138,139}, removing material where it is unnecessary also serves to create areas where metal can be anchored down to the substrate. After isolation, contacts are deposited. The contact metal is either a single material, such as Ni, or a double layer, such as Ti/Au, where the Ti layer acts as an adhesion layer between the 2D material and the gold. Depending on the targeted electrical characterization techniques, a second deposition of thicker metal where probes can sink into away from the actual device channel may be necessary. The following sections offer background information and discussions on current challenges on fabrication processes for 2D material-based devices.

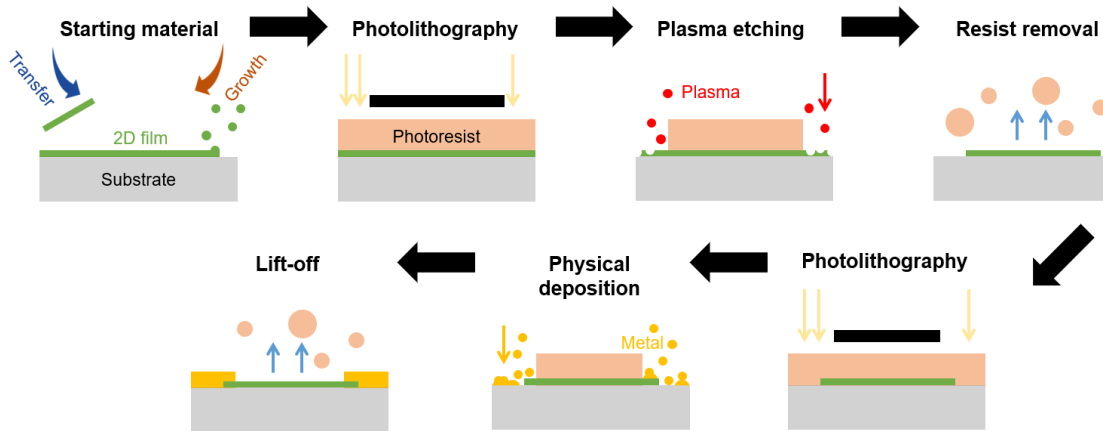


Figure 2-19. A schematic of the basic fabrication steps required to fabricate a simple two-terminal device. Material is transferred or grown on a film, then lithographically patterned for isolation etching. After cleaning, the patterning is repeated for the deposition of contact metals. Depending on the complexity of the device, other processes or repetitions may be used. However, the devices in this dissertation work is limited to 2 or 3 patterning processes after growth in order to minimize resist residue.

2-4-1. Lithography

Lithography is the process of transferring a pre-designed pattern onto the device substrate¹⁴⁰. The simplest lithography process is the use of shadow masks. These are physical stencils that can be placed on top of the sample, with exposed areas for subsequent etching or deposition techniques. While it is possible for any solid material to act as a stencil, commercial shadow masks are often made on metal films whose thickness is dependent on the required resolution of the mask. This method is fast and minimizes direct contact of polymer resists and chemicals to the material surface which may affect the subsequent device characteristics. However, the resolution is limited by the process of creating openings in the shadow mask, such as milling or laser cutting, and is generally on the order of 10 µm¹⁴¹⁻¹⁴³. Furthermore, alignment of the shadow mask is generally done by hand with minimal precision.

When improved resolution or alignment is targeted, polymer resist-based photolithography is necessary. In this method, an energy sensitive photoresist is deposited and cured on the sample,

after which the design is exposed into the polymer through energization with photons (optical lithography or X-ray lithography), or electrons (electron-beam lithography, also known as EBL). In projection optical lithography, the method mainly used in this dissertation, the resolution limit is governed by Raleigh's equation, approximated to the wavelength of the exposure light¹⁴⁴. Electrons, having lower de Broglie wavelengths than photons, can be used to achieve much lower resolutions, down to few nanometers, limited by spatial aberration¹⁴⁵. After the photoresist is energized, the sample is soaked in developers that dissolve and remove polymer in regions where the pattern is exposed, for positive photoresist, or in regions where the pattern is not exposed, for negative photoresist³. This results in a sample with polymer-protected regions and exposed regions in a specified pattern for subsequent steps. Depending on the subsequent processing step, multiple layers of photoresist may be necessary; this is discussed in Section 3-1.

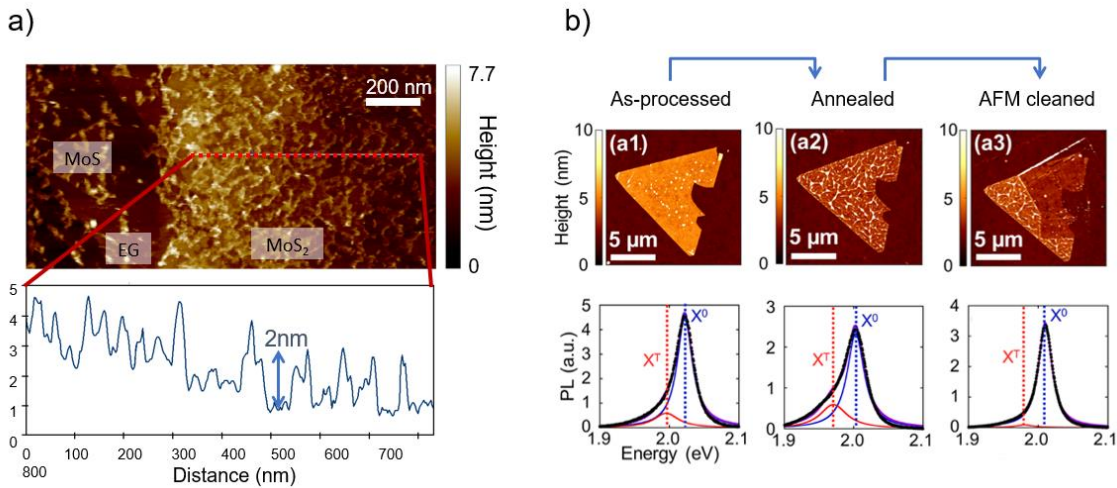


Figure 2-20. a) AFM image of the surface of a MoS_2 device after several photoresist lithography processes and a simple cleaning step. (D. Deng, unpublished) b) A comparison of the PL of WS_2 before any cleaning, after an anneal in H_2/N_2 , and after an AFM “nano-squeegee” cleaning process, where the polymer residue is physically scraped away. The disappearance of the trion peak suggests the AFM method is effective, and the PMMA residue on the surface directly affects the electrical properties of the WS_2 (adapted from reference¹⁴⁶).

Though photoresist is removed after processing using polymer stripping chemicals, it is difficult to fully clear the surface of 2D materials after contact with photoresist. For example, Figure 2-20a shows an atomic force microscope (AFM) image of MoS_2 surface after two photoresist

patterning steps have been performed. While surface cleanliness is a challenge in fabrication of devices with any material, it is especially detrimental to 2D materials where their large surface-to-volume ratio make material characteristics sensitive to surface contamination^{147,148}. Rosenberger et al. observed that cleaning a WS₂ monolayer with an AFM tip in contact mode lead to a significant decrease in the trion peak, shown in Figure 2-20b, suggesting the surface contaminants may be doping the underlying material through charge transfer doping¹⁴⁶. While there are many cleaning methods proposed for residue removal, such as thermal annealing, it has remained difficult to completely remove polymer residue without damaging the underlying 2D material¹⁴⁹.

2-4-2. Plasma etching

After transferring a pattern onto a sample using photoresist, the sample can undergo two main types of fabrication steps: Etching and deposition. In etching processes, material is removed from the growth substrate through wet chemical, plasma, or bombardment techniques. This dissertation work uses plasma etching as the main material removal process.

During plasma etch, gas atoms energized into a plasma are accelerated towards the target sample to physically or chemically remove material¹⁵⁰. First, a controlled mixture of gasses is introduced into a reactive chamber. The gasses are then discharged into plasma by applying a voltage across the plasma sheath region in the chamber, from the source to the substrate platform (see Figure 2-21a). The etch is heavily dependent on many plasma parameters, including the substrate bias, temperature, and pressure¹⁵¹. Controlling the gas composition is also necessary to tune the etching mechanism from chemical reaction to physical bombardment. By optimizing these parameters, the etch can be controlled to be gentle for surface cleaning or strong for deep material removal. For example, O₂ plasma can be used as the main gas in both the cleaning of graphene surfaces and in etching layers of graphene. It has been reported that utilizing a short plasma etch of O₂/He at 150/50sccm lit with RF power of 100W to clean graphene surfaces prior to the metal

deposition process can improve the subsequent device contact resistance by up to three orders of magnitude, as plotted in Figure 2-21b¹⁵². The graphene begins to appear defective with increasing plasma exposure time, and O₂ based etches are often used to etch graphene for device isolation^{153,154}. MoS₂ can be etched using various gasses including CH₄, XeF₂, and SF₆. While exact etch recipes must be optimized per system, adjusting etch parameters can tune SF₆ based plasma from aggressive to gentle, and even precise single layer etching has been reported^{155–157}.

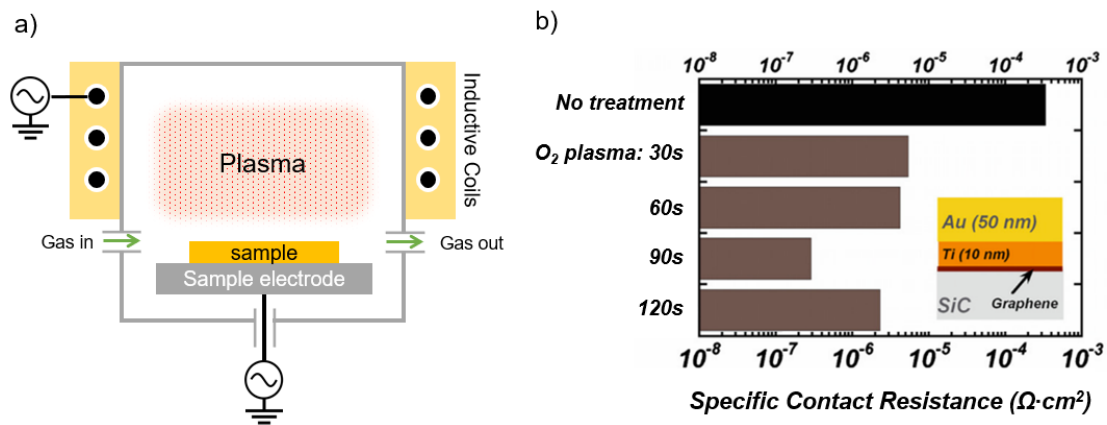


Figure 2-21. a) A schematic of an inductively coupled plasma etch chamber, based on the system most frequently used in this dissertation. The sample is placed on a bias electrode towards which the charged particles in the plasma is accelerated. b) A comparison of contact resistance of Ti/Au on epitaxial graphene for various duration of plasma treatment. 90s O₂ plasma before the metal deposition reduces the contact resistance by three orders of magnitude (adapted from reference¹⁵²).

2-4-3. Physical vapor deposition

Physical vapor deposition methods are commonly utilized to add material onto a patterned sample. In these methods, the deposition material is vaporized through various means, such as thermal heating or sputtering, and transported through a vacuum, low pressure gas, or low pressure plasma environment towards the target substrate¹⁵⁸. In this dissertation, the main method utilized is electron-beam evaporated deposition, where the heating of the source material is done using an electron beam, as illustrated in Figure 2-22a. The deposition rate is controlled by the power of the

electron beam. In depositing metal patterns, it is important to recognize that the metal atoms are evaporated from a point source for many deposition processes, such that the deposition profile is not entirely vertical onto the sample. Instead, the direction at which the atoms approach the surface varies as a function of location on the target substrate¹⁵⁹. While the effect of this directional fanning is reduced as a function of distance of the source and the target substrate, this is limited by the dimensions of the deposition chamber. This becomes a detrimental problem in metal pattern deposition, where metal can be deposited on the sidewalls of the photoresist, as illustrated in Figure 2-22b. After the photoresist and excess metal is cleaned off, a process called “lift off”, the metal on the sidewalls of the photoresist can collapse onto the sample, or the metal can fail to lift off entirely if the sidewall is connected to the metal on top of the photoresist. In order to prevent this, metal patterning is often done with a photoresist double stack layer where the underlying layer has a wider opening than the top layer. This prevents the deposited metal in the pattern to be completely separated from the extra metal on top for more accurate metal patterns¹⁶⁰.

Based on the semiconductor-metal junction physics discussed in Section 2-3-2, the work function of the metal in contact with the 2D material should play a large role in determining the contact transport characteristics. Das et al. showed that using lower work function metals such as scandium in contact to MoS₂ led to improved FET device characteristics, as shown in Figure 2-22c⁶². However, many other reports show that there is minimal correlation between the work function and the contact quality, suggesting that the fermi level is pinned such that it always lies in a range near the conduction band within the MoS₂ bandgap^{152,161}. This discrepancy may further suggest the large role processing steps play in the device characteristics of a 2D TMD-based device.

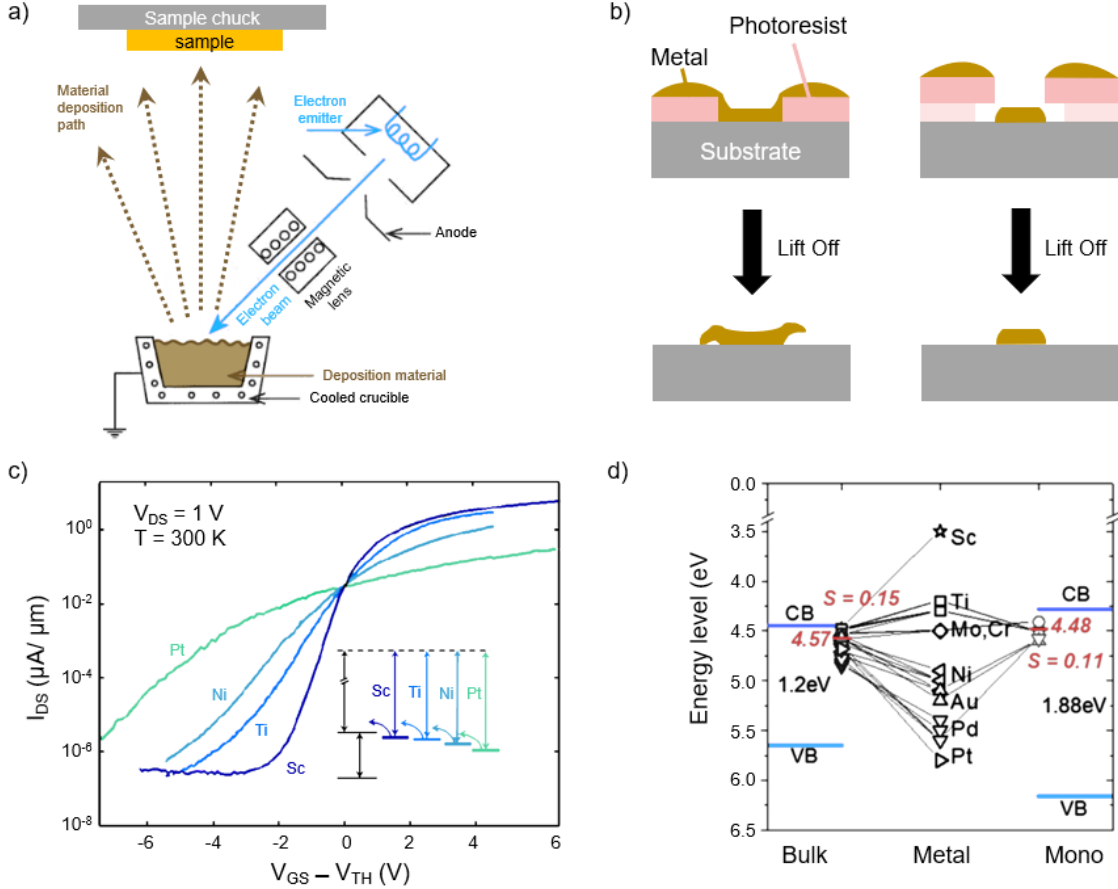


Figure 2-22. a) A schematic of a physical vapor evaporation system. In this thesis, an electron beam is utilized to vaporize the material (adapted from reference ¹⁵⁸). b) A cross-sectional illustration of a single layer and double layer photoresist stack for metal patterning. Using a single stack can lead to sidewall deposition that can collapse after resist removal or lead to lift-off failure. c) Device transfer characteristics measured for devices using various metals as contacts to MoS_2 . There is a correlative trend between the proximity of the metal work function to the MoS_2 conduction band and the device performance (adapted from reference ⁶²). d) A map of the metal work function and the energy level at which various metals are pinned to for both bulk and monolayer devices is plotted. The metal work function appears to have minimal effect on the location at which the metal pins to the semiconductor (adapted from reference ¹⁶¹).

2-4-4. Gate dielectric

The MOS capacitor was discussed in Section 2-3-3, where the gate dielectric was introduced as the barrier between the gate metal and semiconductor. The gate dielectric is an integral part of a MOSFET, as it controls the electronic properties of the channel. One of the reasons

for Si's dominance in MOSFETs is due to the facile and well-understood integration of SiO_2 as its gate dielectric¹⁶². SiO_2 was later replaced by high-k dielectrics when the MOSFET was scaled down to the 45 nm node in order to minimize gate leakage and improve device performance⁸. The most commonly used gate dielectric materials now are HfO_2 and Al_2O_3 , though others such as ZrO_2 have also proved useful^{163–166}.

The deposition of high-k dielectrics on top of 3D semiconductor channels has been well studied, and the most common method is through atomic layer deposition (ALD). This method relies on a cycle of self-limiting reactions where individual precursors are introduced into the chamber, depositing a monolayer of material, then purged before the next precursor is introduced¹⁶⁷. A schematic of the process for an oxide, specifically Al_2O_3 , is illustrated in Figure 2-23. An incoming precursor (Tri-methyl aluminum or TMA in this case) reacts with a hydroxyl group (-OH) until all -OH bonds are filled; once the excess precursor is purged, H_2O is introduced into the system and reacts with the Al components on the substrate surface, leaving it with -OH bonds at the surface such that the cycle can be repeated again¹⁶⁸. The initial -OH bonds on the substrate surface can be created with a series of pre-ALD water-pulses.

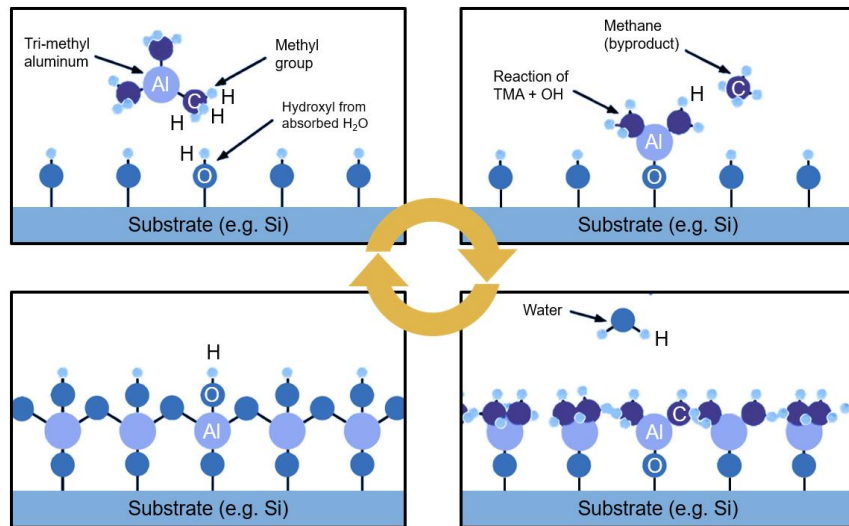


Figure 2-23. An illustration of the self-limiting cycles of ALD growth for Al_2O_3 , showing the self-limiting cycles of TMA and H_2O reactions on the sample surface (adapted from reference¹⁶⁹).

The initial ALD steps are heavily dependent on the surface of the semiconductor; this makes the process difficult for TMD materials, which do not have dangling bonds at the surface to which the first precursor can bond. Some success with ALD on TMDs have been reported, many by utilizing tricks such as pre-ALD seed layers or surface treatments^{170–172}. However, translating and reproducing ALD growths to different ALD systems requires considerable optimization due to the sensitivity of the technique on TMDs. Figure 2-24a illustrates some of the ALD growth processes attempted at Penn State for Al_2O_3 growth on WSe_2 , where it was observed utilizing an oxide seed lowered the dielectric film roughness in comparison to metal seeds. Using an Al_2O_3 seed prior to ALD on MoS_2 yielded a fully covered, conformal Al_2O_3 film, but proved to be low quality as a gate dielectric for a FET, with a high leakage current of $3\text{mA}/\mu\text{m}$ and poor electrostatic control with 2 orders of current increase over 20 V of V_G .

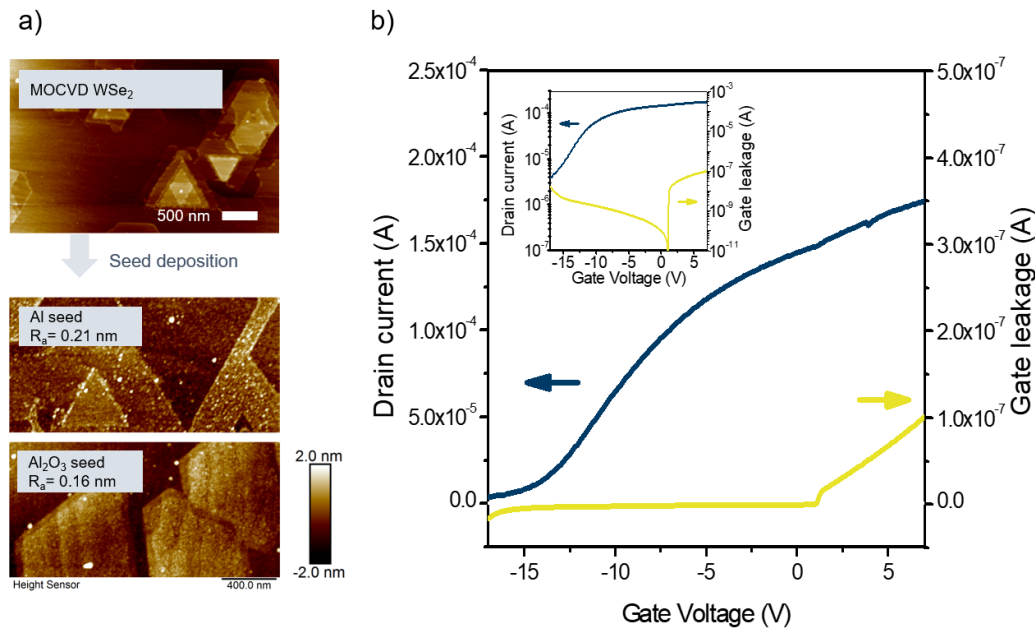


Figure 2-24. a) Atomic force microscope (AFM) images of MOCVD WSe_2 with 2 nm of seed layer and 20 nm of ALD. Using Al_2O_3 seeds lead to lower roughness of the subsequent ALD film. b) Drain current and gate leakage current as a function of gate bias for a $33\mu\text{m}$ wide MoS_2 channel with 2 nm Al_2O_3 seed and 20 nm ALD Al_2O_3 . The inset shows the data on a log scale (D. Deng, unpublished).

Due to the difficulties of ALD deposition of high-k dielectrics on TMDs, other gating methods have been used to characterize 2D material-based devices. A simple method is to utilize a back gate, where the gate dielectric is under the channel material^{40,64}. SiO₂ on doped Si is a common back gate stack due to its commercial availability. However, this requires transferring the 2D material from a growth substrate, making it unscalable, or directly growing on a substrate with a back gate, which can be difficult as direct growth methods are heavily affected by the substrate material. Another option is to utilize gates that can be drop cast onto the sample in liquid from, such as liquid ion gating or solid electrolyte gating. In these gating methods, an electric field induced in the medium by the gate electrode drives diffusion and accumulation of charged ions on the surface of the material, leading to electrostatic doping of the channel^{173–175}. Despite the relatively slow measurement rates required to operate the device in equilibrium due to ion motion through the medium, this method is compatible with TMDs and has been shown to be able to induce large carrier density changes in the channel material.

2-5. Summary

In this chapter, an overview of several topics necessary for the discussion of subsequent experiments and results in this dissertation was provided. A background in semiconductors and 2D TMDs was discussed, followed by an overview of various growth or material transfer methods in literature and in this dissertation work. In addition to a materials background, the basic physics of resistors and metal-semiconductor junctions was discussed, followed by the theoretical concepts and metrics for FETs and chemical vapor sensors. A series of sections also provided an overview of the fabrication methods utilized in this thesis, including the current challenges in each of these steps for 2D materials. The information presented in this chapter will help facilitate the discussions on experimental results for the remainder of this thesis.

Chapter 3

Experimental Procedures

While an overview of growths and device fabrication methods was given in Chapter 2, Chapter 3 lists the exact methods and techniques used in this dissertation work. While the main process flow follows the example schematic shown in Figure 3-1, the exact order is detailed in the Materials and Methods Section within each following chapter. Chapter specific process or characterization parameters are also listed in these sections.

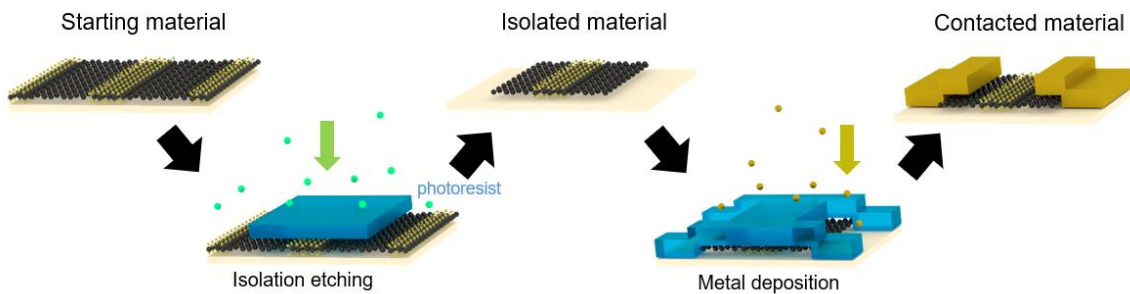


Figure 3-1. A schematic of the basic fabrication steps required to place contacts on a heterostructure material after growth. First, the material is grown on a substrate using one of the methods discussed in Section 3-3. After growth, a photoresist patterning is performed for isolation etching, discussed in Section 3-4-2. The photoresist is removed using the standard cleaning procedure listed in Section 3-1-3. After cleaning, another photoresist patterning is performed, this time for the deposition of contact metals, discussed in Section 3-3-3. Depending on the complexity of the device, other processes or repetitions of earlier fabrication steps may be necessary.

3-1. Lithography on 2-dimensional materials

To pattern TMD films, optical lithography or electron-beam lithography (EBL) is used depending on the requirements for each subsequent processing step. Designs with minimum resolution of 1 μm or larger is exposed using optical lithography, while designs requiring smaller resolution or single-use designs (specifically for designs made for exfoliated flakes) is exposed using EBL. Nearly all patterning in this dissertation work is done using optical lithography, and the

photoresist preparation, exposure, and development is similar for most processes in the remainder of this chapter. Details that vary between each optical lithography process are compiled in Table 3-1 and in the Materials and Methods section in subsequent chapters.

3-1-1. Optical lithography

Before photoresist deposition, TMD films are baked on a hotplate at 110 °C for 1 minute to desorb excess water and organics adsorbed on the surface. The bottom PMGI photoresist layer is spin coated on the sample at 3000 to 4000 rpm in order achieve a uniform coating of photoresist. The speed and PMGI photoresist concentration, ranging from SF2 to SF11, is dictated by the target thickness required for the subsequent fabrication process (see Table 3-1). This layer is cured for 5 minutes at 190 °C. After the PMGI layer, the SPR 3012 is spun on the sample and cured for 1 minute at 95 °C. The patterns are exposed on the polymer using Stepper 8500 i-line optical lithography for a specified duration of time at a lamp power of 25 mW/cm. The 3012 layer is then developed in CD26 developer with agitation by lightly “swishing around” the developer dish by hand. This is followed by a rinse in DI water to remove developer residue. The underlying PMGI layer is then exposed using 1000 W 260 nm wavelength UV flood lamp for up to 900 seconds depending on the thickness of the photoresist. The sample is then developed in 101A developer with light agitation followed by a rinse in DI water.

3-1-2. Electron beam lithography

Unlike the various parameter variations for optical lithography, only one process for EBL was used. After sample dehydration bake identical to the optical lithography case, Zep520A photoresist is spun on the sample at 4000 rpm. The film is cured for 3 minutes at 180 °C on a hotplate. Prior to exposure in EBL, a thin, uniform 10nm coating of gold is deposited on the sample

using thermal physical deposition to prevent charging of the insulating sample that may distort the electron beam. The sample is exposed using Vistec® EBPG5200 Electron Beam Lithography system. Areas of the pattern with features resolution under 3 μm is written using a 65 nA electron beam with 300 μm aperture at 180 $\mu\text{m}/\text{cm}^2$, while portions with larger resolution features are written using 150 nA electron beam with 400 μm at 200 $\mu\text{C}/\text{cm}^2$. The exposed photoresist is developed in n-amyl acetate for 180 seconds, then 20 seconds in methyl isobutyl ketone (MIBK):IPA 8:1 followed by a brief rinse in IPA and N₂ drying.

Table 3-1. A table of the photoresist stack, exposure, and developing information used for the various fabrication processes. Parameters not listed in this table, such as soft bake temperature of developer type, is constant for all processes ^{176,177}.

<i>Fabrication step</i>		<i>Etched alignment marks</i>	<i>Graphene isolation etch</i>	<i>TMD isolation etch</i>	<i>Contact metal deposition</i>	<i>Pad metal deposition</i>
<i>Bottom photoresist layer</i>	Photoresist	PMGI SF11	PMGI SF2	PMGI SF2	PMGI SF5	PMGI SF11
	Spin speed	3000	4000	4000	3000	4000
	Thickness	1000 nm	50 nm	50 nm	175 nm	900nm
	Exposure	UV Flood 900s	UV flood 400s	UV flood 400s	UV flood 600s	UV flood 900s
	Develop time	45s	60s	60s	60s	90s

<i>Top photoresist layer</i>	Photoresist	SPR3012	SPR3012	SPR3012	SPR3012	SPR3012
	Spin speed	3000	4000	4000	4000	4000
	Thickness	1500 nm	1300 nm	1300 nm	1300 nm	1300 nm
	Exposure	Stepper 0.35s	Stepper 0.25s	Stepper 0.25s	Stepper 0.25s	Stepper 0.25s
	Develop time	60s	60s	60s	60s	90s

3-1-3. Photoresist removal

After photoresist patterning and subsequent processing steps, the polymer layers are removed from the sample surface by soaking in solvent. The samples are inserted in a holder in a vertical position such that any contaminants or layers removed from the surface in the cleaning

process do not redeposit on the sample surface. The sample holder and inserted samples are placed in Baker® Photoresist Strip 3000 (PRS 3000) heated to 80 °C for a minimum of 30 minutes. The sample is then placed in boiling acetone for 5 minutes followed by a rinse in room temperature isopropyl alcohol (IPA). Finally, the sample is dried using N₂.

3-2. Substrate preparation

3-2-1. Alignment marks

If the targeted devices are to be made directly on the growth substrate without transfer, alignment markers are first etched into the substrate before material growth. This is in order to avoid using metal alignment marks that may disintegrate during the growth process and deform or contaminate the growth, while minimizing the number of photoresist-based lithography steps on the 2D material after growth.

Silicon Carbide (SiC) Substrates

The sample surface is prepared by a short 60s dip in DisChem® Surface Passivator 3000, followed by a deionized (DI) water rinse. Due to the thick layer of photoresist necessary to withstand the aggressive substrate etching process, a thick stack of PMGI SF11 and SPR3012 for a total of 2.5 μm of resist is spin coated on the sample (details are shown in Table 3-1). The alignment pattern is transferred onto the photoresist using GCA Stepper 8000 or 8500 i-line optical lithography. After developing the SPR 3012 top layer, the sample is exposed to deep UV flood for 900s in order expose through the thick SF11 layer. The sample is then developed in 101A for 45s; due to the poor adhesion of PMGI to SiC, longer develop times result in the delamination of the PMGI layer from the substrate.

After patterning, the sample is exposed to a looping plasma etch in a Plasma-Therm® Versalock system using 20 mTorr 55 sccm sulfur hexafluoride (SF₆). The plasma is lit with 300 W RF power and an additional 800 W is applied to the substrate electrode. Each loop is 20 seconds long and separated by 3 sets of cleaning loops, comprised of 20s purging using 50 mTorr N₂ and 30s vacuum pumping. In addition, the etch is performed at 5 °C to maximize the SiC:photoresist etch rate ratio. The process utilizes 20 full loops with a total effective etch time of 400s, and etches approximately 400nm deep into the SiC substrate.

Sapphire Substrates

Sapphire samples are prepared in the same method as SiC above, with only a difference in the etch recipe. The substrate is etched using 3 mTorr 50 sccm boron trichloride (BCl₃). The etch is performed at 5 °C with a power of 150W and additional 800W applied to the substrate electrode. The etch is performed in loops of 60 seconds of etch followed by 3 sets of purge and pump, same as described for SiC etch above. The process utilizes 10 full loops for a total effective etch time of 600s, and etches approximately 400nm deep in to the sapphire substrate.

3-3. Material growth

3-3-1. Pre-growth cleaning

Immediately prior to growth, all samples, with or without alignment marks, are sonicated in acetone and IPA for several minutes each. After drying with N₂, the samples are cleaned in 80 °C heated Nanostrip® for at least 30 minutes. The sample is then rinsed three times in DI water to remove all trace of Nanostrip® and dried using N₂.

3-3-2. Powder vaporization growth

Powder Vaporization of WS₂

Single crystalline WS₂ flakes are grown on a Si substrate with 285 nm thermal oxide on the surface. Prior to growth, the sample is cleaned with heated piranha solution at 80 °C for 40 minutes. A seed layer of 2nm WO₃ is thermally evaporated on the sample. It is then loaded into a quartz reaction tube with 300 mg of 99.5% purity sulfur powder and then heated to 800 °C while the sulfur is separately heated to 250 °C. The growth yields isolated, triangular domains ranging from 1 – 6 µm in size. Characterization of these growths are shown in section 4-4-2.

Powder Vaporization of MoS₂

For the dielectrophoretic studies, the MoS₂ is grown on Si with 300 nm of thermal SiO₂. After cleaning, the substrate is loaded into a quartz growth tube with 200 mg of 99.9995% purity sulfur powder 27 cm upstream from the substrate, heated to 200 °C. MoO₃ powder is placed 7 mm upstream from the growth substrate under the sample. The growth is performed at 745 °C for 15 minutes at near-ambient pressure (710 Torr) with 300 sccm of Ar carrier gas. Unlike the WS₂, the monolayer MoS₂ crystals using this method is hexagonal shaped, and the domains range from 2 µm to 10 µm in size. A schematic of the growth system is illustrated in Figure 2-8a, and characterization of these growths are shown in section 4-4-3.

3-3-3. Epitaxial graphene-powder vaporization MoS₂ Growth

Epitaxial graphene growth

A 1cm x 1cm 6H crystalline SiC substrate is placed in a hot-zone graphite furnace illustrated in Figure 2-10a, where it is heated to 1500 °C in 10% H₂ for 30 minutes to remove any subsurface damage. For graphene growth, the system is heated to 1800 °C in 100% Ar atmosphere

at 500 Torr. A growth time of 10 minutes produces 2~3 layered EG on top of the buffer layer, as illustrated in Figure 2-10c.

Graphene isolation

After growth, the EG is patterned into rectangular shapes. A thin stack of PMGI SF2 is used underneath the SPR 3012 layer to facilitate the cleaning process after etch. After lithography, the graphene is etched using 5/30 sccm O₂/Ar₂ plasma for 45 seconds in a Plasma-Therm® Versalock 700 system. In this process, the top surface of the photoresist is cross-linked and becomes difficult to remove using the standard cleaning process. Thus, the sample is first sonicated in acetone for 2 minutes before heating the acetone to 80 °C, where it is held for 5 minutes. These samples are then placed in PRS 3000 for the conventional photoresist cleaning described in Section 3-1-3. After cleaning, the resulting sample has large arrays of isolated graphene patterns.

MoS₂ Growth

The patterned graphene sample is loaded in a quartz tube furnace for powder vaporization growth of MoS₂. The tube is loaded with 300 mg of 99.9995% sulfur powder at approximately 27 cm upstream from the hot zone of the tube, where 2-3 mg of MoO₃ powder is placed. After purging the system with Ar, the hot-zone is heated to 800 °C, while the sulfur is heated separately to 130 °C using heat-tape. The growth is performed for 20 minutes in a constant flow of Ar at near-ambient pressures (710 Torr), producing plumes of growth with coalesced regions up to 50% of the sample surface.

3-3-4. Metal-organic chemical vapor deposition MoS₂ growth

The MOCVD growth is performed in a quartz growth tube with bubblers connected to the system. 99.9% purity molybdenum hexacarbonyl (Mo(CO)₆) and 98% purity diethyl sulfide ((C₂H₅)₂S) is loaded into these bubblers in a N₂ environment. The sample is placed in the furnace

5 cm upstream of the center of the hot zone and heated to 900 °C at a rate of 50 °C/min. The growth processes is done in 565 sccm Ar carrier gas at 10 Torr. Before the growth, a 2 minute nucleation step is performed, where 5 sccm of Mo(CO)₆ and 45 sccm (C₂H₅)₂S is flowed into the tube. The flow is then stopped for 2 minutes before restarting, at which point the flow is held for 1 hour to produce fully coalesced monolayer film with small bilayer regions. After the growth, the system is purged and pumped 3 times with Ar to ensure all precursor is removed from the system before the tube is opened to ambient air.

Nb-doped growths

For Nb doped MoS₂, the exact MOCVD recipe from above is used with an additional Nb source. 5 mg NbCl₅ is placed approximately 46 cm upstream in the growth tube from the target substrate, and heated to 55 °C using an external heat tape. This additional step in the MOCVD process described above produces 5.6 at% Nb doped MoS₂ film. The fermi level positioning of this sample was shown in Figure 2-9b.

3-4. Device fabrication

3-4-1. Transition metal dichalcogenide dispersion

After material growth on SiO₂ on Si substrates, poly(methyl methacrylate) PMMA A6 is spin coated on the sample at 4000 rpm, resulting in a 300 nm thick polymer handling layer. This layer is left to cure at room temperature overnight. To remove the TMDs and the PMMA handling layer from the substrate, the sample is submerged in 1M NaOH at 80 °C. Within minutes, the PMMA layer with TMD underneath separates from the substrate as the thermal SiO₂ layer and Si substrate is etched. The sample is left floating on the solution for ~10 minutes in order to remove any remaining SiO₂ on the handling layer. The handling layer is scooped up from underneath with

a blank, new Si substrate and immediately placed in DI water to rinse the layer and prevent adhesion to the fishing substrate. The handling is then picked up from the top surface using a glass pipette. The handling layer is not fully pulled into the pipette; rather, the handling layer is held using the suction from the pipette such that the handling layer drapes down from the pipette tip. Note that the PMMA layer is no longer planar during this transfer. The layer and TMD growths attached to it is then placed in 200 μL of acetone, dissolving the handling layers and leaving TMD monolayers dispersed in a solution of acetone and PMMA.

3-4-2. Device isolation

After growth of coalesced TMD films, the growth is isolated into rectangles using plasma etching to confine the flow of charged carriers and prevent unwanted current paths. The plasma etch is done in a Plasma-Therm® 720 system or Versalock 700 system with 30/10/10 sccm of SF₆/O₂/Ar plasma at 10 mTorr with RF power of 100W and additional substrate electrode power of 400W. A short etch of 30s is observed to remove 1-3 layers of PV and MOCVD grown MoS₂. This time is increased to 90s for exfoliated films, and is observed to etch through ~10 layers thick exfoliated MoS₂ flakes. The SF₆-based etch is followed by a gentle 2-minute 150/50 sccm O₂/He plasma exposure in a PVA TePla® M4L system to soften the top layer photoresist. The plasma is lit with 100W RF power and 350 mTorr pressure. The sample is then soaked in acetone to remove the top PRS 3012 layer first to minimize the chances of the cross-linked polymer film settling on the TMD film before removing the second PMGI layer using the standard cleaning process.

3-4-3. Device contact

After isolation, the sample is patterned for source and drain contacts and side gates for electrolytic gating. After lithography, the sample is exposed for a short 45 s in 150/50 sccm O₂/He

plasma in a PVA TePla® M4L system with 100 RF power at 350 mTorr to gently remove resist residue on the material in exposed areas on which the metal contact is to be deposited. After the brief cleaning, metal is deposited through electron-beam physical deposition in a Kurt J. Lesker® Lab18 system. First, 5 nm of Ti is deposited at 0.5 Å/s to act as an adhesive layer, then 15nm of Au is deposited at 1 Å/s. After deposition, excess metal lift-off is performed by soaking the sample in acetone. The sample is laid flat and agitated slightly by “swishing around” the solvent dish. This step removes the excess metal and the SPR 3012 on which the metal is deposited. The remaining PMGI layer is removed using the standard polymer cleaning process.

For devices requiring electrolytic gating, a thicker metal layer is necessary in order to prevent puncturing through the metal contact with the electrical probes as the probes push through the solid electrolyte. In such cases, an additional patterning step is necessary. After lithography, a layer of Ti/Au (10 /150 nm at deposition rates of 1 / 2 Å/s) is deposited to reinforce existing contact pads. Lift-off and cleaning processes are repeated in the same method as the first metallic layer.

3-4-4. Solid electrolyte gate

After device fabrication, the samples are prepared for electrolytic gating by collaborator Dr. Ke Xu working with Dr. Susan Fullerton’s group at University of Pittsburgh. The solid electrolyte is prepared and deposited on the target substrate in an Ar glove box with less than 0.1 ppm O₂ and H₂O contamination. This is in order to prevent absorption of water into the solid electrolyte film that can affect its electronic properties ¹⁷⁸. The electrolyte mixture is produced by dissolving 95 kg/mol poly(ethylene-oxide) (PEO) and 99.9% purity CsClO₄ in anhydrous acetonitrile in a 76:1 ratio of ether oxygen to Cs, producing a 1 wt% Cs solution. 25µL of this electrolyte solution is drop casted on a 1 x 1 cm² sample. This is left to sit for 15 minutes in Ar

environment to allow the solvent to evaporate, then cured at 80 °C for 3 minutes to remove any remaining solvent. The resulting solid electrolyte film is approximately 1 μm thick.

3-5. Device analysis setup

3-5-1. Field effect transistor measurements

After solid electrolyte gate preparation and deposition, the sample is transported from the Ar glove box through an Ar filled load lock into a Lake Shore® CRX-VF cryogenic vacuum probe station. This prevents the samples from being exposed to ambient between the deposition of the electrolyte gate and electrical characterization. The probe station system is maintained at room temperature under 10^{-6} Torr vacuum. The electrical signal is driven and measured with a Keysight® B1500A semiconductor parameter analyzer. Before measuring drain current-voltage characteristics, the target gate bias is maintained for 5 minutes in order to make sure the ions within the solid electrolyte is in equilibrium. To obtain transfer curves, the gate voltage is swept from -3 to 3 V with a constant drain voltage of 20 mV. The gate bias sweep rate is limited to a maximum of 0.67 mV/s in order to minimize hysteresis effects. For direct device-to-device comparison, only transfer curves taken on devices with a channel length of 3.5 μm is reported.

3-5-2. Sensing measurements

Sensing measurements using triethylamine (TEA) and o-nitrotoluene (o-NTol) is performed at the Naval Research Labs in Washington D.C. in collaboration with Dr. F. Keith Perkins. The components that make up the sensing system “Sherlock” is illustrated simplistically in Figure 3-2a. Liquid chemical analytes are vaporized in bubbler tubes, through which N_2 is flown to carry the analyte through the line towards the sample. The analyte has an equilibrium partial pressure in the

carrier gas, and the concentration of the analyte is tuned by adjusting the relative mixture of this analyte/N₂ gas with a separate line of clean N₂ using mass flow controllers (MFCs). The minimum and maximum analyte concentration that can be confidently reached is 0.02% and 2% partial pressure respectively. Given the equilibrium partial pressure at 20 °C of TEA of 48600 ppm and o-NTol of 136 ppm, this corresponds to a concentration of approximately 10 to 1000 ppm for TEA and 0.03 to 3 ppm for o-NTol ¹²⁷. While concentrations below these values can be reached, it is not precisely controllable and may be prone to variations during sensing exposures. The chemical vapor line is connected to the fume hood exhaust and to the analyte injection line that ends approximately 1cm above the sample position with programmed valve which controls the direction of the flow. The line is also connected to an in-situ residual gas analyzer (RGA), which can provide information on the chemical makeup and concentration of the incoming gas. The sample is placed in an open-air electrical probe system on an air table to minimize transfer of physical vibrations to the device during measurement. The probe system is equipped with a microscope with a Dolan-Jenner® Model 190 Fiber-Lite fiber optic lamp. Stanford Research Systems® Model SR830 DSP Lock-in amplifiers (LIAs) with alternating current (AC) is used to drive and measure the devices. Using Lock-in amplifiers maximizes signal detection at near-noise levels for low concentration measurements ¹⁷⁹. The eight probes in the system are connected to the input and output of four lock-in amplifiers, allowing for the simultaneous analysis of up to four independent sensors. The valve, gas flow, and lock-in amplifiers are controlled in real-time through a program written by Dr. Perkins. The program outputs a voltage corresponding to the output current across a set resistor, such that the signal is simply given by:

$$S = \frac{\Delta G}{G_0} = \frac{V_{out} - V_{out_{t=0}}}{V_{out_{t=0}}} \quad \text{Eq. 3-1}$$

Though an ideal system would immediately and accurately flow specific concentration of analyte, in reality systems require a stabilization of the gas/vapor flow at the start of each measurement.

Therefore, each measurement is accompanied by 300 seconds of initial stabilization prior to any valve motion in order to allow the system and devices to come to equilibrium.

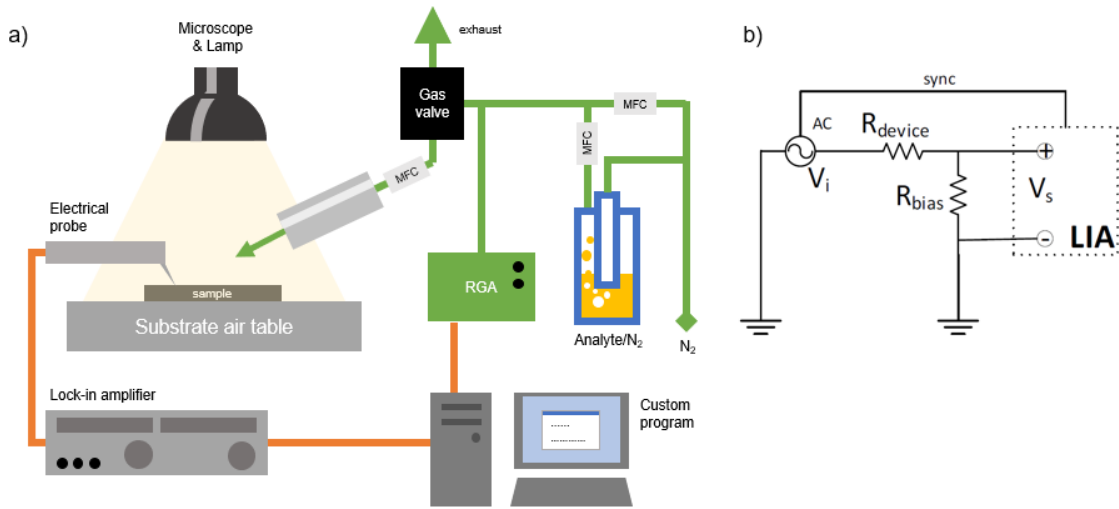


Figure 3-2. a) Illustration of the sensing system setup. b) an equivalent circuit system of the sensor during measurement by the LIA (F.K. Perkins).

3-6. Characterization techniques

3-6-1. Microscopy techniques

Optical microscopy

Optical images are taken using a Nikon® Eclipse L200N series microscope in brightfield using white light without pass filters. The microscope is exposed to ambient air.

Scanning electron microscopy

Scanning electron microscope images are taken in Zeiss® LEO and MERLIN Field emission SEM systems. Samples with metal patterns are imaged using 5 kV acceleration voltage, but samples without metal patterns (i.e. growth only) are imaged using 1 ~ 2 kV in order to prevent

charging of the insulating growth substrate. Working distances of 1.5 ~ 2.5 mm is utilized in InLens mode, which primarily detects secondary electrons.

Transmission electron microscopy

Before microscopy, TEM samples are prepared by depositing 20 nm of SiO₂ on the sample surface with electron beam physical deposition. The area of interest is milled in a FEI® Helios NanoLab DualBeam 660 focused ion beam with Ga⁺ ions. After milling, the sample is loaded in a FEI® Titian3 G2 60-300 S/TEM. Images are taken using 200kV accelerating voltage. In addition, this TEM system is equipped with a SuperX® energy dispersive spectroscopy (EDS) system, so elemental EDS mapping is performed in parallel during TEM imaging.

Atomic force microscopy

Atomic force microscopy is performed using a Bruker® Dimension Icon system in the PeakForce Tapping mode with a Silicon nitride SCANASYST-AIR tip. A force of 10 nN is used with a maximum tip velocity of 10 μm/s in order to prevent loss of feature resolution due to fast scanning. The system is exposed in ambient air but performed in an air-tight enclosure to minimize vibrations through air and upon an air table to minimize vibrations through the floor.

3-6-2. Spectroscopy techniques

X-ray photoelectron spectroscopy

X-ray photoelectron spectroscopy (XPS) is performed using a PHI® VersaProbe II spectrometer. Peaks are fitted using mixed Gaussian-Lorentzian curves. Results are charge-referenced to the carbon (C-C/C-H_x) peak at 284.9 eV ¹⁸⁰.

Raman and photoluminescence

These measurements are done in collaboration with other research groups such that the instrument and methods details differ between thesis subtopics. These details will be discussed in the Materials and Methods section of corresponding chapters.

3-7. Summary

In this chapter, detailed experimental methods used in this dissertation were provided. While parameters for the growth for various materials are detailed in this section and are controlled as precisely as possible during the growth process, there may exist small variations between growths. Characterization of these growths are reported in the Results and Discussion sections in subsequent chapters. Details of the device fabrication processes are also discussed. While these steps are precisely controlled such that the processes are highly repeatable, it is important to note changes in the process parameters may heavily affect device characteristics. Finally, details of characterization techniques are listed. Some parameters will be separately listed in the corresponding sections due to variation in the instrumental details and parameters used between different subtopics.

Chapter 4

Dielectrophoretic Assembly as a Scalable Alternative to Exfoliation for 2-Dimensional Transition Metal Dichalcogenide Integration

The work in reported in this chapter was done in cooperation with Dr. Zhong Lin, previously from the M. Terrones group. Much of the following results are published in D.D. Deng, Z. Lin, A.L. Elías, N. Perea-Lopez, J. Li, C. Zhou, K. Zhang, S. Feng, H. Terrones, J.S. Mayer, J.A. Robinson, M. Terrones, and T.S. Mayer, “Electric-field-assisted directed assembly of transition metal dichalcogenide monolayer sheets,” *ACS Nano*, **10** (5), 2016.

Main subtopic points

- Dielectrophoretic directed self-assembly of microns-sized WS_2 and MoS_2 monolayers is demonstrated. The monolayers assemble conformally across assembly electrodes with minimal folding or wrinkling.
- Raman and photoluminescence spectroscopy reveal little to no damage to the monolayers as a result of the assembly process.
- MoS_2 domains are laterally and longitudinally positioned in a large array with micron-level precision, demonstrating the capability of dielectrophoretic assembly as a scalable 2D material transfer process.
- Direct personal contributions to this work include modeling calculations of field gradient and dielectrophoretic forces, design and fabrication of assembly structures, optimization and demonstration of assembly process, and microscopy characterization.

4-1. Introduction

As discussed in Section 2-2-1, transfer of 2D materials is useful in cases where direct growth options are limited, such as in the fabrication of backgated devices or heterostructure stacks. However, wet transfer techniques provide no control over the positioning of the 2D material on the target substrate. Unless the substrate coverage of the growth is extremely high, this method requires the large-area mapping of the position of targeted flakes and the fabrication of the subsequent device directly around these positions. On the other hand, deterministic transfer methods have

complete control over the positioning of the 2D flakes, but are relatively time consuming due to low yield. In both cases, the methods are not realistic for reliable scaling of device fabrication methods to industrial levels. Dielectrophoretic self-assembly may overcome this challenge of low yield, as the method has demonstrated deterministic assembly of large arrays of dispersed particles¹⁸¹. However, in DEP assembly of 2D materials has been limited mostly to graphene and reduced graphene oxide flakes, with most literature reporting on the chained assembly of many smaller flakes in the specified area^{85,86,182}. Such assembly techniques produce polycrystalline and non-uniformly multilayer channels, such that the transport characteristics may differ from device to device. Assembly of nanoflakes of MoS₂ has been demonstrated¹⁸³, but larger monolayer crystalline domains have not been assembled nor has the effect of such assembly techniques on the quality of TMDs been studied.

This chapter investigates the DEP assembly of WS₂ and MoS₂ monolayers. First, a series of theoretical calculations on the assembly of TMDs with WS₂ as an example is presented, followed by an experimental demonstration of WS₂ assembly and characterization on the effect of assembly on the quality of assembled materials. The method is then extended to MoS₂ monolayers and characterized to confirm the results of WS₂ assembly and study how the method may be applied to other TMDs. Finally, the applicability of this method for large arrays of TMD devices is examined through additional positioning improvements, and considerations for heterostructure assembly for future works is discussed.

4-2. Theoretical discussions on the assembly of 2-dimensional materials

4-2-1. Dielectrophoretic forces on assembling WS₂

While most of the factors of the DEP force equation (Eq. 2-1) govern the magnitude and sign of the force, the electric field gradient portion of the equation, $\nabla|\vec{E}|^2$, provides a vector output,

dictating the direction of the DEP force as well as the magnitude. The field gradient is a vector sum of partial derivatives of the electric field and is a numerical representation of the magnitude of change in the electric field¹⁸⁴. The final positioning of target particles can be controlled through the shape of assembly electrodes and thus the electric field propagating through the dispersion medium.

The electric field gradient map of an assembly system can be approximated using theoretical calculations. Figure 4-1a shows a schematic of a simple assembly structure of a set of $\pm 7.5V$, 100 kHz AC biased parallel electrodes on an insulating substrate. The corresponding electric field gradient immediately above the sample surface is calculated using COMSOL® Multiphysics 4.8 modeling program. The field gradient is shown to be the largest at the edges of the parallel edges of the electrode, where an immediate change in the electric potential is defined. Based on the electric field gradient calculations, a DEP force map of a 3 μm long rod above electrodes separated by 3 μm is calculated and shown in Figure 4-1b in logarithmic color scale. The force is not only strongest at the structure center immediately above the gap, but also directed towards the center of the structure and into the substrate, illustrated by the arrows. This suggests that the defined 3 μm particle would be attracted to the gap and assemble across it under positive DEP assembly. Using estimated material properties of WS₂ ($t = 0.8\text{nm}$, $\varepsilon_m = 4.13$ and $\sigma = 0.5 \text{ Scm}^{-1}$)¹⁸⁵⁻¹⁸⁷ suspended in acetone ($\varepsilon_m = 20$ and $\sigma = 10^{-6} \text{ Scm}^{-1}$)^{188,189} in the DEP calculations, we find that a 3 μm wide particle observes a DEP force of up to 10^{-4} N/m in cross-sectional space immediately above the electrodes. At approximately 10 μm radius away from the center of the assembly gap, the DEP force reduces to 10^{-6} N/m . While this calculation is a cross-sectional estimate in 2D space, the interdigitated electrodes have much smaller lateral dimension than the out of plane dimension such that the system can be considered to extend infinitely in the out-of-plane axis. Based on this, it is assumed that the DEP force map is an acceptable first-order representation of the actual 3D assembly system.

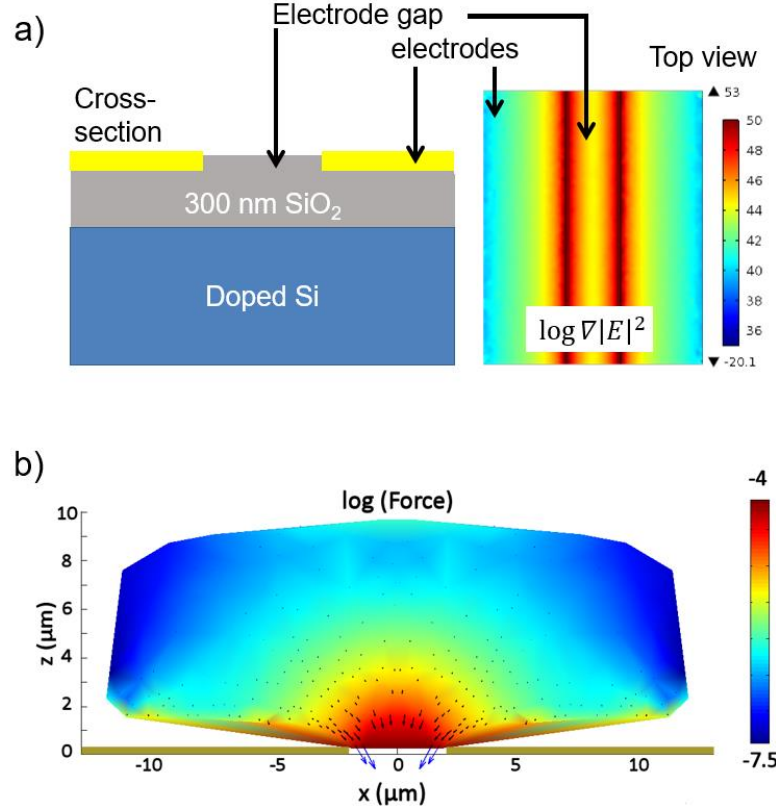


Figure 4-1. a) A cross-sectional schematic of an assembly device with parallel electrodes and a corresponding field gradient map of taken from above. b) A cross-sectional map of the DEP force on a 3 μm wide WS₂ particle as a function of position. Both sets of maps are calculated using COMSOL Multiphysics.

4-2-2. Additional forces during assembly

In addition to DEP forces, a series of first order calculations of additional forces on an assembling particle is made to support or refute the theory that 2D TMD monolayers could be controllably assembled with DEP forces. The gravitational force F_g (causes suspended particles to settle) and buoyant force F_b (causes particles to float to the surface) are calculated. These forces can be calculated using the following equations ¹¹¹:

$$F_g = V_p \rho_p g \quad \text{Eq. 4-1}$$

$$F_B = V_f \rho_f g \quad \text{Eq. 4-2}$$

V_p and V_f are the volumes of the suspended particle and fluid displaced by the particle respectively, and are equivalent. In the case of cross-sectional space, the cross-sectional area of the particle A_p is used instead of volume. g is the universal gravitational force, and ρ_p and ρ_f are densities of the particle and the fluid medium respectively. These calculations are carried out in Table 4-1. It is found that F_g and F_B are on the order of 10^{-10} and 10^{-11} N/m respectively. F_g is calculated to be an order of magnitude larger than F_B , in agreement with the observation that WS₂ sheets settle out of the Acetone-PMMA dispersion over time. Based on the DEP force calculated in the previous section, F_{DEP} will be dominate the forces acting upon the particle by 4 orders of magnitude at 10 μm from the electrode gap center, and 6 orders of magnitude near the electrode surface. Therefore, it is suggested that a particle within 10 μm from the electrode gap center will be driven towards it before settling on the sample.

Table 4-1. A table showing the equation and parameters used for the calculations for gravitational and buoyant forces in competition with DEP forces during assembly ^{185,190,191}.

Force	Equation	Parameters	Calculation
Gravitational	$F_g = w_p t_p \rho_p g$ $= 3 \mu m \times 0.8 nm \times 7.6 \frac{g}{cm^3}$	w_p (width) t_p (thickness) $\rho_p = 7.6 \frac{g}{cm^3}$	$F_g = w_p t_p \rho_p g$ $= [3 \times 10^{-6}] [0.8 \times 10^{-9}] [7.6 \times 10^3] [9.81]$ $= 1.79 \times 10^{-10} \frac{N}{m}$
Buoyant	$F_B = A_f \rho_f g$ $= w_p t_p \rho_f g$	$\rho_f = 0.791 \frac{g}{mL}$	$F_B = w_p t_p \rho_f g$ $= [3 \times 10^{-6}] [1.6 \times 10^{-9}] [0.791 \times 10^3] [9.81]$ $= 3.72 \times 10^{-11} \frac{N}{m}$

However, these calculations assume that the assembling particle is rigid, such that the shape and dimensions of the particle do not change as the particle moves through the medium. In reality, TMD monolayers are flexible and may bend or crumple during the assembly. While this does not affect the gravitational or buoyant force of the particle based on Eq. 4-1 and 4-2, it may affect the dipole moment and thus the DEP force acting on the particle. Furthermore, solvent current flow during assembly due to factors such as drag from particles in motion or convective flow due to resistive heating of the electrodes may further affect the assembly.

4-3. Materials and experimental methods

4-3-1. Transition metal dichalcogenide dispersion

The process of TMD growth and dispersion into acetone was detailed in Sections 3-3-2 and 3-4-1 and illustrated in Figure 4-2. Monolayer domains are grown on approximately 1 cm x 1 cm SiO₂ on Si, and a layer of PMMA handling layer is deposited on the sample surface. The handling layer and TMD growth are removed from the substrate by submerging the sample in heated NaOH. The resulting handling layer and growth is fished out by a Si substrate with additional PMMA layer on the surface. This sample is then submerged in approximately 200 µl of acetone to produce a dispersion of TMD layers in an acetone-PMMA mixture. The TMD sheets in this dispersion settle to the bottom of the mixture within several hours, after which it is nearly impossible to re-disperse into the solution, as the flakes tangle and stick to one another. Attempts to re-disperse the WS₂, such as sonication, lead to significant physical degradation of the films. Therefore, the assembly is done immediately after creating the WS₂ suspension.

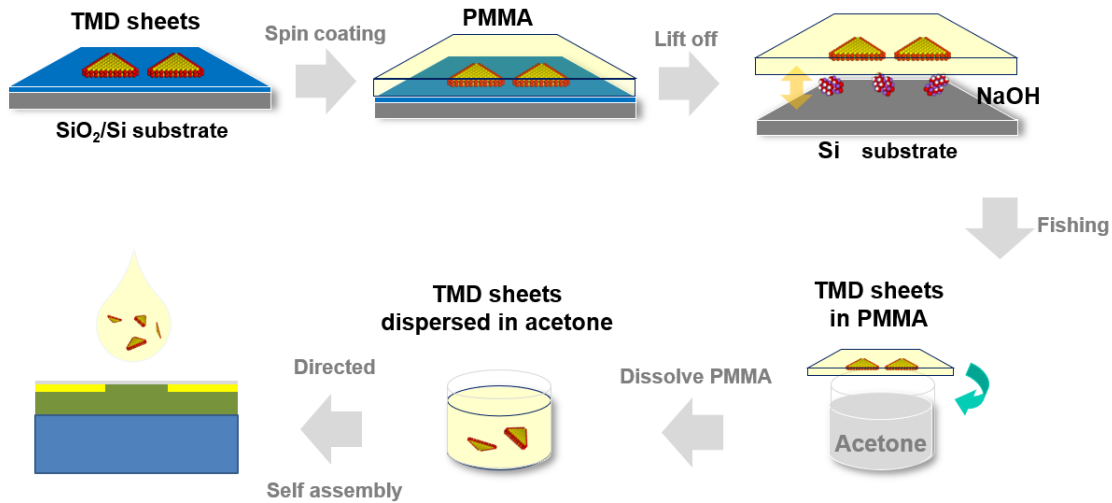


Figure 4-2. A schematic of the series of steps used to transfer PV-grown TMD sheets on SiO₂/Si into an acetone dispersion that can be dropped on an assembly electrode. 3 μ L of the dispersion is used for each assembly system.

4-3-2. Assembly electrode

The assembly electrode is fabricated on 300 nm of wet oxidation SiO₂ on an n⁺ Si substrate. The electrodes are patterned onto the sample using standard optical lithography discussed in Section 3-1-1. After patterning, 10/30 nm of Ti/Au is deposited onto the substrate using electron beam deposition at 0.5 and 1 $\text{\AA}/\text{s}$, such that the electrodes are 40 nm higher than the plane of the electrode gap (the substrate). The final electrode system has 12 sets of interdigitated electrodes that are 150 μm wide with a trench-like gap of 3 μm between each electrode; a simplified schematic of this structure is illustrated in Figure 4-3a.

4-3-3. Dielectrophoretic assembly

For the assembly, an AC signal is used to minimize DC driven vortex flow or any potential of dissociation of solvent components. An illustration of the assembly is shown in Figure 4-3b. A sinusoidal peak-to-peak voltage of 15 V at 100 kHz is applied to the electrode system to produce

the field gradient necessary for assembly. Based on the CM factor plot in Figure 2-6b, the dielectrophoretic force is positive under 1000 kHz for MoS₂ with a conductivity over 0.01 S/cm; this value is approximately the same for WS₂ due to the close dielectric permittivity of the two materials. Thus, a frequency of 100 kHz is used for assembly of both materials. 3 μ L of the TMD-acetone-PMMA dispersion is dropped on the electrode and left to assemble until the acetone completely evaporates in within a minute. This is to ensure that DEP force is driving the particle at all times until the acetone is gone, preventing any redispersion or shifting of the TMD particles during drying. After the signal is removed, the sample is immersed in acetone to remove the PMMA that precipitates out of the acetone on to the electrodes during drying, then rinsed in IPA and dried in N₂.

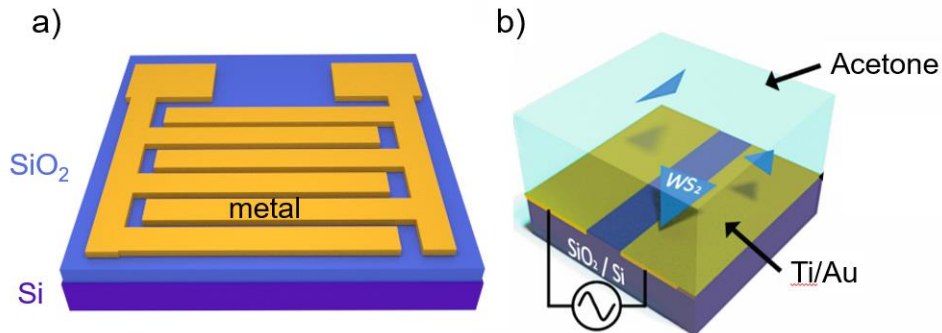


Figure 4-3. a) A simplified illustration of the interdigitated assembly electrodes used for the assembly of WS₂. In the actual device, there are 12 pairs of interdigitated fingers, 150 μ m wide and separated by 3 μ m. b) A schematic of the DEP assembly setup for WS₂ over an electrode gap.

4-3-3. Characterization

Optical, and SEM images are taken using details listed in Section 3-6-1. The Raman and PL spectra are obtained using 514 nm and 488 nm lasers respectively using a Renisha® InVia confocal Raman spectrometer open to ambient air. The laser power is kept under 1.5mW to minimize damage to monolayers. The laser size is approximately 2 μ m in diameter.

4-4. Results and Discussion

4-4-1. Assembly of WS₂ – physical characterization

After cleaning the sample of PMMA residue, the assembly electrode is imaged in SEM for a visual survey of the assembled monolayers. Figure 4-4 shows several scanning electron microscope (SEM) images, with increasing magnification from 4-4a to 4-4c. In the overview image (Figure 4-4a), the light areas correspond to metal electrodes, and the dark areas correspond to the shallow trenches between them. First, we observe that the 2D materials are still present on the surface of the assembly electrodes, despite the sample having undergone solvent cleaning after the assembly. This may be due to the 2D materials having large surface area for adhesive interaction with the substrate; it is also possible that the 2D materials are anchored down to the electrodes, as Au has been reported to have significantly improved adhesion to 2D materials than on SiO₂¹⁹². It is also clear based on this image that the particles are preferentially positioned on the gap with a high density of assembly, and only a small fraction of particles are observed to have settled on the metal electrodes. This confirms the theoretical calculations in Section 4-2-2 that stated the DEP force will dominate over gravitational or buoyant forces. While the calculations could only confirm this to a distance of 10 μm from the electrode center due to limits on the model dimensions, the lack of particles settled on the 150 μm wide electrode suggests that DEP forces dominate far beyond this distance, up to approximately 75 μm from the electrode center.

With increased magnification, it is observed that most particles larger than 3 μm per side assemble spanning the gap, as suggested by the theoretical calculations. However, smaller particles showed a preference to land centered at one electrode edge or the other (Figure 4-4b). This can be explained by considering both electrode edges to be “attractive sites” based on the high electrical field gradient at the electrode edges observed in the map in Figure 4-1. This suggests that a particle large enough to span the gap and contact both edges will prefer to do so to minimize energy, while

small particles are more strongly attracted to one side or the other depending on the direction from which the particles approach the electrode gap. The assembly of sheets spanning the gap is also in agreement with the assembly of 1D particles, where it is reported that nanowires or tubes preferentially assemble spanning the electrode gap due to its induced dipole¹⁸¹. Figure 4-4c shows a series of high magnification images of assembled WS₂ triangles. The assembled monolayer exhibit little to no wrinkling or tearing of the sheets, and are found to be lying conformally on the electrode surface. This is surprising given the flexibility of the monolayers and random sheet orientations in the WS₂-acetone dispersion out of which the monolayers are assembled. This may be due to the assembling monolayers being pulled taught by the induced dipole and the two edges of the electrodes.

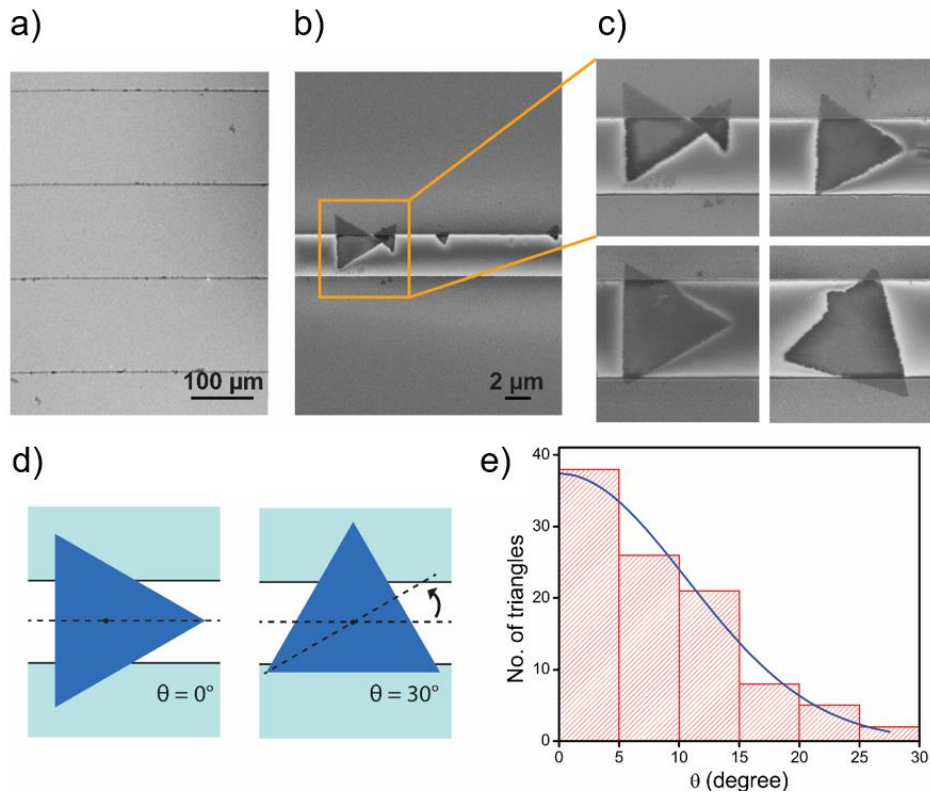


Figure 4-4. a) A low magnification SEM image of the electrodes displaying the preferential positioning of the TMD sheets in the electrode gap regions. b) A closer look at the electrode region. c) Zoomed in images of representative assembled particles. Negligible wrinkling or physical damage is observed. d) An illustration showing the defined particle orientations. e) A survey of 100+ assembled particles and their assembled orientation. There is a clear preference for particles to assemble in the 0° orientation.

In addition to the lack of wrinkles and folds, a preferential orientation of the triangles in the plane of the electrode is observed. To quantify this preference, a survey of the particle orientations is noted for over a hundred WS₂ triangles, with 0° orientation defined to be when one edge of the triangle lies perpendicular to the electrode edges (illustrated in Figure 4-4d). Note that the orientations are periodic with 60° separation, as the 0° orientation and 60° orientation are identical from a geometric perspective. Figure 4-4e plots the result of this survey, where the preference for 0° orientation is confirmed and a bell-shaped distribution is observed.

In order to explain this preference, the torque on an assembling particle 1 μm above the electrode surface is calculated by estimating the system as parallel capacitors as illustrated in Figure 4-5a, where the capacitance is determined by the overlap area between the assembling WS₂ and the underlying electrode. The torque is defined to be the partial derivative of the energy in the system, which is determined by the total capacitance ¹¹¹:

$$T_z(V, \theta) = \frac{\partial}{\partial \theta} W_c(V, \theta) = \frac{\partial}{\partial \theta} \left(\frac{1}{2} C(\theta) V^2 \right) \quad \text{Eq. 4-3}$$

$$C = \frac{k \epsilon_0 A}{d} \quad \text{Eq. 4-4}$$

Where k is the permittivity of the medium, acetone in this case, ϵ_0 is the permittivity of free space, d is the distance between the WS₂ and the electrode surface, and A is the area of the capacitor, in this case the area of overlap between the WS₂ and the electrodes, as a function of the orientation of the triangle. Figure 4-5b shows the semi-analytically calculated plot of the torque on the system as a function of the particle orientation for particles with triangle edges 1.9 to 2.1 times the size of the electrode gap (this ratio is denoted as S). A zero-torque position is observed at 0°, in line with the orientation survey that showed a clear preference for this position. There also exists a second zero-torque position at 30°, but the range at which this position is accessible shrinks as the particle size approaches the size of the electrode gap; at a triangle 2.1 times the size of the gap, the 30° position is favorable when the particle is within approximately 7° from 30°, but the range decreases to within

3° when the triangle size decreases to 1.9 times the size of the gap. most of the particles in this growth is observed to fall under two times the size of the gap ($6 \mu\text{m}$), making the 0° position far more preferable. These calculations further support the theory that the 0° orientation preference is driven by the system moving towards lower energy configurations, manifesting in a torque that exhibits rotational positioning control over assembling triangles.

Note that this plot is an approximation calculated with specific assumptions regarding the monolayer assembly. The calculations assume the triangles rotate around a static center of mass as illustrated in Figure 4-4d; in a real assembly, the triangle as a whole is able to move in the lateral plane to minimize its potential energy. In addition, the monolayer is assumed to approach the electrode gap such that plane of the monolayer is entirely parallel to the plane of the electrode surface. Not only is it possible that the monolayer is not flat as it approaches the electrode surface due to its flexibility, it is also possible for the particle to be tilted such that the monolayer plane is not parallel to the substrate surface. While such assumptions may lead to deviations in the calculated in-plane torque, the agreement between the torque plot in Figure 4-5b and statistical survey of the particle orientations in Figure 4-4e suggests that the trend revealed in the torque plot may still be applicable.

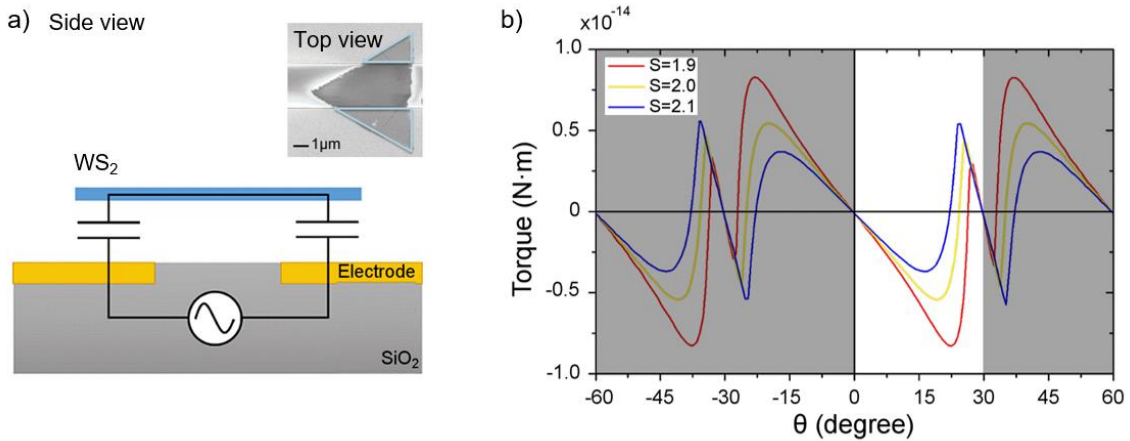


Figure 4-5. a) An equivalent circuit schematic of a particle in suspension above the electrode. The inset shows an SEM image of an assembled particle, illustrating the region of the particle that overlaps with the electrode. c) A semi-analytical plot of the in-plane torque as a function of particle orientation for triangles 1.9 ~ 2.1 times the size of the electrode gap.

4.4-2. Assembly of WS₂: optical characterization

The optical characteristics of the materials pre- and post-assembly is studied in partnership with Dr. Zhong Lin. The measurements are performed with the laser centered over the gap, on the SiO₂ substrate, or on the electrode, on a thin film of Au. Figure 4-6b and c show a comparison of the PL and Raman spectrum of the WS₂ flakes on the growth substrate using 488 nm and 514.5 nm lasers respectively. For each method, the material is characterized before assembly (on the SiO₂ growth substrate), in the electrode gap post-assembly, and on the electrode post-assembly. First, it is confirmed from the pre-assembly characterization that the material exhibits a 2H-WS₂ PL peak at around 2.0 eV ¹⁹³. The Raman spectra exhibits a peak at 355 cm⁻¹, corresponding to a monolayer WS₂ E_{2g} peak ¹⁸⁵. In addition, a peak at 420 cm⁻¹ corresponding to a WS₂ A_{1g} peak is also observed. The peak position, relative intensity, and full-width half maximum (FWHM) of the fitted exciton peaks in the PL spectrum is listed in Table 4-2. In the PL spectrum shown in Figure 4-6b, the peak corresponding to the charged exciton peak, labeled X⁻, is reduced and both the charged and neutral exciton peaks (X⁰) red shift slightly due to the monolayers being released from the original substrate ^{194,195}. However, the FWHM of the exciton peaks do not widen significantly after the assembly, suggesting the materials are not damaged in the process. The Raman spectra of the WS₂ also exhibit minimal change in the E_{2g} or A_{1g} peaks after being assembled, and the LA(M) peak corresponding to structural defects show no observable difference post- assembly ¹⁹⁶. This corroborates the PL data, suggesting the assembly process does not damage the monolayers.

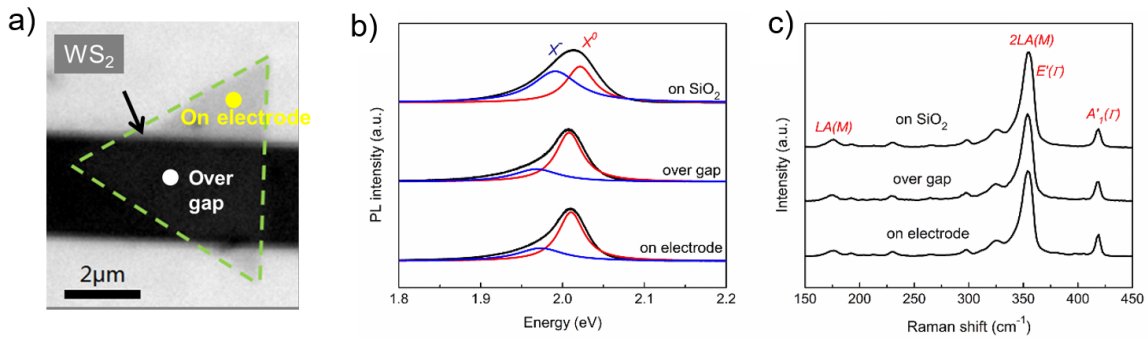


Figure 4-6. a) A schematic of an assembled particle with example positions of the “on electrode” and “over gap” positions. b) A comparison of the PL spectra of WS₂ taken before and after assembly with fitted curves for the Trion X⁻ and Exciton X⁰ peaks. c) a comparison of the Raman spectra of WS₂ taken before and after assembly.

Table 4-2. Details of the peak fitting of the exciton and trion peaks in the WS₂ PL spectra shown in Figure 4-6 above.

	EXCITON X ⁰			TRION X ⁻		
	Energy (eV)	Relative intensity	FWHM (meV)	Energy (eV)	Relative intensity	FWHM (meV)
ON SIO₂	2.02	0.42	42	1.99	0.58	67
OVER GAP	2.01	0.69	39	1.97	0.31	67
ON ELECTRODE	2.01	0.68	38	1.97	0.32	69

4-4-3. Assembly of MoS₂

In addition to WS₂, similar assembly tests are done with MoS₂ in order to assess the possibility of extending the DEP assembly method to other 2D TMDs. The material dispersion preparation, assembly structure, and assembly parameters are identical to the earlier case with WS₂. Figure 4-7a shows an SEM image of an assembled MoS₂ monolayer. Like the case with WS₂, the monolayers were observed to preferentially assemble directly over the electrode gap, with little physical folding of the sheets. However, unlike the triangular WS₂ monolayers, no preferential orientation is observed. This is likely due to the MoS₂ domain shapes being hexagonal, as it offers minimal differences in electrode overlap area as the orientation of the particle is varied. Based on Eq. 4-3 and 4-4, this minimal change in area corresponds to a minimal torque on the hexagonal monolayers. Figure 4-7b shows the Raman spectrum for the MoS₂ before assembly, over the electrode gap post-

assembly, and on the electrode post-assembly. First, the material exhibits peaks at 384 and 408 cm⁻¹, corresponding to the E_{2g} and A_{1g} peaks in 2H-MoS₂. The spectra after assembly are near identical besides a shift to lower wave numbers post-assembly due to release of the material from the growth substrate., suggesting no significant damage is incurred on the material during assembly. This agreement of the assembly results and lack of damage on the material between WS₂ and MoS₂ is encouraging, suggesting that this technique maybe extended further to other 2D TMD materials.

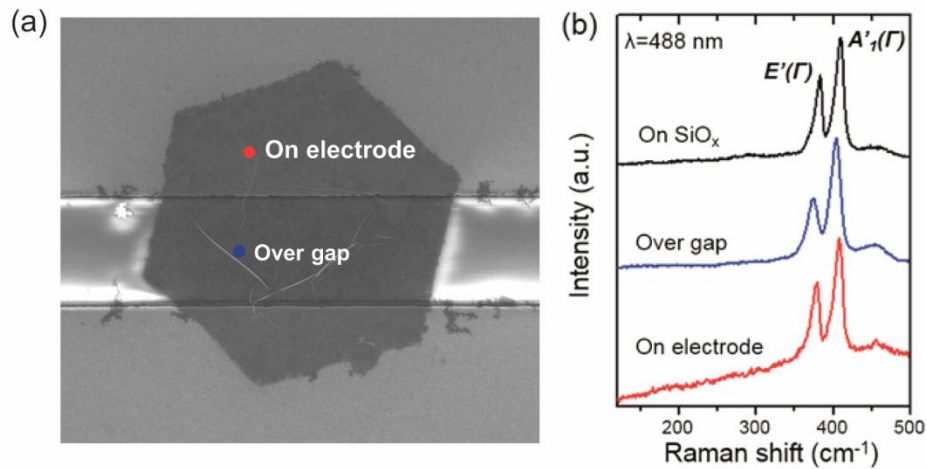


Figure 4-7. a) an SEM image of a monolayer crystal of MoS₂ is assembled across a 3 μm wide electrode gap. The wrinkle in the center of the monolayer is believed to stem from strained growth on the SiO₂/Si substrate. b) Raman spectra obtained from MoS₂ before and after assembly. No significant change is observed post-assembly.

4-4-4. Lateral positioning control of transition metal dichalcogenide flakes

While the large scale, high density assembly of TMDs along parallel electrodes has been demonstrated thus far, such simplistic designs do not offer control of a monolayer's lateral positioning along those parallel electrodes. This is necessary in order to fully pin point material location for scalable device fabrication. To this end, adjusted assembly electrode designs are studied for more to produce a DEP assembly structure with improved positioning control. Figure 4-8a shows a schematic of a finger electrode system, where the parallel electrode gap is widened

from 3 μm earlier in this chapter to 100 μm . From these separated electrodes, metal fingers are extended towards the center to create regions of high field gradient. In order to screen the field gradient at the separated electrode edges and maximize the relative field gradient in the fingertip area, a layer of SPR 3012 photoresist is spin coated at 4000 rpm and patterned with open wells around defined regions using optical lithography. A top-view field gradient map of a similar structure with three finger extensions is show in Figure 4-8b. The electric field outside of the open well is reduced dramatically, making the finger tips more attractive for assembly.

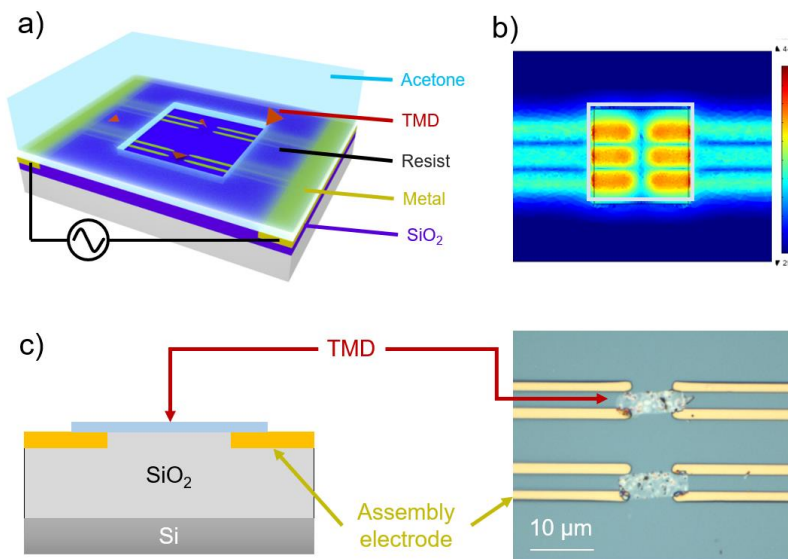


Figure 4-8. a) An overview of the assembly structure with extended fingers and a patterned resist well. b) Top view map of the electric field gradient on a similar electrode structure. the field gradient appears highest around the finger tips. c) A cross-sectional schematic and resulting MoS_2 film assembly on the extended finger electrode, showing the positioning and orientation control of this assembly design.

For these growths, a polycrystalline MoS_2 film grown using the same method as the single domain growths, but for an extended amount of time to produce fully coalesced, 1~2-layer MoS_2 film. After the growth, the MoS_2 is etched into rectangular 10 μm by 3 μm shapes to create uniformly shaped and sized sheets required for device arrays. The MoS_2 sheets are removed from the substrate and into an acetone-PMMA dispersion using the same process as WS_2 , then assembled onto the electrodes using the same parameters. Figure 4-8c shows an optical image of the resulting assembly. The precise positioning of rectangular polycrystalline films is demonstrated, and these

MoS_2 rectangles are observed to be centered between the tips of the extended metal fingers, and oriented such that the longer dimension spans the gap between the two sides of the applied signal. It is noted that the assembly density of these materials is lower than assembly on parallel electrode structures, with a device assembly rate of approximately 25%. This is likely due to the wide lateral separation between regions of high field gradient, such that most particles are far from the open well region where the DEP forces are large enough to attract the assembling particles in the defined areas. This may be improved by increasing the density of the open-well regions as well as the TMD particle density within the assembling solution. The precise positioning control exhibited by these adjusted assembly electrodes are encouraging results, suggesting that DEP assembly is a viable alternative to exfoliation for fabrication of large arrays of uniform devices.

4-5. Summary & Future work

In summary, DEP assembly is tested using WS_2 and MoS_2 on a simple parallel electrode structure, and the effect of the assembly process on the TMDs are assessed using optical characterization. The TMDs are found to assemble centered on the electrode gap region with minimal physical deformations. Furthermore, a preferential orientation of triangular WS_2 is observed, which is likely driven by minimization of the particle energy as it assembles according to analytical calculations. Optical characterization of the TMDs before and after assembly reveal that no observable damage is incurred on the sample during the process. Finally, an example of an assembly structure design with more precise control of the positioning of DEP assembled TMDs is demonstrated. The TMDs assemble in pre-determined regions with few-micron precision, and also exhibited a preferential orientation.

It is envisaged that this method can be a controllable and scalable alternative to conventional transfer techniques for fabrication of 2D TMD devices. While assembly of single material type is achieved in this chapter, it is envisaged that sequential introduction of additional

2D materials may be used to fabricate van der Waal heterostructures by sequentially assembling multiple material types in predefined positions. Figure 4-9 shows a cross-sectional field gradient map before and after the assembly of a WS₂ sheet over the 3 μm electrode gap in the center. While a change in the shape of the gradient map is observed immediately above the center of the electrode gap, the location of highest gradient (the electrode edges) and relative magnitude of the field gradient does not seem to change significantly, suggesting that the DEP forces responsible for driving TMD sheets to the electrode gap may persist after assembly of the first layer. In order to further assess the possibility of using the DEP assembly method for the fabrication of heterostructures, the effect of an assembled 2D layer on subsequent assemblies must be analyzed.

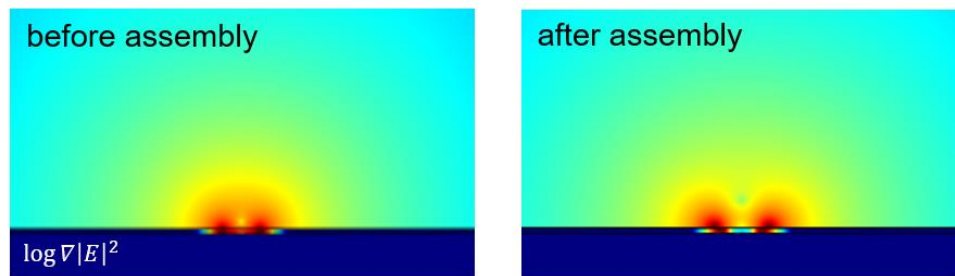


Figure 4-9. A cross sectional map of the field gradient in logarithmic color scale. While the geometry of the field gradient differs before and after assembly, the relative high-gradient positioning and magnitude are similar. This suggests that the DEP force at the electrode gap still persists and assembly of subsequent 2D TMD layers may be possible for the fabrication of van der Waals heterostructures.

Chapter 5

MoS₂- Epitaxial Graphene Heterostructures as Electronic Contacts

The work reported in this chapter is in cooperation with Ms. Shruti Subramanian in the J.A. Robinson Group. Much of the results are published in S. Subramanian, D.D. Deng, K. Xu, N. Simonson, K. Wang, K. Zhang, J. Li, R. Feenstra, S.K. Fullerton-Shirey, J.A. Robinson, “Properties of synthetic epitaxial graphene/molybdenum disulfide lateral heterostructures”, Carbon, 125 (2017).

Main subtopic points

- Completely transfer-free direct growth of type-matched epitaxial graphene–MoS₂ spatially lateral heterojunctions is demonstrated. The interface is an atomically pristine vertical overlap with no intermixing or contaminants observed at the junction.
- Using type-matched graphene as electrical contact to the MoS₂ channel results in a ~20x improved contact resistance compared to Ti/Au-contacted MoS₂.
- Compared to Ti/Au-contacted FETs, epitaxial graphene-contacted MoS₂ field effect transistors exhibit ~3.5x faster turn on with a subthreshold swing of 89.2 mV/dec and two orders of magnitude higher on/off ratio of 10⁵.
- Main contributions to this work include device design, support in optimization of the heterostructure growth process, post-growth/transfer two-terminal device fabrication, and analysis of electrical characteristics.

5-1. Introduction

5-1-1. Graphene contact to MoS₂

Making low-barrier electrical contacts to TMDs for electronic applications remain a challenge, as briefly discussed in Section 2-4-3. As there are no direct bonds between the metal and the TMD surface, the carriers must tunnel through the van der Waals gap, increasing the contact resistance of such junctions ¹⁹⁷. Furthermore, interface dipole formation across the gap can cause the Fermi level to be pinned to unwanted positions ¹⁹⁸. On the other hand, the hybridization of the

metal-TMD interface, through the creation of metal-TMD bonds, creates gap states that could further cause Fermi level pinning. These challenges are especially evident for MoS₂. Various studies on improving the electrical contact to MoS₂ have been reported, including the conversion of the underlying MoS₂ from semiconducting 2H to 1T, deposition of adhesive metal layers such as titanium at ultra-high vacuum, and surveys of various metals contacts and the resulting contact characteristics ^{62,199,200}. As discussed in Section 2-4-3, there are conflicting reports on the effectiveness of choosing contact materials based on the metal work function relative to MoS₂. While some studies report device performance correlating to metal work functions, others report minimal effect of metal species on the SB height due to Fermi level pinning. This discrepancy may be due to the effects of processing conditions on the degree of interface hybridization that may affect the Fermi level pinning of the metal-TMD interface.

In an effort to circumvent such challenges, graphene has been utilized as an electronic contact to MoS₂, with encouraging results ^{201,202}. Reports consistently show nearly an order of magnitude improvement in electron transport of graphene mediated contacts compared to conventional metallic contacts (see Figure 5-1b). Furthermore, graphene itself can be gated to increase carrier concentration and improve carrier injection into MoS₂, further improving the FET characteristics through the compounding effect of channel and contact modulation ^{203,204}.

Historically, graphene-MoS₂ contacts have been produced through exfoliation, specifically through deterministic transfer techniques ^{201,205}. These methods are time consuming and low-yield. In response, the direct growth of lateral MoS₂- graphene heterostructures have been reported, as shown in Figure 5-1c, with successful demonstrations of working logic devices ²⁰⁶⁻²⁰⁸. While this is promising for large thorough-put device fabrication, these reports have been limited to CVD graphene, which is most commonly grown on metallic substrates and require transfer to an insulating substrate before device fabrication, as discussed in Section 2-2-3. In addition, transferred CVD graphene is intrinsically lightly p-type, while MoS₂ is generally naturally n-type due to the pervasiveness of chalcogen vacancies ^{125,209-212}. While CVD graphene contacts to MoS₂ is an

improvement from metallic contacts, it is expected that utilizing type matched n-type EG contacts to MoS₂ could provide further improvements based on the alignment of the graphene Dirac point within the MoS₂ gap and the smaller electron affinity of n-type graphene ^{213,214}. The goal of the research detailed in this section is to utilize intrinsically n-type epitaxial graphene in contact with directly grown MoS₂ to fabricate electronic devices with synthetic contacts and study the electronic transport across this heterojunction.

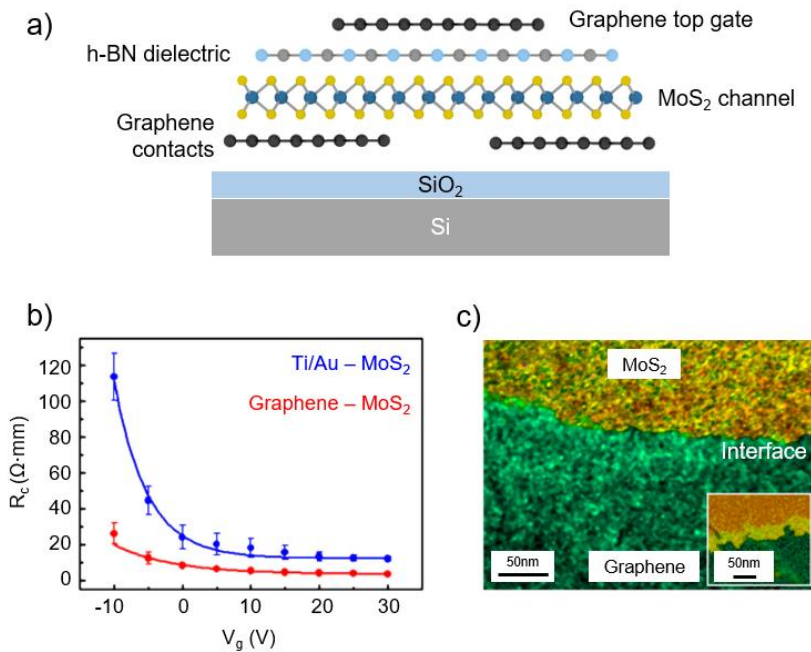


Figure 5-1. a) A cross-section illustration of a 2D FET, with graphene contacts to the MoS₂ channel. b) A direct comparison between contact resistance between metal-contacted and graphene-contacted MoS₂ FETs over a range of gate voltages (adapted from reference ²⁰¹). c) A dark-field TEM image of a directly grown MoS₂-CVD graphene lateral heterojunction, showing the abrupt material interface (adapted from reference ²⁰⁸).

5-2. Materials and experimental methods

5-2-1. Growth and fabrication of devices with synthetic contacts

A completely transfer-free growth method is utilized for the synthesis of the heterostructures. The process of the growth and device fabrication is illustrated in Figure 5-2a. The

growth and patterning of epitaxial graphene and subsequent PV growth of MoS₂ is detailed in Section 3-3-3. After the growth of the heterostructure, the growth is isolated into rectangular device regions using standard TMD isolation etch process discussed in Section 3-4-2. After patterning, 5/15 nm of Ti/Au metal layers are deposited on the sample using electron beam deposition. An additional layer of metal is deposited onto the pre-existing contact pads (Ti/Au 10/150 nm) using electron beam physical deposition in order to provide thicker metal for the electrical probes to sink into during electrical characterization.

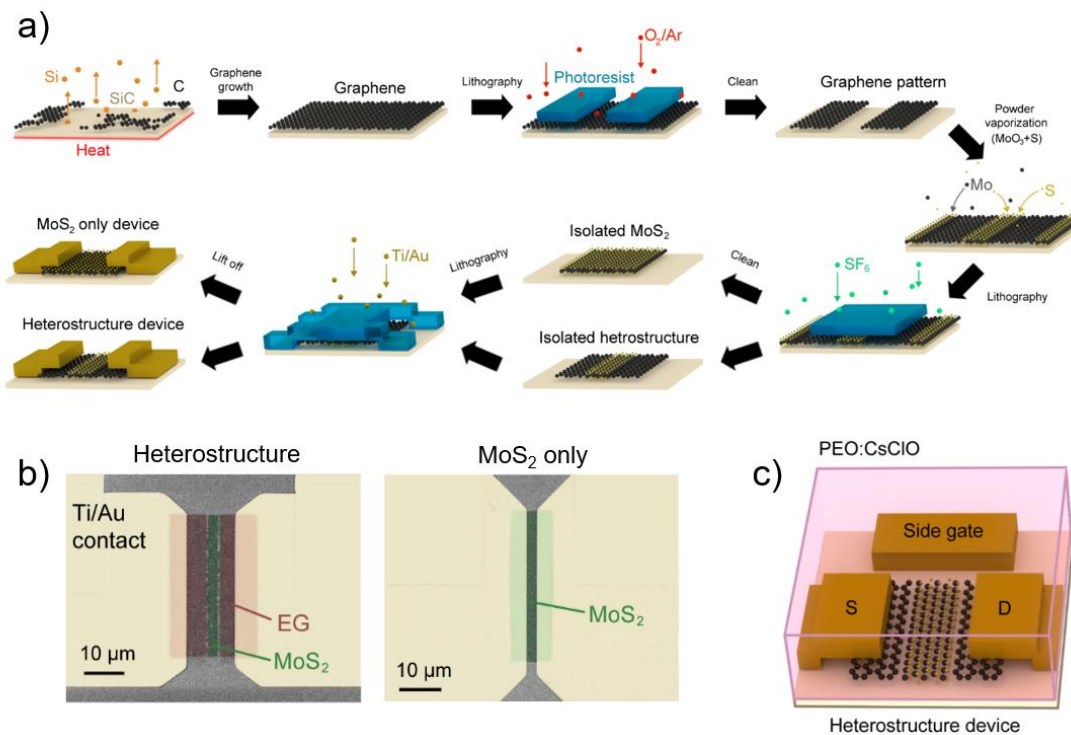


Figure 5-2. a) A schematic of the fabrication process of EG-MoS₂ heterostructures. b) False colored SEM images of the heterostructure and metal-contacted devices. c) A schematic of a heterostructure device with an electrolytic global gate.

Two main types of heterostructure devices are fabricated: devices with graphene as the direct contact to MoS₂, and devices without graphene such that the metal is in direct contact with MoS₂. Figure 5-2b shows an SEM image of these devices. For graphene-contacted devices, the metal is contacted on the graphene 5 μm away from the MoS₂ channel edge on both sides, while the metal-contacted devices fully cover the graphene and overlap directly onto the MoS₂ with a

minimum contact overlap length of 5 μm . By utilizing heterostructure growths for the Ti/Au contacted sample as well, it is ensured that the MoS₂ channel in both device types are as similar as possible. This allows for the direct comparison of the electronic characteristics of the two types of devices. After fabrication, solid electrolyte is deposited on the sample for gating using the methods detailed Section 3-4-4, resulting in a device as illustrated in Figure 5-2c.

5-2-2. Device fabrication of exfoliated epitaxial graphene-MoS₂ devices

In addition to directly grown heterostructures, exfoliated heterostructures are also studied. After EG growth, the sample is patterned and etched into strips of 1 μm wide, approximately 15 μm long graphene extensions separated by 1 to 5 μm . These extensions are contacted by metal leads patterned in optical lithography with 5/15 nm of Ti/Au. After lift-off, MoS₂ flakes are exfoliated and deterministically transferred on the EG extension by a collaborator, Mr. Dacen Waters from the R. Feenstra group at Carnegie Mellon. First, MoS₂ flakes are exfoliated from bulk using the scotch tape method onto an SiO₂ substrate. A polycarbonate (PC) handling layer is heated and attached to a clear transfer slide. MoS₂ flakes are picked up by stamping the PC film onto the SiO₂ substrate. The flakes are then aligned to predefined regions on the target substrate under a microscope. The handling layer and exfoliated flakes are stamped onto the substrate and heated to detach from the transfer slide. The PC handling layer is dissolved in chloroform, leaving behind exfoliated flakes in the target position. This method is performed entirely in a N₂ filled glove box to prevent oxidation of TMDs. After the samples are received from the collaborator, the transferred flakes are mapped out using SEM to design an isolation layer for the MoS₂ channels based on the flake shapes and positions. This design is then transferred to the sample using EBL (Section 3-1-2). Due to the exfoliated MoS₂ layers being thicker than PV or CVD grown samples (up to ~10 layers thick in contrast to 1~3 layers), the MoS₂ isolation etch time is increased to 90 seconds in order to ensure that the channels are isolated and no unwanted current paths are available. Like the

directly grown heterostructure devices, solid electrolyte is deposited on these devices post-fabrication for gated measurements.

5-2-3. Characterization tools

Details on SEM, AFM, TEM, EDS, and XPS characterization techniques are discussed in Section 3-5. Raman and PL measurements are obtained with a Horiba® Scientific LabRam HR Evolution Raman spectrometer with a back illuminated deep depleted detector using a Oxxius® 532nm laser. For PL mapping, a confocal microscope with a 100x 0.9 numerical aperture objective lens is used, with a resolution of 0.2 μm between data points. The laser is used at \sim 0.39 mW power with a grating of 300 gr/mm. Low energy electron diffraction and reflectivity measurements were conducted by Dr. Jun Li, previously of the R. Feenstra group at Carnegie Mellon. Measurements were conducted using an Omicron® SPECTALEED system with a LaB₆ thermionic cathode emitter on growths prior to electrolytic deposition in order to maximize the sample signal.

5-3. Results and discussion

5-3-1. Epitaxial graphene – MoS₂ heterostructures

As-grown EG-MoS₂ heterostructures are characterized before the subsequent device fabrication process. False-colored top-view SEM images of the directly grown EG-MoS₂ heterostructures is shown in Figure 5-3a. Due to the plume-like growths that result from PV growth methods as discussed in Section 2-2-2, The coalescence of the MoS₂ film varies from fully coalesced at the most upstream edge of the substrate to uncoalesced at the downstream edge. The MoS₂ is found to grow on the exposed SiC surface where EG has been etched away. Furthermore, studying the morphology of the uncoalesced growth reveals that the MoS₂ appears to preferentially

grows around the edges of the EG rectangles. Due to this template-like growth, regions between closely spaced graphene rectangles are fully coalesced even in regions away from the upstream edge. Minimal MoS₂ growth is observed on the EG rectangles. An AFM image of a series of graphene stripes surrounded by MoS₂ growth is shown in Figure 5-3b. These images show there exists small, sub-micron multilayers centered on the edge of the etched graphene. This suggests that the MoS₂ growth is nucleating at the high-energy edge of the graphene rectangles, then extending outwards onto the exposed SiC substrate. A photoluminescence map in the same location is taken for the MoS₂ peak around 1.83 eV and is shown in Figure 5-3c²¹⁵. The areas where EG has been removed show significant PL signal, suggesting high quality MoS₂ in those regions. Furthermore, the lack of MoS₂ PL on the graphene rectangles confirm the negligible growth of MoS₂ on top of the EG, as observed in SEM. Based on these results, it can be concluded that the heterostructure growth is successful, with spatially separated EG and MoS₂.

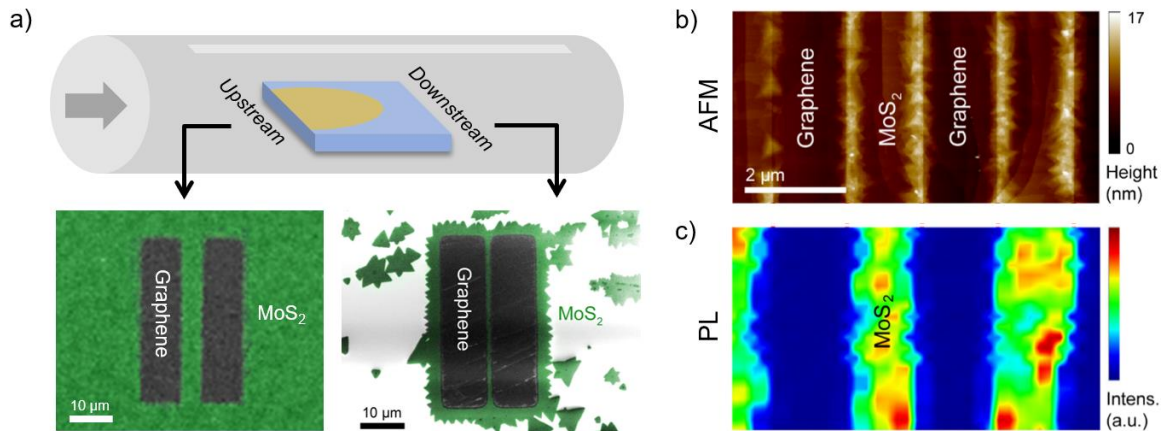


Figure 5-3. a) A schematic of the plumed growth on the substrate and corresponding false colored SEM images of the EG-MoS₂ heterostructure. The uncoalesced regions showcase the MoS₂ growth outwards from the edge of the EG. b) an AFM image and c) a PL map of a series of EG rectangles with MoS₂ growing around them.

In order to better understand the heterojunction interface, cross-sectional TEM images are taken. TEM images of the individual materials away from the heterojunction edge show the growth is high quality with clear layered crystalline structure. Figure 5-4a shows 3-layer EG, while Figure

5-4b shows 1~2 layers of MoS₂. Figure 5-4c, a TEM image of the EG-MoS₂ interface, reveal the heterojunction is comprised of a small region of overlap of multilayer MoS₂ onto the epitaxial graphene. This is a consistent phenomenon observed over several locations and samples; the overlap was observed to range from 50 nm to 200 nm depending on the growth conditions and position on the sample relative to the upstream edge. In contrast to the mono- to bi-layer MoS₂ growth observed away from the interface, the MoS₂ growth in the immediate vicinity of the graphene is multilayered, in agreement with AFM mapping. Remarkably, the material in the overlap region maintain the high crystalline quality observed in regions away from the interface, with no significant concentration of clear atomic defects. A short region at the edge of the epitaxial graphene reveal defective EG, but there is no observable bonding between the MoS₂ and EG layers at the edge of these layers. In addition, the interface between the two materials is pristine, lacking any impurities such as polymer residue that is common in exfoliated structures^{216,217}. It is notable that there is a few-nm thick layer of oxidized SiC (SiO_x) upon which the MoS₂ seems to be grown on. This layer is likely a result of the O₂-based graphene etch process performed before MoS₂ growth.

Energy dispersive spectroscopy (EDS) is also performed on the interface area. Studying the elemental mapping shown in Figure 5-4e, no intermixing of the elements between EG and MoS₂ can be observed. These results suggest the spatially lateral heterostructures have a short but highly pristine vertical overlap of the MoS₂ over EG. Having such a pristine van der Waals heterojunction is highly advantageous in terms of electrical transport, as it minimizes sources of electron scattering.

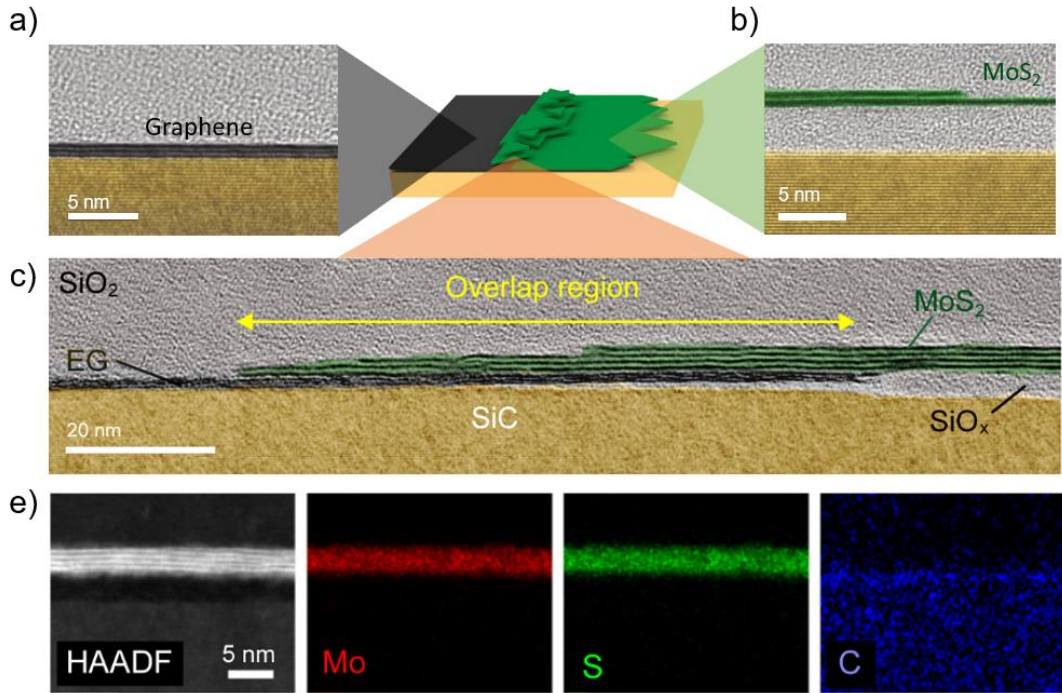


Figure 5-4. Cross-sectional TEM images of a) graphene, b) MoS₂ c) and the heterostructure interface. These reveal the high quality of the growths and a pristine overlap region. e) A series of elemental mapping obtained using EDS that further prove that the interface is sharp with no intermixing.

5-3-2. Device characteristics of epitaxial graphene-contacted MoS₂ field effect transistors

In order to directly compare the contact quality between EG-contacted and Ti/Au-contacted devices, large arrays of both devices (up to 200 devices per type per 1 x 1 cm² substrate) are fabricated and characterized on a single sample under the same conditions. These structures are shown in Figure 5-2b. Total resistance values of both types of devices before and after deposition of the solid electrolytic gate is plotted in Figure 5-5a as a function of channel length. First, the deposition of the electrolyte itself is observed to heavily affect the MoS₂ through surface charge transfer doping^{218,219}, and significantly decreases the resistance of the device by approximately four orders of magnitude. However, the resistance of the heterostructure devices are lower than that of the Ti/Au contacted devices both before and after the electrolytic gate deposition. In order to more

quantitatively compare the contacts, contact resistance values are extracted from the gated devices using the TLM method. Figure 5-5b illustrates this method for a series of heterostructure devices with varying channel lengths at varying gate voltages as a plot of device resistance against channel length. While there is some noise in the data due to device-to-device variation, the resistance values exhibit a relatively linear relationship with channel length. A linear line is fit through each set of devices to extract a contact resistance at a given gate voltage. The results are shown in Figure 5-5c, which reveal that EG-MoS₂ contacts have approximately 20 times reduced contact resistance at every gate voltage in comparison to the Ti/Au-MoS₂ contacts. While this is in agreement with other reports in literature of graphene decreasing the contact resistance, most previous papers reported an improvement of less than an order of magnitude^{201,202}. This may suggest that using type matched n-type EG as contacts to MoS₂ improves contact transport more significantly than using CVD p-type graphene, but a direct comparison to heterostructure devices using p-type graphene is necessary to confirm.

While the minimum achieved contact resistance of 10.5 kΩ•μm is still significantly larger than the industry goal of ~0.2 kΩ•μm, it is expected that this value can be further reduced²²⁰. Based on the AFM image in Figure 5-3b, the multilayer growth at the graphene-MoS₂ overlap is non-uniform along the interface in terms thickness and multilayer growth dimensions. Optimization of the growth parameters may improve the uniformity of this overlap growth as well as increase the width of the overlap region to achieve larger transport area through the interface. Also, it is noted that the heterostructure contact resistance values includes the contact resistance between the EG and Ti/Au. This interface could be improved through various methods, such as further cleaning of the material before metal deposition or post-deposition annealing²²¹.

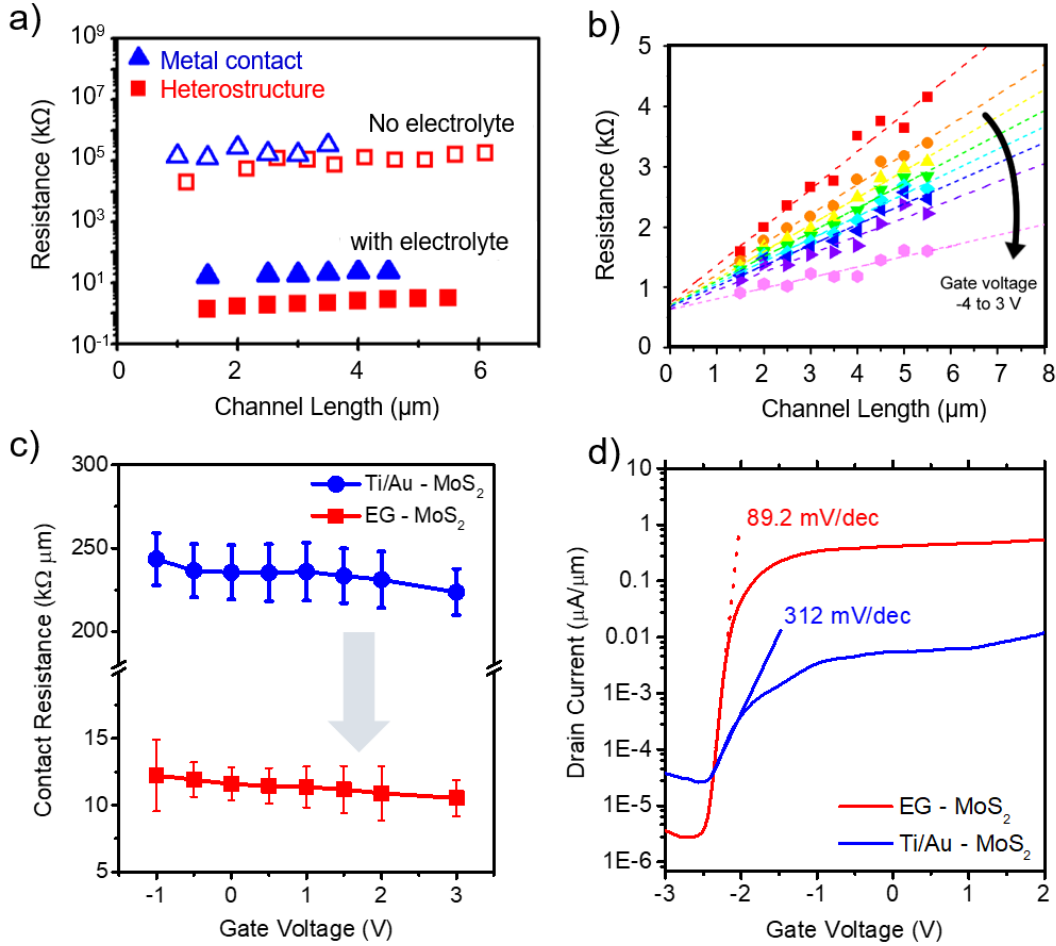


Figure 5-5. a) The total device resistance of heterostructure and metal contacted devices before and after the deposition of the electrolytic gate. b) An example of the TLM contact resistance extraction method, where the resistance of a series of devices are recorded and fit as a linear function of channel length. c) A comparison of the contact resistance of the heterostructure devices and the metal contacted devices. d) The transfer curves of a heterostructure device and a Ti/Au contacted device.

In addition to contact resistance analysis, full FET characteristics of the two types of devices are studied in order to ascertain if the improvement in the contact translates into an improvement in the FET characteristics of the device. Figure 5-5d plots the I_D - V_G transfer curves of 3.5 μm channel length MoS₂ FETs with EG or Ti/Au contacts. Not only does the heterostructure device exhibit a higher on/off ratio of 10^5 in comparison to only 10^3 for the Ti/Au contacted device, the SS also decreases by 71% from 312 to 89.2 mV/dec. Based on these metrics, we conclude that using n-type EG as the contacts to a MoS₂ FET improves the contact resistance, and leads to a significant improvement in the overall FET device performance. While part of this improvement

in the device characteristics is suspected to be directly related to the improved contact resistance of the heterostructure device, it may also be partially due to the modulation of the graphene contacts due to global gating of the devices, whereas Ti/Au metal contacts are not modulated by the gate field. In order to deconvolute the effect of graphene contacts, it is necessary to directly compare FET characteristics of global gating vs local gating of the MoS₂ channel.

5-3-3. Band alignment comparison of epitaxial graphene-MoS₂ and Ti/Au-MoS₂

In addition to electrical measurements, low energy electron reflectivity (LEER) is employed to directly study the band alignment of the contacts to understand the differences in the band alignment of the contacts. This technique measures the relative vacuum levels of the materials in contact. Because the energy difference from the work function or electron affinity is constant in a material and the fermi level is constant across a junction, a relative band alignment across the heterojunction can be estimated from data obtained using LEER. Figure 5-6a shows a diffraction image obtained using low energy electron diffraction (LEED) in an overlap region. The individual points correspond to graphene and its aligned, hexagonal structure. On the other hand, there exists a ring of data points corresponding to MoS₂^{222,223}. This suggests the MoS₂ on the overlap region is polycrystalline and non-epitaxial to the EG²²⁴.

Based on the vacuum level differences extracted from LEER, estimated band alignments across the device contacts are calculated. Figure 5-6b shows a schematic of the band diagram at the contact interface for both EG-MoS₂ and Ti/Au-MoS₂ contacts. The Ti/Au contact is found to have a barrier to electron transport from the metal conduction band to the MoS₂ conduction band of approximately 1.01 eV. The same value for an EG-MoS₂ heterojunction is half of this value, at approximately 0.51 eV. This would suggest that the electron transport across the latter structure is more facilitated, which is in agreement with the electronic characterization in the previous section. Based on this data, it can be assumed the improvement in the contact resistance of the EG-MoS₂

junction stems from the lower barrier to transport across the junction in comparison to the Ti/Au-MoS₂ junction.

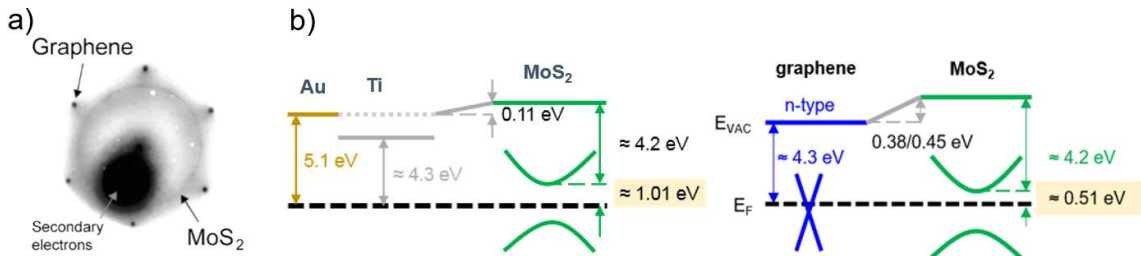


Figure 5-6. a) A LEED image showing the polycrystallinity of MoS₂ and crystallinity of EG in an overlap region. b) A set of band alignment diagrams estimated from LEED values. The electron barrier to transport for the Ti/Au contacted device is twice the height of the EG contacted devices.

5-3-4. Comparison of synthesized and exfoliated epitaxial graphene-MoS₂ heterostructures

While the direct growth method offers scalability in comparison to exfoliated methods in the production of heterostructures, it is also necessary to compare the electronic characteristics of the heterojunctions produced by direct growth and exfoliated methods. To this end, EG-MoS₂ heterostructure devices with MoS₂ exfoliated on EG are fabricated. Figure 5-7a shows a false-coloring image of such devices. It is worth noting that there are several key design differences between the exfoliated and the directly synthesized heterostructure. While the current flow is driven in a single orientation in the directly synthesized devices, the exfoliated devices require current to travel laterally through the EG extensions before travelling longitudinally across the MoS₂ channel such that the current flow is required to turn perpendicularly into the MoS₂ channel. In addition, the EG-MoS₂ vertical contact is longer at ~1 μm in contrast to 50~200 nm in a direct growth sample, and the MoS₂ film in this device is single crystalline rather than the polycrystalline channels of the directly grown structures. While the first point may increase the total device resistance due to current crowding ²²⁵, the latter two points may decrease the device resistance by having a larger transport area and lack of defective grain boundaries. It is unclear how these differences affect the

overall device characteristics, but these devices are still useful for first-order comparisons. Figure 5-7b shows a comparison of the transfer curves for the exfoliated structure and the direct growth devices. The exfoliated heterostructure device has improved device characteristics than the Ti/Au contact device, but it has inferior characteristics compared to direct growth devices. Though the on/off ratio of the exfoliated device reaches the same value as that of the heterostructure at $V_G \cong 2$ V, the turn-on speed is much slower, with a 3 times larger subthreshold swing. While the devices are not directly comparable due to physical device design differences, the transfer curve comparison suggest that the direct growth may offer improved device performance, possibly stemming from the lack of contaminants between the two EG and MoS₂.

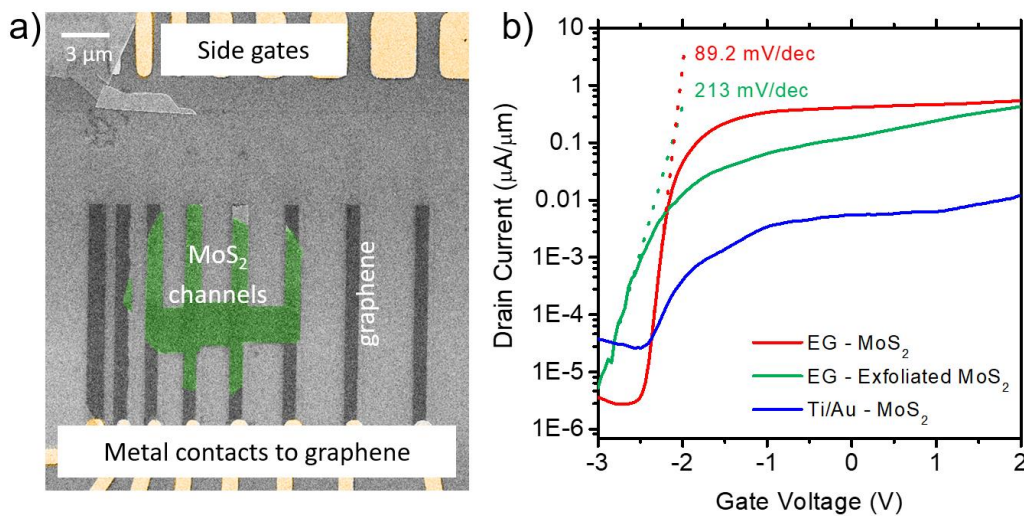


Figure 5-7. a) A false color SEM of the exfoliated EG-MoS₂ FET. The source-drain electrical signal is driven through the metal contacts at the bottom of the image, which extend out to large pads. b) A comparison of the transfer curves for the directly synthesized and exfoliated EG-MoS₂ FETs. The directly synthesized heterostructures exhibit a significantly faster turn-on.

5-4. Summary & future work

In summary, directly synthesized MoS₂-EG heterostructures are used to fabricate type-matched contacts for MoS₂ FETs. In comparison to the more conventional Ti/Au contacts, the

heterostructure junction exhibits more than an order of magnitude reduction in the total contact resistance. In addition, two orders of magnitude improvement in the on/off ratio and three-fold decrease in SS is observed. Based on band alignment estimates calculated from LEER measurements, it is suggested that the electronic transport improvements may be a result of the lower electron barrier to transport. In addition to direct comparisons between the EG and Ti/Au contacted devices, a first-order comparison between devices with directly grown and exfoliated MoS₂ is made. While both devices exhibit a total on/off ratio of 10⁵ over 5 V of gate modulation, the turn-on is much faster for the direct growth devices with a 60% lower subthreshold swing. This suggests the direct growth devices offer advantages in electrical transport in addition to improved scalability.

While this series of experiments focused on as-grown n-type EG, EG is easily tuned to become p-type through intercalation of hydrogen between the buffer layer and the SiC substrate, producing quasi-free-standing epitaxial graphene (QFEG) where the buffer layer no longer exists¹¹⁰. Therefore, this direct growth method for graphene contacts may be extended to p-type TMDs such as WSe₂ as well by utilizing hydrogenated p-type QFEG as electrical contact. In literature, using CVD graphene as contacts for WSe₂ has also shown promise²²⁶; it is suspected that the pristine heterostructure interface of the directly grown heterostructures can offer further improvements in the contact transport of WSe₂ devices. It is suspected that this EG templated growth method to produce graphene contacts to TMDs can be extended to various TMDs by utilizing the tunability of the EG electronic structure to match the band structure of the target TMD.

Chapter 6

Exploration of the Roles of Material and Device design on Sensing Characteristics of MoS₂-Based Chemiresistors

Main subtopic points	w
<ul style="list-style-type: none"> • Approximately 3.5x larger triethylamine sensing signals are observed in powder vaporization-grown MoS₂ chemiresistors on SiC in comparison to MOCVD-grown MoS₂ chemiresistors on sapphire, emphasizing the importance of morphology, stoichiometry, and/or substrate type on the sensing characteristics. • Inducing Mo-O defects in MoS₂ with UV ozone exposure increases triethylamine sensing signal by up to ~30x after 15 minutes of exposure at 1 ppm UV ozone, with a saturation signal over 900%. Further exposure leads to signal degradation, suggesting an optimal defect density for maximizing sensing amplitude. • Exposure of 5.6 at% Nb-doped p-type MoS₂ to triethylamine decreases the channel conductivity, opposite to what is observed for pristine MoS₂, and a ~50x increase in signal-to-noise ratio is observed. The doped MoS₂ sensor exhibits an improved detection resolution, sensing 15 ppb triethylamine in N₂ with a signal-to-noise ratio of ~50. • Ti/Au-contacted MoS₂ chemiresistors exhibit increased sensing amplitude by ~10⁴ and signal-to-noise ratio by ~10^{1.5} in comparison to epitaxial graphene-contacted MoS₂ sensors, suggesting the contact transport plays a direct role in overall sensing. • Direct contributions include device design, post-growth device fabrication, and sensing characterization and analysis. 	

6-1. Introduction

The network integration of various applications able to communicate remotely and function synergistically is becoming more attractive in an increasingly digitized age. These multi-functional network of devices in communication, known as the Internet of Things (IOT), relies on the integration of More-than-Moore functional devices necessary for real-time interaction between the devices and the people or environment around it ^{227,228}. This push is active for military applications as well, where the integration of sensors and actuators is necessary for improved awareness of the field, as illustrated in Figure 6-1a ²²⁹. One avenue of interest is the sensing of triethylamine (TEA),

a pungent chemical irritant and byproduct in the production and decomposition of V-series chemical agents²³⁰, some of which are illustrated in Figure 6-1c. Precise and quick sensing of such components through integrated network of sensors can aid in assessing the field situation to minimize harm to personnel.

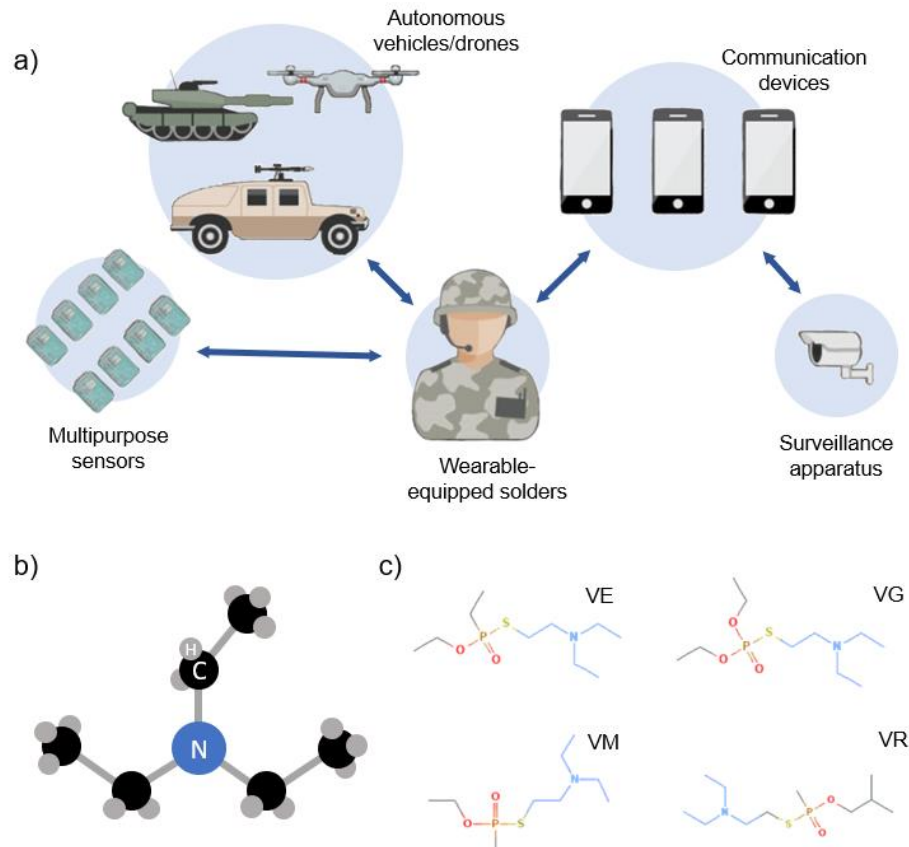


Figure 6-1. a) A schematic of the Internet of Battlefield Things, illustrating the goal of a communication network of soldiers, sensors, vehicles, and other military apparatus (adapted from reference²³¹). b) The molecular structure of TEA. c) The chemical structure of several V-series nerve agents, highlighting the amine functional group in light blue that is isolated after decomposition (adapted from reference²³²).

As discussed in Section 2-3-4, chemiresistors rely on the charge transfer interactions between analyte and sensing material surface. Due to their large surface-to-volume ratio, 2D materials are attractive for sensing applications^{233,234}. Of these materials, MoS₂ is of particular interest for the sensing of TEA^{127,235}. While density functional theory (DFT)-based sensing studies of free-standing MoS₂ suggested the charge transfer between TEA and MoS₂ would be minuscule,

F.K. Perkins et al. reported MoS₂ to be highly sensitive to TEA, with a signal of nearly 20% increase in the conductance after a 10 s exposure in 100 ppm TEA/N₂^{127,236}. This discrepancy was attributed to doping of the MoS₂ by the SiO₂ substrate. However, little is known about sensing of TEA beyond device demonstration. A deeper understanding of the role of material properties, processing techniques, and device design on the MoS₂ sensing of TEA is necessary in order to fabricate reliable sensors optimized for this purpose. In addition, better understanding of how material and external parameters affect TEA sensing can shed light on how such parameters affect TMD chemiresistors in sensing other analytes, paving way for the optimization of TMD chemiresistor fabrication for specific applications.

In assessing the factors that affect TEA sensing signals in MoS₂, it is useful to survey how various parameters affect sensing characteristics in other 2D material, carbon nanotube (CNT) or metal oxide sensors. Treatment of CNTs using ultraviolet ozone (UV O₃) or thermal annealing have been demonstrated to improve sensing of a range of chemicals^{237,238}. This is attributed to the creation of defect sites on the surface of CNTs, which act as additional adsorption and charge transfer sites. Other reports demonstrate improved sensing characteristics by utilizing p-n junctions or Schottky junctions to amplify changes in the electrical transport through the chemiresistor²³⁹⁻²⁴¹. Such devices have been reported for the sensing of TEA as well; J. Du et al. demonstrated the doubling of TEA sensing signals through the addition of NiO particulates on ZnO sheets to produce p-n junctions, as well as improvement in the sensing of other analytes including ethanol and acetone¹²⁴. Additionally, the illumination of MoTe₂ with high-energy UV light has been reported to improve sensing of NH₃, with an improvement in both the signal amplitude and recovery time²⁴². In this case, the suggested mechanism was desorption of oxygen from defect sites, thus increasing the number of interaction sites available for incoming analyte.

Using these reports as basis, a series of studies on the effects of processing conditions and experimental design is performed for the purpose of better understanding the mechanisms of TEA sensing by MoS₂ chemiresistors. First, a demonstration of pristine, untreated MoS₂ chemiresistors

for TEA sensing is performed. Using the sensing results of the untreated devices as a base, the effects of several material, processing technique, and device design parameters on the sensing characteristics is studied. The specific topics studied are the effects of MoS₂ growth process variations, UV O₃ exposure, Nb-doping, contact design, and low-energy illumination.

6-2. Materials and experimental methods

6-2-1. Material growth and device fabrication

Most of the sensing tests are conducted on pristine MOCVD MoS₂ on sapphire substrates, for which the growth process was detailed in Section 3-3-4. Nb is incorporated into the system using NbCl₅ powder heated to 45 °C such that the resulting material is 5.6 at% doped MoS₂, with a fermi level approximately 0.2 eV above the valence band according to Figure 2-9b. After growth, the material is isolated into the device shape and 5/15 nm of Ti/Au is deposited on the material for electrical contact (see Section 3-4). Figure 6-2a shows an optical image of the sensor design. An interdigitated structure where the channel winds through the metal electrodes is used in order to maximize the signal amplitude. The device has 25 interdigitated electrodes for 24 effective channels, each with a width of 800 μm for a total effective channel width of 19.2 mm. The channel lengths range from 3 μm to 15 μm.

In addition to MOCVD MoS₂, EG – PV MoS₂ heterostructures studied in Chapter 5 are used as well. The growth process was detailed in Section 3-3-3. Both EG-contacted and Ti/Au-contacted MoS₂ chemiresistors are fabricated, with an EG contact length of 3~4 μm on each side. “PV MoS₂ devices” in this chapter specifically refer to metal contacted devices where the Ti/Au metal extends beyond the EG and is directly in contact with the MoS₂. Heterostructure devices will be referred to as such, and are PV-MoS₂ based.

For covered-electrode sensors, an additional lithography step is performed after metal contact deposition. SPR3012 is diluted 1:1 with ethyl lactate and spin coated at 4000rpm on the sample to produce a ~600 nm thick photoresist layer. After soft baking at 95 °C for 1 minute, the electrode cover design is exposed to the sample for 0.2 s at a lamp power of 25 mW/cm. After exposure, the sample is developed in CD26 developer for 1 minute to reveal the MoS₂ channels.

6-2-2. Ozone exposure

Some sensors are exposed to ozone prior to sensing measurements. “Weak” UV O₃ is produced using an UVP® Stable ozone generator Model SOG-1 pen light, at a concentration of approximately 1 ppm. “Strong” UV O₃ is produced using an UVOCS® Inc. UV O₃ cleaning system model T10x10 OES, at a concentration of approximately 4 ppm. In both cases, the samples are placed approximately 1 cm below the UV light source. A 5-minute conditioning step prior to the exposure is utilized, but because the O₃ chamber is not air tight and the system must be exposed to ambient to load the target sample after conditioning, the effectiveness of this step on the homogeneity of the subsequent exposure is unclear.

6-2-3. Sensing methods

Triethylamine sensing is performed at NRL with the Sherlock system described in Section 3-5-2. For every device, up to 200 mV peak-to-peak amplitude alternating bias is applied on the device at frequencies around 10 kHz. During simultaneous multi-device measurements, the frequencies are shifted slightly such that the devices are characterized at frequencies between 9.5 kHz to 10.5 kHz. This small shift is to assure that the signals do not resonate. The measurements are automated and is made up of a 300 s stabilization, 10 ~ 600 s exposure time, and 20 ~600 s

recovery time depending on measurement goals. While the total gas flow is constant at 5 lpm of N₂, the concentration of TEA varies per measurement and will be specified per study.

6-3. Results and discussions

6-3-1. Basic device sensing characteristics of MoS₂ chemiresistors

Pristine MOCVD MoS₂ chemiresistors are first characterized as a control for comparison for devices with material and post-processing variations. Figure 6-2a shows an optical image of a MoS₂ sensor. Corresponding XPS data for these growths (previously shown in Figure 2-8 and reproduced in Figure 6-2b) illustrate that the material is of good quality, with a near-ideal stoichiometry of ~1:1.98. Figure 6-2c shows the sensing curve of a 13 μm channel length MOCVD MoS₂ under TEA exposure in white light. The conductance of the signal increases over time when exposed to TEA, and varying the concentration of TEA/N₂ from 10 to 1000 ppm leads to increasing saturation signal amplitudes from 11.2% to 195%. This is expected, as TEA is an electron-donating Lewis base, and increasing electron carriers in n-type MoS₂ in which electrons are the major carrier leads to an increase in the conductivity. In addition, an increase in the concentration increases the equilibrium amount of TEA adsorbed on the MoS₂ channel, thus increasing the saturation signal. Response time ranges from device to device due to non-uniformity during the fabrication process, but low TEA exposures exhibit short response times at around 20-40 seconds, while devices exposed to 100 and 1000 ppm have response times around 50~100 seconds. Figure 6-2d shows pulsed sensing data for the same device, with 10ppm TEA/N₂ exposure of 15 seconds and recovery of 45 seconds. The output appears to increase both in the peak signal and recovered signal. The increase in the “off-state” signal is likely due to the device requiring longer times to fully recover, such that the device has not fully recovered from a TEA pulse before being exposed to the next pulse. The increase in the peak signal from ~2.5% at the first pulse to ~4.5% at the 10th pulse is

partially due to the higher baseline “off-state” signal. The $\Delta\%$ from peak to valley varies between 2.0 ~3.2%, and appears to be increasing with more pulses; however, the trend is not clear and is inconclusive. Increasing signal $\Delta\%$ could be due to low concentration of adsorbed oxygen atoms being removed from the surface as the device ambient environment changes.

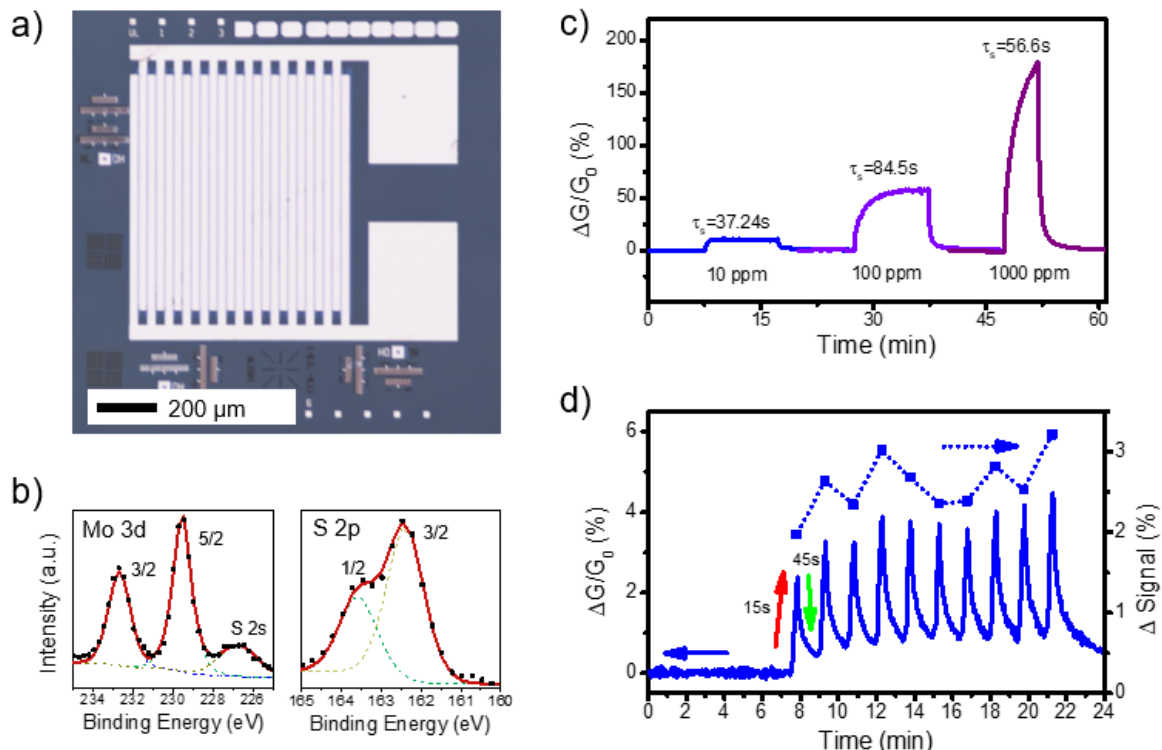


Figure 6-2. a) Optical image of an MOCVD MoS₂ device, showing the interdigitated structure. b) XPS of the Mo 3d and S 2p peaks of MOCVD grown MoS₂. The Mo:S ratio is ~1:1.98. c) The sensing characteristics of MoS₂ devices over increasing concentrations of TEA. The response time listed corresponds to these specific curves and are not averaged representation of a number of devices. d) Pulsed sensing characteristic of the same device in (c) at 10 ppm pulsed for 15 s with 45 s recovery. The peak-to-valley signal difference for each pulse is also plotted.

In order to confirm the signal is due to the presence of triethylamine, the sensors are exposed to pure N₂ pulses. Figure 6-3a shows the sensor output over several pulses of N₂ at 5 lpm, denoted in gray. No observable signal is detected, indicating the sensor does not respond at detectable levels to N₂ or small pressure changes associated with the introduction of gas flow above the sensor. In addition, selectivity of the sensor is tested by exposing the devices to o-nitrotoluene (o-NTol), to which MoS₂ has been reported to be unresponsive ¹²⁷. Figure 6-3b shows the sensor

output over time as 3 ppm o-NTol is introduced to the system. No observable signal is detected, corroborating the selectivity of MoS₂ to triethylamine as reported in literature. According to the basic sensing characteristics of MoS₂ exposed to TEA, N₂, and o-NTol, the devices perform in expected ways with sensing characteristics that are on the same order as what has been reported in literature; the remainder of the chapter focuses on how sensing characteristics evolve with various changes to the material, device design, and experimental setup.

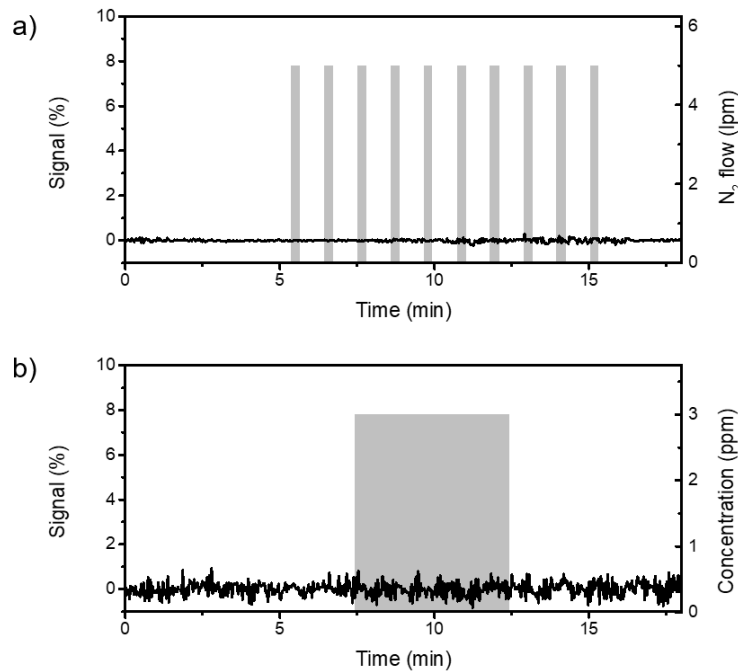


Figure 6-3. a) Sensor signal over time through ten 30 second pulses of pure N₂ at 5 lpm flow. b) Sensor signal over time through a single 5 minute pulse of 3 ppm o-NTol in N₂. In both a) and b), no detectable sensor signal is observed.

6-3-2. Effect of growth process on sensing characteristics

The difference in the Mo:S ratio of the PV and MOCVD growth MoS₂ films was discussed in Section 2-2-2. The MOCVD growth process produces more stoichiometric MoS₂ than PV, with PV films having an estimated 10% more vacancies roughly based on the Mo:S ratio. The sensing curves of a 9 μm channel length PV MoS₂ device and an MOCVD MoS₂ device under 100 ppm of

TEA/N₂ is plotted in Figure 6-4a. PV grown devices exhibit higher signal amplitudes, with a saturation signal difference of approximately 3.5x. Based on a survey of additional PV and MOCVD grown devices, it is found that this trend of higher sensing signals from PV devices is consistent, as PV devices consistently sense at saturation amplitudes of approximately 400~500%, while MOCVD samples sense in a range of 50 ~ 150%, depending on the device. While this could suggest the improvement in sensing amplitude due to the increased vacancies in PV grown MoS₂, it is critical to note that these films differ in ways beyond stoichiometry; According to SEM images shown in Figure 6-4b, the MOCVD films have smaller, < 1 μm domain sizes compared to PV films with domains ranging from 1-3μm, and PV films are multi-layered at the domain centers due to additional nucleation while MOCVD devices remain mostly monolayer with bilayer regions where domains overlap. Furthermore, it has been suggested that the substrate plays a large effect on the sensing characteristics of the TMD film through doping of the film above it ²³⁶. The convoluted effects of the substrate doping effect and growth differences due to growth process and substrate is not well understood, but it is expected to have a direct effect on the sensing characteristics.

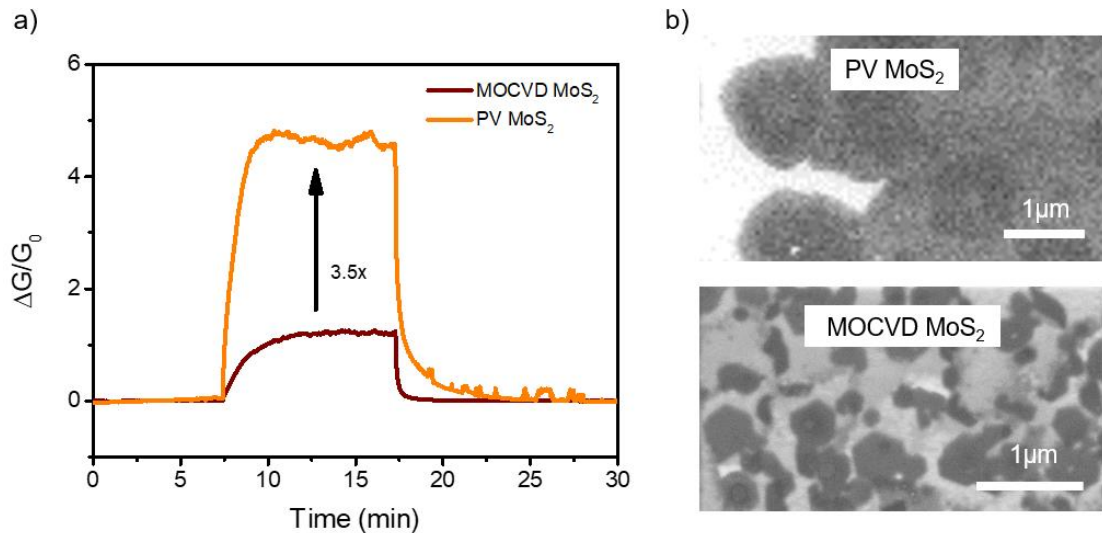


Figure 6-4. a) A representative comparison between a PV and MOCVD grown MoS₂ film under 100 ppm TEA/N₂ exposure. the PV grown film exhibits a 3.5x increase in the saturation signal. b) SEM images of PV and MOCVD grown films. The PV domains are larger and thicker, while the MOCVD growths are smaller but have more controlled layer numbers.

6-3-3. Effect of controlled defects on sensing characteristics: ozone exposure

The characteristics of MoS₂ sensors as a function of ozone exposure is studied to see how induced defects change the charge transport interaction of MOCVD MoS₂ and TEA. Prior to the characterization of UV O₃ exposed sensors, the effect of UV O₃ on MOCVD MoS₂ is quantified. XPS of the sulfur 2p bonds for a pristine MOCVD MoS₂ sample before and after exposure to UV O₃ is plotted in Figure 6-5a. As-grown XPS data show no observable Mo-O bonds, with a S:Mo ratio of ~1.97:1. After 10 minutes in ~4 ppm UV O₃, XPS peaks corresponding to S-Mo-O bonds are observed. The S:Mo ratio calculated from XPS data as a function of ozone exposure time is plotted in Figure 6-5b. The plot shows that as the ozone exposure is increased, the S:Mo ratio is reduced, stabilizing at 1:0.94 after 10 minutes of exposure. Numerically, this could correlate to the Janus structure MoOS, with the top chalcogen layer of MoS₂ films becoming completely replaced with oxygen, leaving behind only the sulfur layer underneath the Mo as illustrated in Figure 6-5c²⁴³. However, this will require additional material characterization to confirm.

Based on XPS data, longer UV O₃ exposure results in a higher density of surface defects in the channel; the effect of this change in sensing characteristics is studied. Figure 6-5d shows the saturation signal as a function of ~1 ppm UV O₃ exposure for both PV and MOCVD MOS₂ devices under exposure to 100 ppm of TEA/N₂. For the first 15 minutes, there is an increase in the saturation signal for both types of devices, up to over 900% at 15 minutes for MOCVD, more than an order of magnitude increase from as-grown at ~30%. However, the saturation signal for MOCVD devices are observed to have decreased after 25 minutes of UV O₃ exposure, possibly due to degradation of the material and thus the sensing characteristics. This trend is mirrored in the S/N values plotted for the MOCVD devices in the inset in Figure 6-5d, with the S/N ratio increasing to ~3000x in comparison to ~20x prior to ozone sensing. Based on this data, it is likely that there is an optimal density of Mo-O bonds on the MoS₂ surface at which the device is most sensitive, above which the effects of degradation on the material become larger than the improvement in sensing

characteristics. While previous reports of UV O₃ treated, chemically exfoliated, multi-layer MoS₂ suggests the sensing is due to the creation of a layer of MoO₃ and thus a MoO₃:MoS₂ heterojunction that assists hole injection into the MoS₂²⁴⁴, the MoS₂ utilized in this study is approximately 70% monolayer, making heterojunction area relatively low. It is likely that the Mo-O bonds themselves act as additional charge injection sites in addition to the effects of the MoO₃:MoS₂ heterojunction.

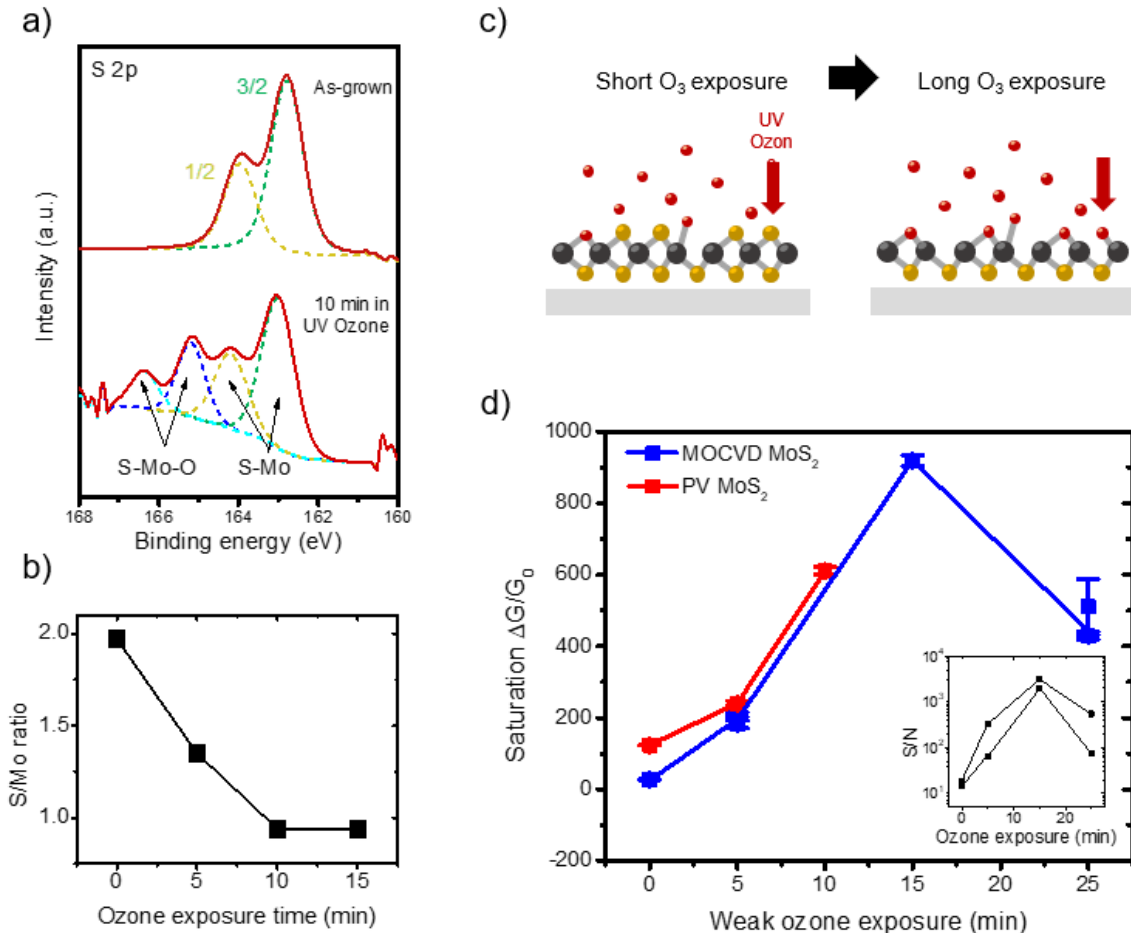


Figure 6-5. a) XPS data for the S 2p peak of a MOCVD MoS₂ sample before and after 10 minutes in ~4 ppm UV O₃ exposure. After the exposure, peaks corresponding to S-Mo-O bonds are observed. b) A calculation of S to Mo concentration for increasing ozone exposure times. The ratio stabilizes at approximately 0.94 above 10 min of exposure. c) An illustration of MoS₂ after exposure to UV O₃ where the top sulfur layer has been removed and replaced with O and vacancies to produce a MoOS Janus structure. d) The saturation signal of MOCVD and PV MoS₂ sensors as a function of ~1 ppm UV O₃ exposure time. Both devices exhibit a similar increase in sensing, and a peak in the saturation is observed for MOCVD devices at 15 minutes. The inset shows the S/N ratio of the MOCVD sensing curves, which mirror the trend seen in the saturation signal.

While some of the Mo-S bonds at the top surface of the MoS₂ growths are converted to Mo-O, it is likely that the ozone treatment leads to the formation of additional sulfur vacancies as well. Comparisons based solely on vacancy concentrations is difficult to make between the PV and MOCVD grown devices due to factors discussed in the previous section. However, a rough estimate of the maximum increase in sensitivity with vacancies is made using the 3.5x increase from MOCVD to PV for ~10% vacancy increase. Assuming each vacancy site interacts identically and independently, having 50% vacancies where every sulfur on the MoS₂ surface has been removed would lead to ~17x increase in the signal. While this assumption ignores the likely degradation of sensing characteristics due to material degradation, this still falls short of the ~50x increase in signal observed after ozone treatment. Based on this, it is possible the increase in sensing in the UV O₃ exposed samples is due to the creation of Mo-O bonds and S vacancy sites, both of which contribute to sensing at varying degrees. However, due to the convolution of various growth-based differences between PV and MOCVD grown devices, this is solely a rough estimate and requires further studies.

6-3-4. Effect of controlled defects on sensing characteristics: Nb-doping

In addition to defects introduced post-growth, the effect of external dopants introduced during growth is studied, specifically the effect of p-type Nb dopants. Figure 6-6a shows SEM images of the undoped and 5.6 at% Nb doped MoS₂ device channels. A difference in the growth morphology is observed, with the Nb doped MoS₂ samples showing some vertical growth, aligned to the underlying MoS₂. XPS near the valence band edge (Figure 6-6b) reveal that the 5.6 at% doped material has a fermi level that lies at approximately 0.2 eV above the valence band, confirming that the material is heavily p-type doped, but not degenerate. Representative current-voltage curves of the pristine and doped devices are plotted in Figure 6-6c in log-scale for facile comparison. The doped devices are approximately 1000x more conductive, with a total device

resistance of $0.0037 \text{ k}\Omega/\mu\text{m}$ in comparison to $5.24 \text{ k}\Omega/\mu\text{m}$ for the pristine MoS₂ devices. This could be indicative of an increase in major charge carrier concentration, and suggests that there are significantly more hole carriers in the doped samples than there are electrons in the pristine sample.

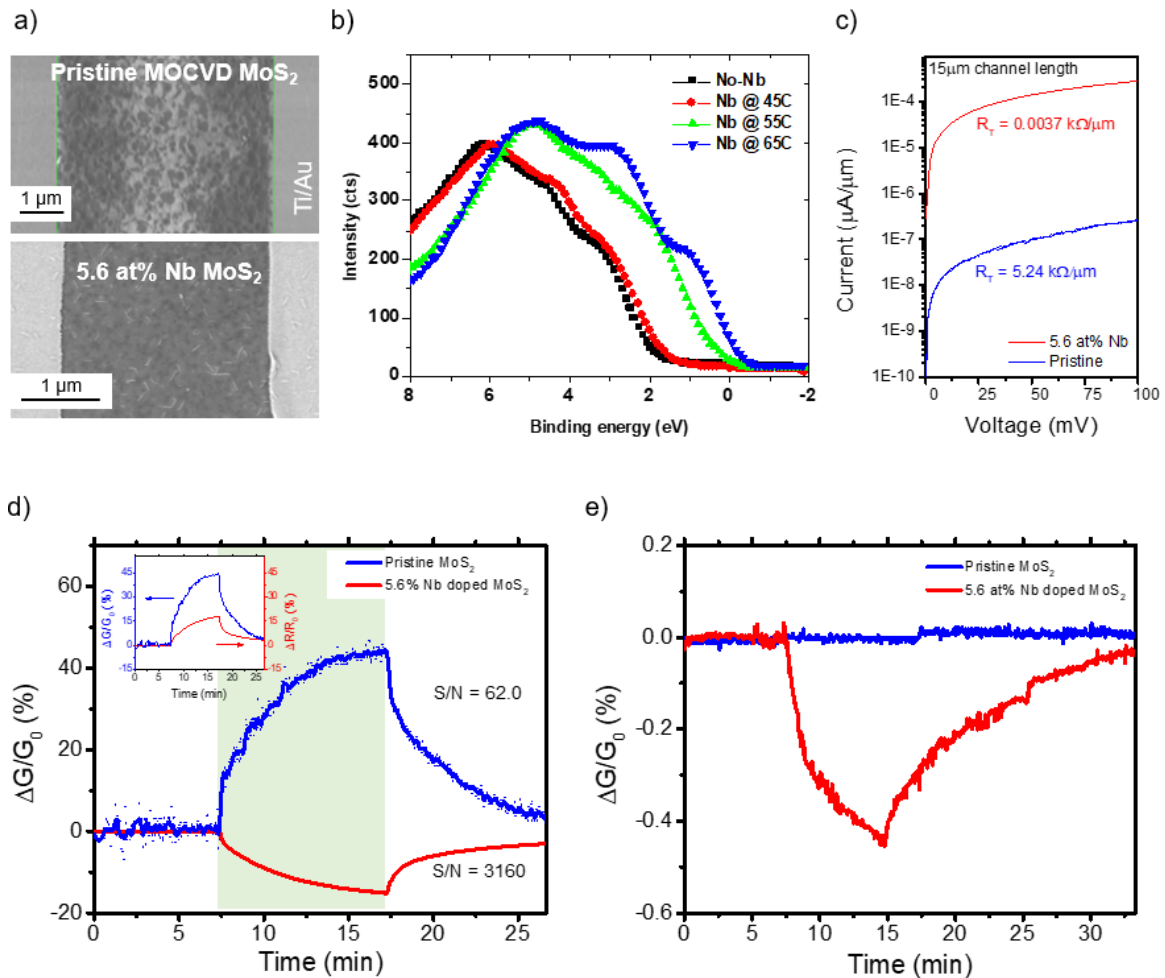


Figure 6-6. a) SEM images of MOCVD MoS₂ sensor channels for pristine and 5.6 at% MoS₂ films contacted by Ti/Au metal electrodes. b) XPS data near the valence band edge of MoS₂. The fermi level shifts closer to the valence band edge at higher doping concentrations (K. Zhang, in preparation). c) Current voltage characteristics for pristine and 5.6 at% Nb MoS₂ devices. The latter is approximately three orders of magnitude more conductive. d) Sensing characteristics of pristine and 5.6 at% Nb MoS₂ sensors in 100 ppm TEA/N₂. While the pristine MoS₂ exhibits an increase in signal with analyte exposure, 5.6 at% Nb doped MoS₂ exhibits a decrease in the conductance. e) Sensing characteristics of pristine and 5.6 at% Nb MoS₂ sensors in 15ppb TEA/N₂. While no signal is observed for pristine devices, a signal 50 x above noise level is observed for the doped devices.

Characterization of these sensors under TEA exposure reveal that the two devices exhibit significant differences. Figure 6-6d shows a direct comparison of the sensing characteristics of pristine and 5.6 at% Nb doped MoS₂ devices under exposure to 100ppm TEA/N₂, marked in green. Contrary to the sensing characteristics of n-type pristine MoS₂, the Nb-doped devices are observed to exhibit a decrease in the conductance with TEA. This is indicative of holes being the major carrier in the material, as suggested by the band energy diagram; in this case, the injection of electrons by TEA leads to an overall decrease in the hole concentration through electron-hole recombination, thus decreasing the total conductance of the film. While the total sensing signal is smaller for the Nb-doped MoS₂ compared to the pristine MoS₂, the signal is significantly less noisy. The smaller magnitude of the signal is a result of the large initial conductance of the doped samples as shown in Figure 6-6c, such that the signal, which is simply the normalized change in conductance, becomes small. In cases where the initial conductance of the material is significantly different, it is more informative to calculate a signal to noise ratio S/N as discussed in Section 2-3-2. The S/N for these pristine MoS₂ materials are found to be approximately 40 ~ 60, while the S/N of Nb-doped devices are around 3000. Based on this metric, the doped MoS₂ devices are approximately 60 times more sensitive relative to its noise level than pristine MoS₂.

This is confirmed by low TEA concentration measurements. In this case, both pristine and doped devices are exposed to approximately 15 ppb TEA/N₂, and the resulting sensing signals are plotted in Figure 6-6e. While the pristine sensor shows no discernable signal to the TEA exposure, the doped device shows a clear signal with a S/N ratio of ~50, far beyond the 3x noise threshold. Based on this data, it can be concluded that doping the MoS₂ film with Nb leads to an improvement in the sensing resolution of the device, even though the normalized sensing signal is decreased due to the high initial conductance of the Nb doped film. While only one doping concentration of MoS₂ was studied in this test, studying the sensing characteristics as a function of Nb-dopant concentration may reveal a trend that could be used in tuning the characteristics to target an ideal compromise between high resolution and high signal amplitude of the MoS₂ sensor.

6-3-5. Effect of contact material on sensing characteristics

In Chapter 5, direct synthesis of EG contacts to MoS₂ devices were studied, and a significant improvement in the device transport in comparison to conventional metal-contacted devices were observed. Here, a direct comparison is made between chemiresistors with these two types of contact structures. As the growth and processing of these structures are unchanged, characterization of these structures will not be repeated in this section; refer to Chapter 5 for such results. Figure 6-7a shows a schematic of the two types of devices as well as a graphene channel device. A direct comparison of the signal amplitude of 5 μm PV synthesized MoS₂ sensors with Ti/Au and EG contacts under exposure to 100ppm of TEA/N₂ is plotted in log scale in Figure 6-7b. A device with a 5 μm graphene channel length is also plotted; this device is non-responsive to the TEA. This confirms that the graphene itself do not contribute to the sensing signal of the MoS₂ devices. At first glance, there is a large difference of 4 orders of magnitude in the saturation signal of the MoS₂ devices with a saturation signal amplitude of ~480% for the Ti/Au device and ~0.07% for graphene devices. However, as was the case for Nb-doped MoS₂ samples, the enormous difference in the sensing amplitudes partially stems from the larger initial conductance of the EG-MoS₂ devices, reported in Chapter 5. The total device resistance of each sensor device in this case is noted in the plot. Instead, the on/off ratio is marked in Figure 6-7b as a more informative parameter to compare. It is observed that the on/off ratio of Ti/Au is still higher at nearly 3 orders of magnitude, compared to the on/off ratio of EG devices at approximately 1.5 orders of magnitude. The S/N ratio for the heterostructure devices is ~23.8, while the same metric is approximately 20 times larger at ~514 for the Ti/Au-contacted devices. These trends suggest that devices with Ti/Au contacts with larger transport barriers to MoS₂ (discussed in Section 5-3-3) exhibit improved sensor device performance in comparison to EG-contacted devices. This trend is the opposite of what was observed in the case of gated FETs.

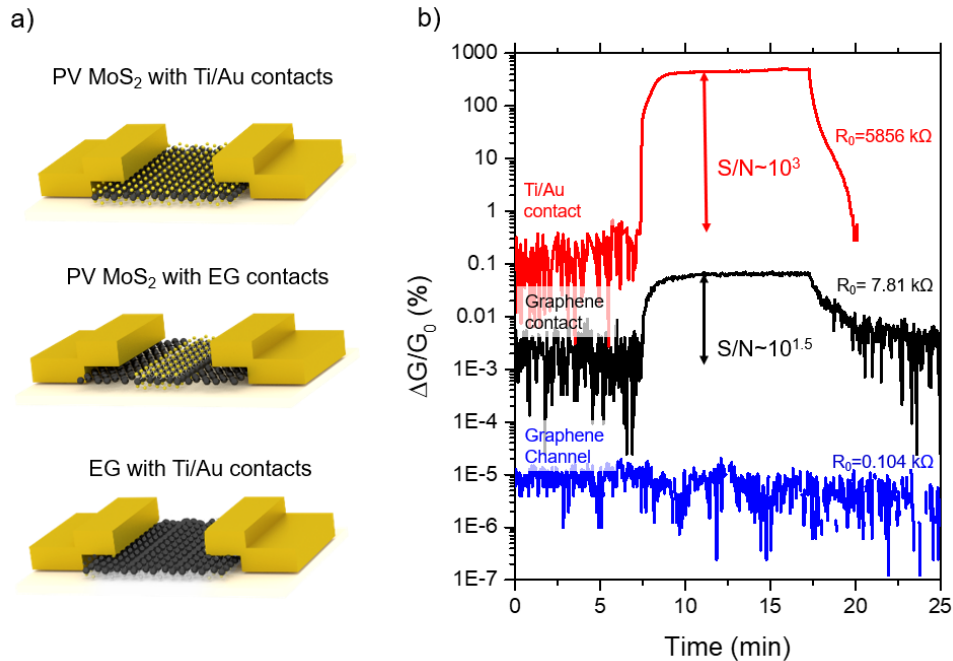


Figure 6-7. a) A series of schematics of devices with MoS_2 channel and Ti/Au contacts, MoS_2 channel with EG contacts, and EG channel with Ti/Au contacts. b) The sensing characteristics of the three types of devices under exposure of 100 ppm TEA/ N_2 , plotted in log scale for easier comparison. The graphene channel does not exhibit any sensing, while the Ti/Au-contacted devices exhibit higher overall signal and S/N in comparison to EG-contacted devices.

Other sensors with an increase in sensing signal with a high barrier junction have been reported in the past. While some reports suggest an actual change in the SB height with analyte exposure²⁴¹, it is more likely that the improvement in signal stems from an increase in thermionic field emission across the junction. Under the exposure of electron donating analytes such as TEA, the major carrier concentration in MoS_2 increases and leads to a thinning of the depletion width through Eq. 2-5. This decrease in the barrier width leads to an increase in the thermionic field emission across the SB, as discussed in Section 2-3-2. This increase in transport through the thinning of the SB, compounded with the increase in channel conductivity due to the analyte, may be the source of the increased sensing signal observed for Ti/Au-contacted devices.

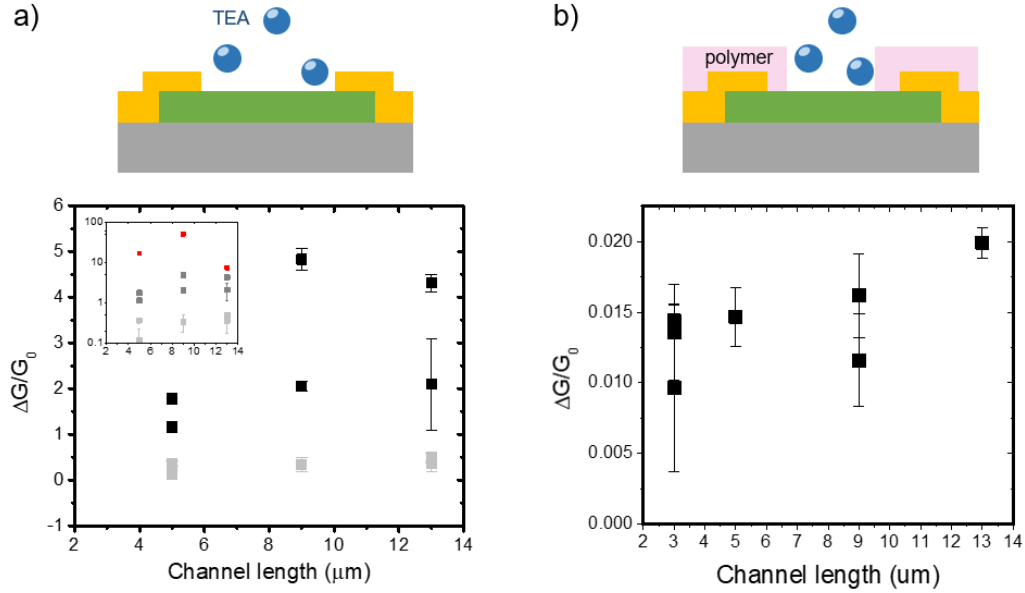


Figure 6-8. a) A cross sectional schematic of MOCVD MoS₂ devices and the corresponding saturation signal as a function of channel length for devices exposed to 10 ppm (light gray), 100ppm (black), and 1000ppm (red). The inset shows the same data on a log plot. b) A cross sectional schematic of a polymer covered MOCVD MoS₂ device and the corresponding saturation signal as a function of channel length for 1000ppm exposure.

In order to test this theory, a series of sensing characteristics as a function of channel length is studied. Based on Eq 2-5, increase in channel carrier concentration leads to further decrease in the SB width. This suggests that as the concentration of TEA/N₂ is increased from 10ppm to 1000 ppm, the SB width shrinks further, thermionic field emission increases, and the contact resistance of the device is decreased. Figure 6-8a shows a plot of saturation amplitude for various analyte concentrations as a function of channel length. While a positive correlation is observed under exposure to 10 ppm TEA/N₂, shown in light gray data points, the data becomes scattered for 100 ppm TEA/N₂, shown in black data points, and at 1000ppm the data becomes further scattered as illustrated by the red data points in the logarithmic scale inset. In addition, a series of devices with a polymer cover layer are fabricated in an effort to independently study the sensing of the MoS₂ channel from the modulation of the SB at the contact edge. The polymer layer is 600nm thick and extends 500nm into the channel beyond the contact on both sides of the channel. This data is presented in Figure 6-8b. While an apparent positive correlation between sensing signal and device

channel length is observed, the low signal amplitude values and large error bars corresponding to noisy data prevent any clear conclusions from being made. The significantly low signal amplitudes is suspected to be due to polymer residue on the surface of the MoS₂ channel that is more prevalent after photoresist develop without a polymer clean. It is expected that some of this residue is more thoroughly cleaned with the full photoresist cleaning done for devices with no polymer cover layers. While the data shown in Figure 6-8 is inconclusive, improvements in the experimental procedures, such as larger data sets and non-polymer contact covers can be used to further study the effect of contact modulation on the sensing characteristics of MoS₂ sensors.

6-3-6. Effect of low-energy illumination on sensing characteristics

Thus far, the sensing characteristics discussed have been taken under exposure to the experimental system's tungsten halogen microscope light. In this chapter, the effect of such low energy light is discussed. Figure 6-9a illustrates the signal amplitude of a 13 μm channel length MOCVD sensor taken at varying concentrations of TEA/N₂ with and without the lamp illumination. An increase of up to 2x in the amplitude is observed at 1000 ppm. While this improvement in the signal is modest in comparison to other effects discussed earlier in this chapter, the improvement is observed at every concentration level, with apparently increasing effects at higher concentrations. While such improvements in sensing have been observed with UV light exposure, the suggested mechanism has been the increase in available sensing locations through desorption of O₂ from the TMD surface with UV light ^{245,128}. However, the system setup used in this work utilizes a low energy lamp with a wavelength spectrum centered around near-infrared, as plotted in Figure 6-9b. The binding energy of oxygen in a sulfur vacancy is reported to be ~2.4 eV ²¹⁵, equivalent to 517 nm wavelength light, for which the radiant flux is relatively small for the tungsten halogen lamp. While it is suspected some desorption of oxygen can occur with the current system, it is likely the increase in sensing signal is partially due to another mechanism. One possibility is the improved

mobility of the major carriers due to the increasing carrier concentration with visible light exposure on MoS₂^{246,247}. With increased carrier concentration in the channel, coulomb impurities at the surface of the MoS₂, such as adsorbed charged TEA molecules, may be more efficiently screened. This reduces scattering of charge carriers through the channel, improving the charge mobility and thus the total conductivity. While this is speculation based on experimental observations, it has been suggested that an increase in carrier concentration more effectively screens coulomb impurities in graphene²⁴⁸; this concept may be applicable to TMDs as well. Based on the results in Figure 6-9a, it can be stated that performing sensing measurements under the exposure of visible light can directly affect the sensing characteristics; while this is something that is necessary to keep in mind when analyzing such measurements, it can also be utilized to improve sensing characteristics in consumer applications.

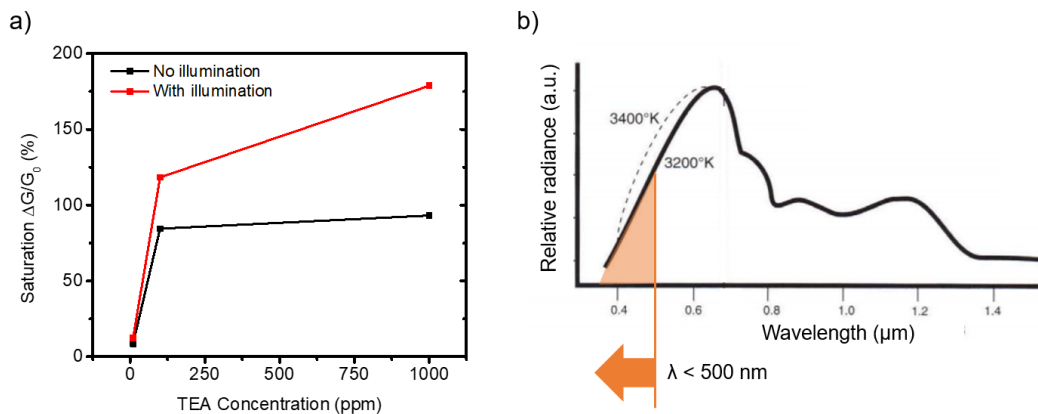


Figure 6-9. a) Saturation signal of 13 μm MOCVD MoS₂ sensors as a function of TEA concentration with and without microscope lamp illumination. b) The spectrum of the halogen lamp used in Sherlock. Wavelengths strong enough to desorb O₂ is marked (adapted from reference²⁴⁹).

6-4. Summary & future work

In summary, various methods of improving the sensing amplitude and sensitivity of MoS₂ chemiresistors for detection of TEA was explored. First, pristine MOCVD-grown MoS₂ was tested as a baseline to which subsequent experiments were compared to. While device-to-device variation

can be observed, these devices perform as expected based on theory and previous literature on MoS₂-based sensors for TEA. These devices were also compared to PV-grown MoS₂, where it was observed that PV-grown films consistently exhibit higher signals compared to MOCVD growth devices (within an order of magnitude). This difference is likely due to a combination of difference in vacancy concentration, morphology, and substrate between the two films.

To study the effects of controlled defects, MoS₂ sensors with UV O₃ exposure and impurity doping is characterized. Exposure to UV O₃ created Mo-O bonds on the MoS₂ surface according to XPS data, and exhibited a maximum observed signal amplitude of ~1000% after 15 minutes in ~1 ppm TEA/N₂. However, the existence of an optimal defect density is observed, as further UV O₃ exposure lead to a degradation in the sensing signal. Heavily p-type Nb-doped MoS₂ is observed to react in the opposite sensing magnitude compared to pristine n-type materials. While the sensing amplitude of the Nb-doped MoS₂ was smaller than that of pristine MoS₂, it is observed to have improved resolution and is able to detect 15 ppb TEA with S/N ratio of ~50.

In addition to defects, the effect of device and measurement design was studied. Utilizing higher Schottky barrier contacts of Ti/Au to MoS₂ rather than EG is observed to have an improved saturation signal of ~480% in comparison to ~0.07%, as well as improved S/N ratio by ~20x. It is suggested that the charge transfer doping of TEA leads to a thinning of the SB at the Ti/Au contact, thus an increase in the thermionic field emission. It is expected this effect is larger in the Ti/Au contact rather than the EG contact, such that the compounded sensor signal increase is larger in the former device. Finally, it is observed that low-energy light from the system microscope manifests in a modest (~2x) but clear improvement in the sensing characteristics of the MoS₂ channel. Due to the low energy of the light, it is suspected that mechanisms other than oxygen desorption is at play; the improvement in carrier mobility due to improved screening of coulomb impurities at the surface is suggested.

In order to assess MoS₂ chemiresistors, a basic comparison to other TEA sensors are necessary. The sensing characteristics of various sensors reported in literature is compared to the

devices in this work in Table 6-1. While many oxide-based devices exhibit larger signals than MoS₂ sensors in this work and in literature, oxide-based sensors operate above room temperature, and low concentration (on the order of 10 ppb) detection of TEA has not been demonstrated²⁵⁰. This suggests MoS₂ chemiresistors are advantageous for applications requiring room temperature operation or low concentration detection.

Table 6-1. Comparison of triethylamine sensors in literature (top half) to the sensors in this work (bottom half). While some literature report higher signals, sensors in this work perform at room temperature, and exhibit promise for signal and detection limit improvements. Detection limits listed in () specifies the minimum tested concentration.

SENSOR TYPE	T (°C)	[X] (ppm)	SIGNAL ($\Delta G/G_0$, $\Delta R/R_0$ %)	DETECTION LIMIT (PPM)
ZNO MICROPYRAMIDS CHEMIRESISTOR ²⁵¹	300	100	6600%	(< 2)
TIO ₂ NANORODS CHEMIRESISTOR ²⁵²	290	100	1320%	(< 0.1)
SNO ₂ /ZN ₂ SNO ₄ HETEROJUNCTION SENSOR ²⁵³	250	100	4700%	(< 0.5)
A-MOO ₃ FLOWER CHEMIRESISTOR ²⁵⁴	250	100	316%	(< 0.5)
ZNO/SNO ₂ HETEROJUNCTION SENSOR ²⁵⁵	40	100	1470%	(< 2)
POLYPYRROLE/WO ₃ PN-JUNCTION SENSOR ²⁵⁰	RT	100	680%	~ 5.4
EXFOLIATED MOS ₂ CHEMIRESISTOR ¹²⁷	RT	100	~17% at 15s	0.01
MOCVD MOS ₂ CHEMIRESISTOR	RT	100	50~150%	(< 10)
PV MOS ₂	RT	100	300~500%	(< 10)
MOCVD MOS ₂ (AFTER 1PPM UV O ₃ FOR 15 MIN)	RT	100	919%	(< 10)
5.6 AT% NB DOPED MOCVD MOS ₂	RT	100	17%	(< 0.015)

While various routes to modify the sensing of TEA by MoS₂ is discussed, there is still much to be understood on the exact mechanisms of such changes. For example, the convolution of growth morphology and stoichiometry with substrate effects on the sensing characteristics was discussed in Section 6-3-2. To deconvolute the data, the sensing of identical material on various substrates can be studied by utilizing material transfer after growth or exfoliation. In addition, the effect of the substrate-film interaction can be studied by comparing sensing characteristics of identical growths where a film is transferred to a new substrate of the same material.

In addition to the deconvolution of substrate and growth process effects, the effect of the contact requires further studies. While the data presented in this thesis was inconclusive, changes to the experimental methods, as discussed in section 6-3-5, may shed light on the modulation of the current transport across the SB and the resulting effect on the sensing characteristics. This will assist in utilizing the best materials for contacting MoS₂ sensors.

Chapter 7

Dissertation Summary

In this dissertation, a series of studies focusing on the integration and processing of 2D TMD based electronic devices are studied for the purpose of better understanding the manipulation of 2D TMDs for More-than-Moore applications. This chapter will provide a summary of the results and discussions of the research presented in earlier chapters.

The dielectrophoretic assembly of microns-sized monolayer WS₂ and MoS₂ on simple, parallel electrodes is demonstrated with no damage to materials based on optical characterization. In addition, a positioning torque is observed to act on triangular particles, likely driven by the minimization of potential energy of an assembling triangle. Further tuning of the assembly structure may help achieve high density, precisely assembled arrays of 2D materials. In addition, theoretical calculations suggest that sequential assembly may be possible through tuning of the assembly structure and parameters. Further studies could lead to controlled, large-area positioning of 2D materials on underlying circuitry or fabrication of 2D heterostructures.

While exfoliated graphene-TMD heterostructures have been used as an intermediate contact between metal and the TMD, a direct-growth approach to lateral EG-based heterostructures is demonstrated as a scalable alternative to exfoliation techniques. Characterization of the resulting films confirm the successful growth of spatially lateral EG-MoS₂ heterostructures, with negligible MoS₂ growth on the surface of EG and a short, sub-micron pristine vertical overlap at the interface. Utilizing these structures as EG contacts to MoS₂ devices lead to a ~20x decrease in the contact resistance compared to Ti/Au-contacted MoS₂. In addition, an increase in the FET performance of an MoS₂ channel device is observed, with a 70% reduction in the subthreshold swing and 2 orders of magnitude increase in the on/off ratio. Comparison of the direct-growth heterostructure devices to exfoliated heterostructures reveal that the exfoliated heterostructures have an inferior subthreshold swing ~2.5x larger than the direct-growth heterostructures, suggesting the importance

of a contaminant-free, pristine heterojunction interface. It is envisaged that this method can be extended to other TMDs by utilizing hydrogenated p-type EG.

In addition to studying MoS₂ channel FETs, MoS₂ channel sensors for the detection of TEA are tested with various material and processing conditions. It is observed that many factors played a large role in the sensing characteristics, including surface defect concentration, doping effects, contact design, and low energy illumination. PV-growth based MoS₂ channels output consistently higher sensing signals in comparison to MOCVD-growth based channels, expected to be due to a combination of larger vacancy concentration in PV films, differences in morphology, and substrate doping effects. Inducing Mo-O bonds on the MoS₂ surface through UV O₃ exposure was found to increase the sensing signal by up to ~30x after 15 minutes in 1 ppm UV O₃. Introducing Nb dopants in the MoS₂ film flipped the sensing magnitude of the film from increasing conductivity to decreasing conductivity with TEA exposure, but exhibited an improved resolution, sensing 15 ppb TEA/N₂ with a S/N ratio of ~50. Utilizing EG-MoS₂ heterostructures to compare to Ti/Au contacted devices reveal that Ti/Au sensors exhibited higher signal amplitude by ~4 orders of magnitude as well as higher S/N ratio of ~20x. This is expected to be due to larger increase in transport at the contact due to a thinning of the SB for Ti/Au contacted devices; however, the effects of sensing concentration on the contact requires further studies. While many factors to MoS₂ sensing characteristics are discussed, deconvolution of these factors and deeper understanding of the effect of material parameters on the sensing characteristics is necessary; it is of interest to continue to study these effects in order to understand the exact mechanism of sensing for TMD chemiresistors.

The above results bring some light to the large roles that material properties, fabrication design and processes, and post-fabrication processes play on the characteristics of TMD devices. It is expected that these discussions may be helpful in further understanding the topics of material integration, contact engineering in FETs, and characteristics of TMD-based sensors. In moving forward, these results can be utilized to facilitate integration of TMDs into More-than-Moore

electronic systems as well as improving TMD device quality for various applications by understanding the effect of material properties on the device characteristics.

References

1. Statista. Semiconductor sales revenue worldwide from 1987 to 2019. (2018). Available at: <https://www.statista.com/statistics/266973/global-semiconductor-sales-since-1988/>.
2. Heywang, W. & Zaininger, K. H. Silicon: the Semiconductor Material. in *Silicon* (eds. Siffert, P. & Krimmel, E. F.) 25–42 (Springer, Berlin, Heidelberg, 2004).
3. Streetman, B. E. N. G. & Banerjee, S. K. *Solid State Electronic Devices*. (Prentice-Hall, 2006).
4. Arden, W. *et al.* ‘More-than-Moore’: White Paper. *Int. Technol. Roadmap Semicond.* (2010).
5. Ha, D., Yang, C., Lee, J. & Lee, S. Highly manufacturable 7nm FinFET technology featuring EUV lithography for low power and high performance applications. *2017 Symp. VLSI Technol.* (2017).
6. *Nano-Electronic Devices*. (Springer).
7. Frank, D. J. *et al.* Device Scaling Limits of Si MOSFETs and Their Application Dependencies. **89**, (2001).
8. Mistry, K. *et al.* A 45nm Logic Technology with High-k + Metal Gate Transistors , Strained Silicon , 9 Cu Interconnect Layers , 193nm Dry Patterning , and 100 % Pb-free Packaging A 45nm Logic Technology with High-k + Metal Gate Transistors , Strained Silicon , 9 Cu Intercon. (2008). doi:10.1109/IEDM.2007.4418914
9. Hisamoto, D., Lee, W., Kedzierski, J., Takeuchi, H. & Asano, K. FinFET — A Self-Aligned Double-Gate MOSFET. (2001). doi:10.1109/16.887014
10. Roser, M. & Ritchie, H. *Technological Progress*. (2018).
11. Waldrop, M. M. MORE THAN Moore. *Nature* **530**, (2016).
12. Walsh, D. & Solymar, L. *Electrical Properties of Materials , Seventh Edition*. **2004**, (Oxford University Press, 2004).

13. Novoselov, K. S., Mishchenko, A., Carvalho, A. & Castro Neto, A. H. 2D materials and van der Waals heterostructures. *Science (80-.)*. **353**, (2016).
14. Avouris, P. Graphene: Electronic and Photonic Properties and Devices. *Nano Lett.* 4285–4294 (2010). doi:10.1021/nl102824h
15. Kang, J. *et al.* Graphene and beyond-graphene 2D crystals for next-generation green electronics. *Micro Nanotechnol. sensors, Syst. Appl.* **6**, 908305 (2014).
16. Schwierz, F., Pezoldt, J. & Granzner, R. Two-dimensional materials and their prospects in transistor electronics. *Nanoscale* **7**, 8261–8283 (2015).
17. Mattheiss, L. F. Band Structures of Transition-Metal-Dichalcogenide Layer compounds. *Phys. Rev. B* **8**, (1973).
18. Dresselhaus, M. S. & Dresselhaus, G. Advances in Physics Intercalation compounds of graphite. **8732**, (2010).
19. Novoselov, K. S. *et al.* Electric Field Effect in Atomically Thin Carbon Films. *Science (80-.)*. **306**, 666–670 (2004).
20. Lee, C., Wei, X., Kysar, J. W. & Hone, J. Measurement of the Elastic Properties and Intrinsic Strength of Monolayer Graphene. *Science (80-.)*. **321**, 385–389 (2008).
21. Yu, A., Roes, I., Davies, A. & Chen, Z. Ultrathin , transparent , and flexible graphene films for supercapacitor application. *Appl. Phys. Lett.* **96**, 1–4 (2010).
22. Xu, Y., Bai, H., Lu, G., Li, C. & Shi, G. Flexible Graphene Films via the Filtration of Water-Soluble. 5856–5857 (2008).
23. Bolotin, K. I. *et al.* Ultrahigh electron mobility in suspended graphene. *Solid State Commun.* **146**, 351–355 (2008).
24. Du, X., Skachko, I., Barker, A. & Andrei, E. V. A. Y. Approaching ballistic transport in suspended graphene. 1–5 (2008). doi:10.1038/nnano.2008.199
25. Suzuki, S. & Yoshimura, M. Chemical Stability of Graphene Coated Silver Substrates for Surface-Enhanced Raman Scattering. *Sci. Rep.* 1–7 (2017). doi:10.1038/s41598-017-

- 14782-2
26. Sprinkle, M. *et al.* First direct observation of a nearly ideal graphene band structure. 1–5
 27. Tiwari, R. K., Rangari, R. & Vlsi, M. Graphene Review : A Future for Electronics Applications. **2**, 6–8
 28. Chhowalla, M. *et al.* The chemistry of two-dimensional layered transition metal dichalcogenide nanosheets. *Nat. Chem.* **5**, 263–75 (2013).
 29. Choi, W. *et al.* Recent development of two-dimensional transition metal dichalcogenides and their applications. *Mater. Today* **20**, 116–130 (2017).
 30. Geim, A. K. & Grigorieva, I. V. Van der Waals heterostructures. *Nature* **499**, (2013).
 31. Lin, Y. *et al.* Atomically thin resonant tunnel diodes built from synthetic van der Waals heterostructures. *Nat. Commun.* **6**, 1–6 (2015).
 32. Radisavljevic, B., Radenovic, A., Brivio, J., Giacometti, V. & Kis, A. Single-layer MoS₂transistors. *Nat. Nanotechnol.* **6**, 147–150 (2011).
 33. Roy, T. *et al.* Field-effect transistors built from all two-dimensional material components. *ACS Nano* **8**, 6259–64 (2014).
 34. Lopez-sanchez, O., Lembke, D., Kayci, M., Radenovic, A. & Kis, A. Ultrasensitive photodetectors based on monolayer MoS₂. *Nat. Nanotechnol.* (2013).
doi:10.1038/nnano.2013.100
 35. Lee, K., Gatensby, R., McEvoy, N., Hallam, T. & Duesberg, G. S. High-performance sensors based on molybdenum disulfide thin films. *Adv. Mater.* **25**, 6699–6702 (2013).
 36. Sarkar, D. *et al.* A subthermionic tunnel field-effect transistor with an atomically thin channel. *Nature* **526**, (2015).
 37. Fiori, G. *et al.* Electronics based on two-dimensional materials. *Nat. Nanotechnol.* **9**, 768–779 (2014).
 38. Novoselov, K. S. *et al.* Two-dimensional atomic crystals. *Proc. Natl. Acad. Sci. U. S. A.* **102**, 10451–3 (2005).

39. Ayari, A., Cobas, E., Ogundadegbe, O. & Fuhrer, M. S. Realization and electrical characterization of ultrathin crystals of layered transition-metal dichalcogenides. *Appl. Phys.* **101**, (2007).
40. Schmidt, H. & Eda, G. Electronic transport properties of transition metal dichalcogenide field-effect devices : surface and interface effects. *Chem. Soc. Rev.* 7715–7736 (2015). doi:10.1039/c5cs00275c
41. Callister, W. D. & Rethwisch, D. G. *Materials Science and Engineering: An Introduction*. (John Wiley & Sons, 2010).
42. Taur, Y. & Ning, T. H. *Fundamentals of Modern VLSI Devices*. (2009).
43. Sze, S. M. & Ng, K. K. *Physics of Semiconductor Devices*. (Wiley and Sons, 2007).
44. Allen, M. J., Tung, V. C. & Kaner, R. B. Honeycomb Carbon : A Review of Graphene. *Chem. Rev.* **110**, 132–145 (2010).
45. Georgiou, T. *et al.* Vertical field effect transistor based on graphene-WS₂ heterstructures for flexible and transparent electronics. *Nanture Nanotechnol.* **8**, (2013).
46. Arco, L. G. De *et al.* Continuous, Highly Flexible, and Transparent Graphene Films by Chemical Vapor Deposition for Organic Photovoltaics. *ACS Nano* **4**, 2865–2873 (2010).
47. Ghosh, S. *et al.* Extremely high thermal conductivity of graphene : Prospects for thermal management applications in nanoelectronic circuits. *Appl. Phys. Lett.* **92**, (2008).
48. Balandin, A. A. *et al.* Superior Thermal Conductivity of Single-Layer Graphene. *Nano Lett.* **8**, 902–907 (2008).
49. Bonaccorso, F., Sun, Z., Hasan, T. & Ferrari, A. C. Graphene photonics and optoelectronics. *Nat. Photonics* **4**, 611–622 (2010).
50. Eftekhari, A. & Garcia, H. The necessity of structural irregularities for the chemical applications of graphene. *Mater. Today Chem.* **4**, 1–16 (2017).
51. Neto, A. H. C. The electronic properties of graphene. *81*, (2009).
52. Wallace, P. R. The Band Theory of Graphite. *Phys. Rev.* **71**, (1946).

53. Bai, C. & Zhang, X. Klein paradox and resonant tunneling in a graphene superlattice. 1–7 (2007). doi:10.1103/PhysRevB.76.075430
54. Britnell, L. *et al.* Field - effect tunneling transistor based on vertical graphene heterostructures. *Science (80-.).* **335**, 1–11 (2012).
55. Chhowalla, M., Voiry, D., Yang, J., Shin, H. S. & Loh, K. P. Phase-engineered transition-metal dichalcogenides for energy and electronics. *MRS Bull.* **40**, (2015).
56. Voiry, D. *et al.* Covalent functionalization of monolayered transition metal dichalcogenides by phase engineering. *Nat. Chem.* **7**, (2014).
57. Gong, C. *et al.* Band alignment of two-dimensional transition metal dichalcogenides: Application in tunnel field effect transistors. *Appl. Phys. Lett.* **103**, 053513 (2013).
58. Isomaki, H. & von Boehm, J. The conduction band structure of ZrS₂ and ZrSe₂. *Phys. Lett.* **89**, 89–92 (1982).
59. Li, X. & Zhu, H. Two-dimensional MoS₂: Properties, preparation, and applications. *J. Mater.* **1**, 33–44 (2015).
60. Terrones, H., López-Urías, F. & Terrones, M. Novel hetero-layered materials with tunable direct band gaps by sandwiching different metal disulfides and diselenides. *Sci. Rep.* **3**, (2013).
61. Ghatak, S., Pal, A. N. & Ghosh, A. Nature of Electronic States in Atomically Thin MoS₂ Field-Effect Transistors. *ACS Nano* **5**, 7707–7712 (2011).
62. Das, S., Chen, H., Penumatcha, A. V. & Appenzeller, J. High Performance Multilayer MoS₂ Transistors with Scandium Contacts. (2013).
63. Radisavljevic, B. & Kis, A. Mobility engineering and a metal-insulator transition in monolayer MoS₂. *Nat. Mater.* **12**, 815–20 (2013).
64. Fiori, G., Szafranek, B. N., Iannaccone, G. & Neumaier, D. Velocity saturation in few-layer MoS₂ transistor. *Appl. Phys. Lett.* **103**, 233509 (2013).
65. Das, S. & Chen, H. High Performance Multilayer MoS₂ Transistors with Scandium

- Contacts. *Nano Lett.* **13**, (2012).
66. Shi, Y., Li, H. & Li, L. J. Recent advances in controlled synthesis of two-dimensional transition metal dichalcogenides via vapour deposition techniques. *Chem. Soc. Rev.* **44**, 2744–2756 (2015).
67. Lin, Z. *et al.* 2D materials advances: From large scale synthesis and controlled heterostructures to improved characterization techniques, defects and applications. *2D Mater.* **3**, 042001 (2016).
68. Novoselov, K. S. & Neto, A. H. C. Two-dimensional crystals-based heterostructures: materials with tailored properties. *Phys. Scr.* **146**, (2012).
69. Jang, A.-R. *et al.* Wafer-Scale and Wrinkle-Free Epitaxial Growth of Single-Orientated Multilayer Hexagonal Boron Nitride on Sapphire. *Nano Lett.* **16**, (2016).
70. Kang, K. *et al.* High-mobility three-atom-thick semiconducting films with wafer-scale homogeneity. *Nature* **520**, 656–660 (2015).
71. Desai, S. B., Madhvapathy, S. R., Sachid, A. B., Llinas, J. P. & Wang, Q. MoS₂ transistors with 1-nanometer gate lengths. *Science (80-.)* **354**, (2016).
72. Wachter, S., Polyushkin, D. K., Bethge, O. & Mueller, T. A microprocessor based on a two-dimensional semiconductor. *Nat. Commun.* **8**, (2017).
73. Furchi, M. M., Pospischil, A., Libisch, F., Burgdo, J. & Mueller, T. Photovoltaic Effect in an Electrically Tunable van der Waals Heterojunction. *Nano Lett.* **14**, (2014).
74. Li, X. *et al.* Transfer of Large-Area Graphene Films for High-Performance Transparent Conductive Electrodes. *Nano Lett.* **9**, (2009).
75. Mlack, J. T. *et al.* Transfer of monolayer TMD WS₂ and Raman study of substrate effects. *Sci. Rep.* **7**, (2017).
76. Desai, S. B. *et al.* Gold-Mediated Exfoliation of Ultralarge OptoelectronicallyPerfect Monolayers. *Adv. Mater.* **28**, (2016).
77. Dean, C. R. *et al.* Boron nitride substrates for high-quality graphene electronics. *Nat.*

- Nanotechnol.* **5**, (2010).
78. Castellanos-Gomez, A., Buscema, M., Molenaar, R., Singh, V. & Janssen, L. Deterministic transfer of two-dimensional materials by all-dry viscoelastic stamping. *2D Mater.* (2014). doi:10.1088/2053-1583/1/1/011002
79. Raychaudhuri, S., Dayeh, S. a., Wang, D. & Yu, E. T. Precise semiconductor nanowire placement through dielectrophoresis. *Nano Lett.* **9**, 2260–2266 (2009).
80. Evoy, S. *et al.* Dielectrophoretic assembly of carbon nanofiber nanoelectromechanical devices. *IEEE Trans. Nanotechnol.* **4**, 570–575 (2005).
81. Dan, Y., Cao, Y., Mallouk, T. E., Johnson, A. T. & Evoy, S. Dielectrophoretically assembled polymer nanowires for gas sensing. *Sensors Actuators, B Chem.* **125**, 55–59 (2007).
82. Velev, O. D. & Bhatt, K. H. On-chip micromanipulation and assembly of colloidal particles by electric fields. *Soft Matter* **2**, 738–750 (2006).
83. Gangwal, S. *et al.* Dielectrophoretic Assembly of Metallodielectric Janus Particles in AC Electric Fields. *Langmuir* **24**, 13312–13320 (2008).
84. Levin, S., Li, J. & Mayer, T. GeSe and SnSe Microparticle FETs Fabricated Through Use of Electric-Field-Assisted Assembly. (2013).
85. Vijayaraghavan, A., Sciascia, C., Dehm, S. & Lombardo, A. Dielectrophoretic Assembly of High-Density Arrays of Individual Graphene Devices for Rapid Screening. *ACS Nano* **3**, (2009).
86. Joung, D., Chunder, A., Zhai, L. & Khondaker, S. I. High yield fabrication of chemically reduced graphene oxide field effect transistors by dielectrophoresis. *Appl. Phys. Lett.* **94**, 1–8 (2009).
87. Smith, B. D., Mayer, T. S. & Keating, C. D. Deterministic assembly of functional nanostructures using nonuniform electric fields. *Annu. Rev. Phys. Chem.* **63**, 241–63 (2012).

88. Griffiths, D. J. *Introduction to Electrodynamics*. (Prentice-Hall, 1999).
89. Zhang, K., Lin, Y.-C. & Robinson, J. A. Synthesis, Properties, and Stacking of Two-Dimensional Transition Metal Dichalcogenides. in *Semiconductors and Semimetals: Volume 95* 189–219 (Elsevier, 2016).
90. Zhang, Y. *et al.* Direct observation of the transition from indirect to direct bandgap in atomically thin epitaxial MoSe₂. *Nat. Nanotechnol.* **9**, 111–115 (2014).
91. Liu, H. J. *et al.* Molecular-beam epitaxy of monolayer and bilayer WSe₂: a scanning tunneling microscopy/spectroscopy study and deduction of exciton binding energy. *2D Mater.* **2**, (2015).
92. Vishwanath, S., Liu, X., Rouvimov, S. & Basile, L. Controllable growth of layered selenides and telluride heterostructures and superlattices using molecular beam epitaxy. *J. Mater. Res.* **31**, (2016).
93. Song, J., Park, J., Lee, W., Choi, T. & Jun, H. Layer-controlled, wafer-scale, and conformal synthesis of tungsten disulfide nanosheets using atomic layer deposition. *ACS Nano* **7**, (2013).
94. Tan, L. K., Liu, B., Teng, J. H., Guo, S. & Low, H. Y. Atomic layer deposition of a MoS₂ film. *Nanoscale* **18**, (2014).
95. Mahler, B., Hoepfner, V., Liao, K. & Ozin, G. A. Colloidal Synthesis of 1T-WS₂ and 2H-WS₂ Nanosheets: Applications for Photocatalytic Hydrogen Evolution. *J. Am. Chem. Soc.* **136**, (2014).
96. Jung, W. *et al.* Colloidal Synthesis of Single-Layer MSe₂ (M = Mo, W) Nanosheets via Anisotropic Solution-Phase Growth Approach. *J. Am. Chem. Soc.* **137**, (2015).
97. ZABINSKI, J. S., DONLEY, M. S., PRASAD, S. V. & McDEVITT, N. T. Synthesis and characterization of tungsten disulphide films grown by pulsed-laser deposition. *J. Mater. Sci.* **29**, (1994).
98. McConney, M. E. *et al.* Direct synthesis of ultra-thin large area transition metal

- dichalcogenides and their heterostructures on stretchable polymer surfaces. *J. Mater. Res.*, (2016).
99. Rockett, A. *The Materials Science of Semiconductors*. (Springer, 2008).
 100. Carlsson, J.-O. & Martin, P. M. Chemical Vapor Deposition. in *Handbook of Deposition Technologies for Films and Coatings* (ed. Martin, P. M.) 314–363 (Elsevier, 2010).
 101. Lin, Z. *et al.* Controllable Growth of Large–Size Crystalline MoS₂ and Resist-Free Transfer Assisted with a Cu Thin Film. *Sci. Rep.* **5**, (2015).
 102. Subramanian, S. *et al.* Properties of synthetic epitaxial graphene/molybdenum disulfide lateral heterostructures. *Carbon N. Y.* (2017).
 103. Kim, K. S. *et al.* Large-scale pattern growth of graphene films for stretchable transparent electrodes. *Nature* **457**, (2009).
 104. Li, X. *et al.* Large-Area Synthesis of High-Quality and Uniform Graphene Films on Copper Foils. *Science (80-.).* **324**, (2009).
 105. Li, X., Cai, W., Colombo, L. & Ruoff, R. S. Evolution of Graphene Growth on Ni and Cu by Carbon Isotope Labeling. *Nano Lett.* **9**, (2009).
 106. Choi, W., Lahiri, I., Seelaboyina, R. & Kang, Y. S. Synthesis of graphene and its applications: A review. *Crit. Rev. Solid State Mater. Sci.* **35**, 52–71 (2010).
 107. Hao, Y. *et al.* The Role of Surface Oxygen in the Growth of Large Single-Crystal Graphene on Copper. *Science (80-.).* (2013).
 108. Emtsev, K. V., Speck, F., Seyller, T. & Ley, L. Interaction, growth, and ordering of epitaxial graphene on SiC{0001} surfaces: A comparative photoelectron spectroscopy study. *Phys. Rev. B* **77**, (2008).
 109. Riedl, C. *et al.* Structural and electronic properties of epitaxial graphene on SiC (0001): a review of growth , characterization , transfer doping and hydrogen intercalation. *J. Phys. D* **43**, (2010).
 110. Riedl, C., Coletti, C., Iwasaki, T., Zhakharov, A. A. & Starke, U. Quasi-Free-Standing

- Epitaxial Graphene on SiC Obtained by Hydrogen Intercalation. *Phys. Rev. Lett.* **103**, (2009).
111. Halliday, D., Resnick, R. & Walker, J. *Fundamentals of Physics*. (John Wiley & Sons, 2010).
 112. Schroder, D. K. *Semiconductor Material and Device Characterization*. (John Wiley & Sons, 2006).
 113. Chakrapani, V. Semiconductor Junctions, Solid-Solid Junctions. in *Encyclopedia of Applied Electrochemistry* (eds. Kreysa, G., Ota, K. & Savinell, R. F.) (Springer, 2014).
 114. Jena, D. Tunneling Transistors Based on Graphene and 2-D Crystals. *Proc. IEEE* **101**, 1585–1602 (2013).
 115. Shukla, N. *et al.* A steep-slope transistor based on abrupt electronic phase transition. *Nat. Commun.* **6**, 1–6 (2015).
 116. Hu, C. MOS capacitor. in *Modern Semiconductor Devices for Integrated Circuits* (ed. Pearson) 157–194 (2010). doi:10.1038/nmat2749
 117. Seabaugh, A. C. & Zhang, Q. Low-Voltage Tunnel Transistors for Beyond CMOS Logic. *Proc. IEEE* **98**, 2095–2110 (2010).
 118. Banica, F.-G. *Chemical Sensors and Biosensors*. (John Wiley & Sons, 2012).
 119. Kaur, M., Aswal, D. K. & Yakhmi, J. V. Chemiresistor Gas Sensors: Materials, Mechanisms, and Fabrication. in *Science and Technology of Chemiresistor Gas Sensors* (eds. Aswal, D. K. & Gupta, S. K.) (Nova, 2007).
 120. Averill, B. & Eldredge, P. *Chemistry: Principles, Patterns, and Applications*. (Prentice-Hall, 2007).
 121. Ashenhurst, J. A. How to use a pKa Table. *Master Organic Chemistry* (2018). Available at: <https://www.masterorganicchemistry.com/2010/09/29/how-to-use-a-pka-table/>.
 122. Cho, B. *et al.* Charge-transfer-based gas sensing using atomic-layer MoS₂. *Sci. Rep.* **5**, 8052 (2015).

123. Hu, Y. *et al.* Supersensitive, fast-response nanowire sensors by using schottky contacts. *Adv. Mater.* **22**, 3327–3332 (2010).
124. Ju, D., Xu, H., Qiu, Z., Guo, J. & Zhang, J. Chemical Highly sensitive and selective triethylamine-sensing properties of nanosheets directly grown on ceramic tube by forming NiO / ZnO PN heterojunction. *Sensors Actuators B* **200**, 288–296 (2014).
125. Wu, W. *et al.* Wafer-scale synthesis of graphene by chemical vapor deposition and its application in hydrogen sensing. *Sensors Actuators, B Chem.* **150**, 296–300 (2010).
126. Mirica, K. A., Azzarelli, J. M., Weis, J. G., Schnorr, J. M. & Swager, T. M. Rapid prototyping of carbon-based chemiresistive gas sensors on paper. *Proc. Natl. Acad. Sci.* **110**, E3265–E3270 (2013).
127. Perkins, F. K. *et al.* Chemical vapor sensing with monolayer MoS₂. *Nano Lett.* **13**, 668–673 (2013).
128. Wu, E. *et al.* Ultra-sensitive and Fully Reversible NO₂ Gas Sensing based on p-type MoTe₂ under ultra-violet Illumination. *ACS Sensors* **3**, 1719–1726 (2018).
129. Benjamin, M. M. & Lawler, D. F. *Water Quality Engineering: Physical / Chemical Treatment Processes*. (John Wiley & Sons, 2013).
130. Do, D. D. *Adsorption analysis: Equilibria and Kinetics*. (Imperial College Press, 1998).
131. Foo, K. Y. & Hameed, B. H. Insights into the modeling of adsorption isotherm systems. *156*, 2–10 (2010).
132. Arafat, M. M., Dinan, B., Akbar, S. A. & Haseeb, A. S. M. A. Gas sensors based on one dimensional nanostructured metal-oxides: A review. *Sensors* **12**, 7207–7258 (2012).
133. Li, Z. & Fonash, S. J. Properties of Pd-Gate Heterostructure Diodes for Hydrogen Detection. in *Chemical Sensor Technology, Volume 2* (ed. Seiyama, T.) (Elsevier, 2013).
134. Samitier, J., López-Villegas, J. M., Marco, S., Ruiz, O. & Morante, J. R. New method to analyze time transients signal in chemical sensors. *Sensors and Actuators B-Chemical* **18–19**, 308–312 (1994).

135. Gutierrez-Osuna, R., Nagle, H. T. & Schiffman, S. S. Transient response analysis of an electronic nose using multi-exponential models. *Sensors Actuators, B Chem.* **61**, 170–182 (1999).
136. Li, J. *et al.* Carbon Nanotube Sensors for Gas and Organic Vapor Detection. *Nano Lett.* **3**, 929–933 (2003).
137. Lee, Y.-H. *et al.* Synthesis of large-area MoS₂ atomic layers with chemical vapor deposition. *Adv. Mater.* **24**, 2320–5 (2012).
138. Shin, Y. J. *et al.* Surface-Energy Engineering of Graphene. *Langmuir* **26**, (2010).
139. Kang, J., Liu, W., Sarkar, D., Jena, D. & Banerjee, K. Computational Study of Metal Contacts to Monolayer Transition-Metal Dichalcogenide Semiconductors. *Phys. Rev. X* **4**, (2014).
140. Mack, C. *Fundamental Principles of Optical Lithography*. (John Wiley & Sons, 2007).
141. Burger, G. J. *et al.* High resolution shadow mask patterning in deep holes and its application to an electrical wafer feed-through. in *8th International Conference on Solid-State Sensors and Actuators* (1995).
142. Photo Sciences. Precision shadow masks. Available at: <https://www.photosciences.com/photomask-and-patterned-optics-services/shadow-masks/>.
143. Micron Laser Technology. Shadow Masks. (2019). Available at: <https://micronlaser.com/laser-applications/shadow-masks/>.
144. Ito, T. & Okazaki, S. Pushing the Limits of Lithography. *Nature* **406**, (2000).
145. Vieu, C. *et al.* Electron beam lithography : resolution limits and applications. *Appl. Surf. Sci.* **164**, 111–117 (2000).
146. Rosenberger, M. R. *et al.* Nano-"Squeegee" for the Creation of Clean 2D Material Interfaces. *ACS Appl. Mater. Interfaces* **10**, 10379–10387 (2018).
147. Pettes, M. T., Jo, I., Yao, Z. & Shi, L. Influence of Polymeric Residue on the Thermal Conductivity of Suspended Bilayer Graphene. *Nano Lett.* **11**, (2011).

148. Choi, W., Shehzad, M. A., Park, S. & Seo, Y. Influence of removing PMMA residues on surface of CVD graphene using a contact-mode atomic force microscope. *RSC Adv.* **7**, (2017).
149. Lin, Y. *et al.* Graphene Annealing : How Clean Can It Be ? *Nano Lett.* **12**, (2011).
150. Chapman, B. *Glow Discharge Processes: Sputtering and Plasma Etching*. (Wiley and Sons, 1980).
151. Darnon, M. Plasma Etching in Microelectronics. in *Plasma Etching Processes for CMOS Devices Realization* (ed. Posseme, N.) (Elsevier, 2017). doi:10.1016/B978-1-78548-096-6.50002-X
152. Robinson, J. A. *et al.* Contacting graphene. *Appl. Phys. Lett.* **053103**, (2014).
153. Kedzierski, J., Hsu, P.-L., Healey, P., Wyatt, P. & Keast, C. Epitaxial graphene transistors on SiC substrates. in *Device Research Conference* (2008).
154. Yan, H. *et al.* Tunable infrared plasmonic devices using graphene/insulator stacks. *Nat. Nanotechnol.* **7**, (2012).
155. Huang, Y. *et al.* An innovative way of etching MoS2: Characterization and mechanistic investigation. *Nano Res.* **6**, (2013).
156. Jeon, M. H. *et al.* Controlled MoS2 layer etching using CF4 plasma. *Nanotechnology* **26**, (2015).
157. Xiao, S. *et al.* Atomic-layer soft plasma etching of. *Sci. Rep.* **6**, (2016).
158. Mattox, D. M. *Handbook of Physical Vapor Deposition (PVD) Processing*. (Elsevier, 2010).
159. Ohring, M. *Materials Science of Thin Films*. (Academic Press, 2001).
160. Golden, J., Miller, H., Nawrocki, D. & Ross, J. *Optimization of Bi-layer Lift-Off Resist Proces s.* (2009).
161. Kim, C. *et al.* Fermi Level Pinning at Electrical Metal Contacts of Monolayer Molybdenum Dichalcogenides. *ACS Nano* **11**, 1588–1596 (2017).

162. Kooi, E. & Schmitz, A. Brief Notes on the History of Gate Dielectrics in MOS Devices. in *High Dielectric Constant Materials: VLSI MOSFET Applications* (eds. Huff, H. R. & Gilmer, D. C.) (2005).
163. Wang, D., Wang, Q., Javey, A., Tu, R. & Dai, H. Germanium nanowire field-effect transistors with SiO₂ and high-k HfO₂ gate dielectrics. *Appl. Phys. Lett.* **83**, (2003).
164. Kim, S. *et al.* Realization of a high mobility dual-gated graphene field-effect transistor with Al₂O₃ dielectric. *Appl. Phys. Lett.* **94**, (2009).
165. Liu, H., Ye, P. D., Member, S. & We, A. MoS₂ Dual-Gate MOSFET with atomic-layer-deposited Al₂O₃ as top-gate dielectric. *IEEE* **33**, 546–548 (2012).
166. Perkins, C. M., Triplett, B. B., McIntyre, P. C. & Saraswat, K. C. Electrical and materials properties of ZrO₂ gate dielectrics grown by atomic layer chemical vapor deposition. *Appl. Phys. Lett.* **78**, (2001).
167. Johnson, R. W., Hultqvist, A. & Bent, S. F. A brief review of atomic layer deposition : from fundamentals to applications. *Mater. Today* **17**, (2014).
168. George, S. M. Atomic Layer Deposition : An Overview. *Chem. Rev.* **110**, 111–131 (2010).
169. Atomic Layer Deposition. Veeco Available at: <http://cambridgenanotechald.com/atomic-layer-deposition/index.shtml>.
170. Yang, J. *et al.* Improved Growth Behavior of Atomic-Layer-Deposited High-k Dielectrics on Multilayer MoS₂ by Oxygen Plasma Pretreatment. *ACS Appl. Mater. Interfaces* **5**, (2013).
171. CHristian, W. *et al.* Atomic layer deposition on 2D transition metal chalcogenides: Layer dependent reactivity and seeding with organic ad-layers. *Chem. Commun.* (2015). doi:10.1039/b000000x
172. Azcatl, A. *et al.* MoS₂ functionalization for ultra-thin atomic layer deposited dielectrics. *Appl. Phys. Lett.* **104**, 1–5 (2014).
173. Panzer, M. J. & Frisbie, C. D. Exploiting Ionic Coupling in Electronic Devices:

- Electrolyte-Gated Organic Field-Effect Transistors. *Adv. Mater.* **20**, (2008).
174. Jung, N. *et al.* Charge transfer chemical doping of few layer graphenes: charge distribution and band gap formation. *Nano Lett.* **9**, 4133–7 (2009).
175. Chakraborty, B. *et al.* Symmetry-dependent phonon renormalization in monolayer MoS₂ transistor. *Phys. Rev. B* **85**, (2012).
176. Micro Chem. *LOR and PMGI Resists*.
177. Shipley. *Megaposit SPR 3000 Series Photo resist*.
178. Fullerton-Shirey, S. K., Ganapatibhotla, L. V. N. R., Shi, W. & Maranas, J. K. Influence of thermal history and humidity on the ionic conductivity of nanoparticle-filled solid polymer electrolytes. *J. Polym. Sci. Part B Polym. Phys.* **49**, (2011).
179. Stanford Research Systems. *About Lock-In Amplifiers: Application Note #3*.
180. NIST. NIST X-ray photoelectron Spectroscopy Database.
181. Morrow, T. J., Li, M., Kim, J., Mayer, T. S. & Keating, C. D. Programmed assembly of DNA-coated nanowire devices. *Science* **323**, 352 (2009).
182. Li, P., Lei, N., Xu, J. & Xue, W. High-Yield Fabrication of Graphene Chemiresistors With Dielectrophoresis. *IEEE Trans. Nanotechnol.* **11**, (2012).
183. Wang, S.-P., Wu, C.-H. & Hong, C.-C. MoS₂nanosensors fabricated by dielectrophoretic assembly for ultrasensitive and rapid sensing of volatile organic compounds. in *IEEE sensors* (2015).
184. Durrant, A. *Vectors in Physics and Engineering*. (Chapman & Hall, 1996).
185. Gutierrez, H. R., Perea-Lopez, N., Elias, A. L., Berkdemir, A. & Wang, B. Extraordinary Room-Temperature Photoluminescence in Triangular WS₂ Monolayers. *Nano Lett.* **13**, (2013).
186. Ramasubramaniam, A. Large excitonic effects in monolayers of molybdenum and tungsten dichalcogenides. *Phys. Rev. B* **86**, (2012).
187. Kim, J., Choi, S. M., Seo, W.-S. & Cho, W.-S. Thermal and electronic properties of

- exfoliated metal chalcogenides. *Bull. Korean Chem. Soc.* **31**, (2010).
188. Dortmund Data Bank. Dielectric Constant of Acetone. Available at:
http://www.ddbst.com/en/EED/PCP/DEC_C4.php.
189. Shell. *Technical Datasheet: Acetone*. (2017).
190. Lide, D. R. *CRC Handbook of Chemistry and Physics*. (CRC Press, 1998).
191. Chemical Book. Chemical Book: Acetone. Available at:
https://www.chemicalbook.com/productchemicalpropertiescb3130928_en.htm#msdsa.
192. Torres, J., Zhu, Y., LIU, P., Lim, S. C. & Yun, M. Adhesion Energies of 2D Graphene and MoS₂ to Silicon and Metal substrates. *Phys. Status Solidi* **215**, (2017).
193. Zhao, W. *et al.* Evolution of Electronic Structure in Atomically Thin Sheets of WS₂ and WSe₂. *ACS Nano* **7**, (2013).
194. Zhu, B., Chen, X. & Cui, X. Exciton Binding Energy of Monolayer WS₂. *Sci. Rep.* **5**, (2015).
195. Currie, M., Hanbicki, A. T., Kioseoglou, G. & Jonker, B. T. Optical control of charged exciton states in tungsten disulfide. *Appl. Phys. Lett.* **106**, (2015).
196. Lin, Z. *et al.* Defect Engineering of two-dimensional transition metal dichalcogenides. *2D Mater.* **3**, (2016).
197. Allain, A., Kang, J., Banerjee, K. & Kis, A. Electrical contacts to two-dimensional semiconductors. *Nat. Publ. Gr.* **14**, 1195–1205 (2015).
198. Gong, C., Colombo, L., Wallace, R. M. & Cho, K. The unusual mechanism of partial fermi level pinning at metal-MoS₂ interfaces. *Nano Lett.* **14**, 1714–1720 (2014).
199. Kappera, R. *et al.* Metallic 1T phase source / drain electrodes for field effect transistors from chemical vapor deposited MoS₂. *APL Mater.* (2014). doi:10.1063/1.4896077
200. McDonnell, S., Smyth, C., Hinkle, C. L. & Wallace, R. M. MoS₂–Titanium Contact Interface Reactions. *Appl. Mater. Interfaces* **8**, (2016).
201. Du, Y. *et al.* MoS₂Field-Effect Transistors With Graphene/Metal Heterocontacts. *IEEE*

- Electron Device Lett.* **35**, (2013).
202. Lee, Y. T. *et al.* Graphene Versus Ohmic Metal as Source-Drain Electrode for MoS₂ Nanosheet Transistor Channel. *Small* **10**, (2014).
 203. Yu, Y. *et al.* Tuning the graphene work function by electric field effect. *Nano Lett.* **9**, (2009).
 204. Chuang, H., Tan, X., Ghimire, N. J. & Perera, M. M. High Mobility WSe₂ p- and n- Type Field Effect Transistors Contacted by Highly Doped Graphene for Low-Resistance Contacts. *Nano Lett.* **14**, 1–22 (2014).
 205. Kwak, J. Y. *et al.* Electrical Characteristics of Multilayer MoS₂ FET's with MoS₂/Graphene Heterojunction Contacts. *ACS Nano* **14**, (2014).
 206. Ling, X. *et al.* Parallel Stitching of Two-Dimensional Materials. *Adv. Mater.* (2016).
 207. Zhao, M. *et al.* Large-scale chemical assembly of atomically thin transistors and circuits. *Nat. Nanotechnol.* **11**, (2016).
 208. Guimaraes, M. H. D. *et al.* Atomically Thin Ohmic Edge Contacts Between Two-Dimensional Materials. *ACS Nano* **10**, (2016).
 209. Arco, L. G. De, Zhang, Y., Kumar, A. & Zhou, C. Synthesis, Transfer, and Devices of Single- and Few-Layer graphene by Chemical vapor deposition. *IEEE Trans. Nanotechnol.* **8**, 135–138 (2009).
 210. Goniszewski, S. *et al.* Correlation of p-doping in CVD Graphene with Substrate Surface Charges. *Nat. Publ. Gr.* 1–9 (2016). doi:10.1038/srep22858
 211. Qiu, H. *et al.* Hopping transport through defect-induced localized states in molybdenum disulphide. *Nat. Commun.* **4**, 1–6 (2013).
 212. Tongay, S. *et al.* Defects activated photoluminescence in two-dimensional semiconductors: interplay between bound, charged, and free excitons. *Sci. Rep.* **3**, 2657 (2013).
 213. Larentis, S. *et al.* Band Offset and Negative Compressibility in Graphene-MoS₂

- heterostructures. *Nano Lett.* **14**, (2014).
214. Mammadov, S. *et al.* Work function of graphene multilayers on SiC(0001). *2D Mater.* **4**, (2017).
215. Nan, H. *et al.* Strong photoluminescence enhancement of MoS₂through defect engineering and oxygen bonding. *ACS Nano* **8**, 5738–5745 (2014).
216. Colombo, L., Vogel, E. M., Ruoff, R. S. & Wallace, R. M. The effect of chemical residues on the physical and electrical properties of chemical vapor deposited graphene transferred to SiO₂. *J. Appl. Phys.* **122** 108, 3–5 (2011).
217. Jain, A. *et al.* Minimizing residues and strain in 2D materials transferred from PDMS. *Nanotechnology* **29**, (2018).
218. Fang, H. *et al.* Degenerate n - Doping of Few-Layer Transition Metal Dichalcogenides by Potassium. *Nano Lett.* **13**, (2013).
219. Rai, A. *et al.* Air Stable Doping and Intrinsic Mobility Enhancement in Monolayer Molybdenum Disulfide by Amorphous Titanium Suboxide Encapsulation. *Nano Lett.* **15**, (2015).
220. Fiori, G. *et al.* Electronics based on two-dimensional materials. *Nature* **9**, (2014).
221. Leong, W. S., Nai, C. T. & Thong, J. T. L. What Does Annealing Do to Metal – Graphene Contacts ? *Nano Lett.* **14**, (2014).
222. Jin, W. *et al.* Tuning the electronic structure of monolayer graphene/ Mo S₂ van der Waals heterostructures via interlayer twist. *Phys. Rev. B* **92**, (2015).
223. Liu, X. *et al.* Rotationally Commensurate Growth of MoS₂ on Epitaxial Graphene. *ACS Nano* **10**, (2016).
224. Lee, J. *et al.* Wafer-Scale Growth of Single-Crystal Monolayer Graphene on Reusable Hydrogen-Terminated Germanium. *Science (80-.).* **344**, (2014).
225. Croes, K., Li, Y., Lofrano, M., Wilson, C. J. & Tokei, Z. Intrinsic Study of current crowding and current density gradient effects on electromigration in BEOL copper

- interconnects. in *IEEE international reliability physics symposium* (2013).
226. Tang, H.-L. *et al.* Multilayer Graphene-WSe₂ Heterostructures for WSe₂ Transistors. *ACS Nano* **11**, (2017).
 227. Miorandi, D., Sicari, S., Pellegrini, F. De & Chlamtac, I. Internet of Things: Vision, application areas and research challenges. *Ad Hoc Networks* **10**, 583–587 (2012).
 228. GSM Association. *Understanding the Internet of Things (IoT)*. (2014).
 229. Suri, N. *et al.* Analyzing the applicability of Internet of Things to the battlefield environment. *2016 Int. Conf. Mil. Commun. Inf. Syst. ICMCIS 2016* (2016). doi:10.1109/ICMCIS.2016.7496574
 230. Barakat, N. H. *et al.* Chemical synthesis of two series of nerve agent model compounds and their stereoselective interaction with human acetylcholinesterase and human butyrylcholinesterase. *Chem. Res. Toxicol.* **22**, 1669–1679 (2009).
 231. Laying groundwork for the Internet of Battlefield Things. *Engineering, Virginia Tech Department of Electrical and Computer* (2017). Available at: <https://ece.vt.edu/news/article/the-internet-of-battlefield-things>.
 232. NIH. PubChem Open Chemistry Database. Available at: <https://pubchem.ncbi.nlm.nih.gov/>.
 233. Yang, S., Jiang, C. & Wei, S. huai. Gas sensing in 2D materials. *Appl. Phys. Rev.* **4**, (2017).
 234. Donarelli, M. & Ottaviano, L. 2D Materials for Gas Sensing Applications: A Review on Graphene Oxide, MoS₂, WS₂ and Phosphorene. *Sensors (Basel)*. **18**, (2018).
 235. Friedman, A. L. *et al.* Chemical vapor sensing of two-dimensional MoS₂ field effect transistor devices. *Solid. State. Electron.* **101**, 2–7 (2014).
 236. Mehmood, F. & Pachter, R. Density functional theory study of chemical sensing on surfaces of single-layer MoS 2 and graphene. *J. Appl. Phys.* **115**, (2014).
 237. Robinson, J. A., Snow, E. S., Bădescu, ř. C., Reinecke, T. L. & Perkins, F. K. Role of

- defects in single-walled carbon nanotube chemical sensors. *Nano Lett.* **6**, 1747–1751 (2006).
238. Kim, J., Choi, S., Lee, J., Chung, Y. & Tae, Y. Chemical Gas sensing properties of defect-induced single-walled carbon nanotubes. *Sensors Actuators B* **228**, 688–692 (2016).
 239. Yamazoe, N. New approaches for improving semiconductor gas sensors. *Sensors Actuators B* **5**, 13–31 (1994).
 240. Gong, J., Li, Y., Hu, Z., Zhou, Z. & Deng, Y. Ultrasensitive NH₃ Gas Sensor from Polyaniline Nanograin Enchased TiO₂ Fibers. *2010* **21**, (114AD).
 241. Liu, B. *et al.* High-performance chemical sensing using Schottky-contacted chemical vapor deposition grown monolayer MoS₂ transistors. *ACS Nano* **8**, 5304–5314 (2014).
 242. Feng, Z. *et al.* Enhanced Sensitivity of MoTe₂ Chemical Sensor through Light Illumination. *Micromachines* **8**, (2017).
 243. Chen, W., Hou, X., Shi, X. & Pan, H. Two-Dimensional Janus Transition Metal Oxides and Chalcogenides : Multifunctional Properties for Photocatalysts , Electronics , and Energy Conversion. *ACS Appl. Mater. Interfaces* **10**, 35289–35295 (2018).
 244. Burman, D., Ghosh, R., Santra, S., Kumar Ray, S. & Kumar Guha, P. Role of vacancy sites and UV-ozone treatment on few layered MoS₂nanoflakes for toxic gas detection. *Nanotechnology* **28**, (2017).
 245. Feng, Z. *et al.* Enhanced Sensitivity of MoTe₂Chemical Sensor through Light Illumination. *Micromachines* **8**, 8050155 (2017).
 246. Wu, C.-C. *et al.* Elucidating the Photoresponse of Ultrathin MoS₂ Field-Effect Transistors by Scanning Photocurrent Microscopy. *2013* **15**, (4AD).
 247. Čabo, A. G. *et al.* Observation of Ultrafast Free Carrier Dynamics in Single Layer MoS₂. *Nano Lett.* **15**, (2015).
 248. Ohta, T., Bostwick, A., Seyller, T., Horn, K. & Rotenberg, E. Controlling the Electronic Structure of Bilayer graphene. *Science (80-)* **313**, (2006).

249. Dolan-Jenner. *Fiber-Lite Model 190 Convection Cooled 30 Watt Illuminator*.
250. Sun, J. *et al.* Chemical Preparation of polypyrrole @ WO₃ hybrids with p-n heterojunction and sensing performance to triethylamine at room temperature. *Sensors Actuators B* **238**, 510–517 (2017).
251. Li, W. *et al.* triethylamine sensor based on ZnO micropyramids prepared by molten salt growth method. *J. Alloys Compd.* **695**, 2930–2936 (2017).
252. Yang, H., Cheng, X., Zhang, X., Zheng, Z. & Tang, X. A novel sensor for fast detection of triethylamine based on rutile TiO₂ nanorod arrays. *Sensors Actuators B Chem.* **205**, 322–328 (2014).
253. Yang, X. *et al.* Chemical Highly sensitive and selective triethylamine gas sensor based on porous SnO₂ / Zn₂SnO₄ composites. *Sensors Actuators B* **8**, 213–220 (2018).
254. Sui, L. *et al.* Sensors and Actuators B : Chemical hierarchical structure for highly selective triethylamine sensor. *Sensors Actuators B Chem.* **208**, 406–414 (2015).
255. Ju, D. *et al.* Near Room Temperature , Fast-Response , and Highly Sensitive Triethylamine Sensor Assembled with Au-Loaded ZnO / SnO₂ Core – Shell Nanorods on Flat Alumina Substrates. *Appl. Mater. Interfaces* **7**, (2015).

Donna D. Deng

ddd19@psu.edu | (952) 217-6212

EDUCATION

Pennsylvania State University – University Park Fall 2013 – May 2019

PhD in Materials Science and Engineering
Cumulative GPA - 3.52

University of Minnesota - Twin Cities Fall 2009 - May 2013

Bachelor of Materials Science and Engineering - cum laude
Minors in Astrophysics and Physics

SELECTED PUBLICATIONS

- S. Subramanian, D.D. Deng, K.Xu, N. Simonson, K. Wang, K. Zhang, J. Li, R. Feenstra, S.S. Fullerton Shirey, J.A. Robinson. “Properties of synthetic Epitaxial Graphene/Molybdenum Disulfide Lateral Heterostructures.” Submitted to Carbon, 2017.
- D.D. Deng, Z. Lin, A.L. Elias, N. Perea Lopez, J. Li, C. Zhou, K. Zhang, S. Feng, H. Terrones, J.S. Mayer, J.A. Robinson, M. Terrones, T.S. Mayer. “Electric-field-assisted directed assembly of transition metal dichalcogenide monolayer sheets.” ACS Nano, 2016, 10 (5), 5006-5014.

SELECTED PRESENTATIONS

- D.D. Deng, S. Subramanian, K. Zhang, K. Wang, N. Simonson, G.R. Bhimanapati, T.S. Mayer, J.A. Robinson, “Tuning transport at the graphene/TMD interface.” Presented at the 47th IEEE SISC, Dec 8-10 2016, (San Diego, CA).
- D.D. Deng, S. Subramanian, K. Zhang, K. Wang, N. Simonson, G.R. Bhimanapati, J.A. Robinson, “Electronic transport in graphene-based lateral heterostructures.” Presented at the 2016 MRS Fall Meeting and Exhibit, Nov 27 – Dec 2 2016, (Boston, MA).

MISC. EXPERIENCES & HONORS

Safety Olympics committee member

Spring 2016 – Spring 2018

Laboratory safety manager

Spring 2016 – Fall 2017

3M Graduate Fellowship

Fall 2013 – Spring 2017